UNIVERSITY OF LIVERPOOL

Surface Studies of Model Intermetallic Catalysts

Thesis submitted in accordance with the requirements
of the University of Liverpool for the degree of Doctor in Philosophy

By Michael Lowe

November 2015

Acknowledgments

The completion of this thesis has been a challenging and at times seemingly endless task. It is, however, an undertaking which has been thoroughly satisfying and rewarding, even if I would have much rather been sat with a vacuum chamber than a keyboard. I would like to thank Dr. Hem Raj Sharma for giving me the opportunity to undertake this research and for all his considerable help and guidance. I would also like to thank Prof. Ronan M^{c}Grath for inviting me into his research group and for his advice and expertise.

I have had the pleasure of working with some extremely talented scientists during my PhD, I would like to thank Dr. Joseph Smerdon for all the crazy hours he made me work, even if I've taken a while to appreciate it. I would like to thank Dr. Thakur Yadav and Dr. Abdullah Al-Mahboob for their hard work and input with my projects. I also extend gratitude to Dr. Vincent Fournée and Dr. Julian Ledieu, without them (and their laboratories) I may not have had a thesis at all. I would also like to thank colleagues Sanger Hars and Stuart Thorn for their advice and contributions, experimental or otherwise. My gratitude must also go to Dr. Sam Haq and Dr. Paul Unsworth for their knowledge and expertise about all things UHV. I would also like to acknowledge Prof. Andy Cooper and Dr. Rob Clowes at the Centre for Materials Discovery for the use of their high resolution SEM.

This work was funded from various sources and I'd like recognize the UK Engineering and Physical Sciences Research Council for financial support, the European COST Action CM0904 for experimental and conference travel funds, and the European CMAC for funding experimental research trips.

My final thanks go to my family and friends who have kindly neglected to ask me where this was all heading for the past four years. Thank you Mum and Dad for all your love and support that has enabled me to get this far and to believe it was possible. My utmost thanks go to my wife Katie, for her love and limitless positivity. Thank you for the times you convinced me not to pack it all in, I'm almost certain I would have given up if it weren't for you. Here's to the next seemingly impossible challenge, whatever it is...

Michael Lowe 2015

Abstract

Intermetallic compounds have been identified as possible replacements for traditionally used catalysts for heterogeneous reactions. With their fixed stoichiometry, defined active sites and tunable density of states near the Fermi level these materials provide a multitude of possibilities for improving the way resources are used for energy and transport applications. Current catalysts do not possess the required stability or selectivity for potential mobile applications. Using a variety of microscopic, diffraction and spectroscopic techniques it has been possible to investigate the structure and chemistry of these materials.

The intermetallic compound ZnPd has been studied to understand its surface structure and stability, by developing a new preparation routine to provide atomically flat surfaces. The presence of the Zn-Pd bond parallel or close to parallel to the surface was found to be a key factor in the stability of surfaces.

Quasicrystalline *i*-Al-Cu-Fe was modified using a procedure similar to that used in preparation of Raney catalysts, to attempt to understand the influence of quasicrystalline structure on catalytic behaviour. The subsurface region underneath oxide coverage was found to contain catalytically active Cu metal dispersed by Fe and Fe_3O_4. The presence of pentagonal and dodecahedral facets suggested the leaching kinetic of these surfaces was strongly influenced by crystallographic orientation.

Similar experiments carried out on a *d*-Al-Ni-Co quasicrystal with three well-defined surfaces was used to test this observation further. It was identified that crystallographic directions in the quasicrystal played a larger role in the leaching kinetics of the material than the macroscopic surface orientation with respect to the leaching solution.

Finally, using a simple test molecule, the adsorption characteristics of the clean *i*-Al-Cu-Fe crystal were investigated to provide information about the role of surface and subsurface structures in surface reactivity and specific site separation. It was possible to decorate a unique five-fold aperiodic lattice relating to the position of Fe in the material, creating a quasiperiodic molecular overlayer. The two-fold and three-fold surfaces of the isostructural *i*-Ag-In-Yb inhibited the formation of any ordered overlayer.

It is hoped that this work can add to the current discussion promoting a 'knowledge-based' view of catalyst development and also provide a good basis for further studies using new techniques that seek to bridge the pressure and materials gap that separate fundamental surface science and catalytic reaction studies.

Contents

Chapter 1

Introduction

1.1 Motivation

Demand for energy is ever increasing, and with countries such as India and China rapidly becoming more and more developed the global energy requirements are only going to grow [1]. Recent studies have shown that member states of the Organization for Economic Cooperation and Development (OECD), have managed to level off their consumption to approximately 3.5 Mtoe (Million Tonnes of Oil Equivalent) or 1.47×10^{11} GJ. The global consumption is continuing to grow and now stands at approximately 9 Mtoe or 3.8×10^{11} GJ, with large increases from developing nations and economies around the world [2]. Global energy is currently produced largely through the combustion of fossil fuel hydrocarbons, over 75% of energy including electricity generation. Many of the materials used in the developed world are constructed from the same hydrocarbons [3]. About 10% of hydrocarbons used are for non-energy purposes. This creates a further problem; as the world requires more hydrocarbon based fuels and materials to continue to function, if production begins to dwindle, as has been predicted although not observed yet, prices will increase and development will stumble. Add to this the threat posed by climate change through the 'anthropogenic greenhouse effect' [4], and it becomes obvious that immediate action is required.

The automobile industry is estimated to produce 13-14% of total greenhouse emissions globally, and this has led to the desire to see the industry altered to adhere to a 'greener' policy. These attempts have taken many forms from solar powered cars to electrically powered cars powered from large batteries charged from the grid. Fuel cells are considered by many to be a much more suitable answer to these problems, it is possible to operate with only hydrogen and air as fuels and water vapour as an emission, the technology has significant merit in terms of reducing both hydrocarbon use and greenhouse emissions. Fuel Cells

within cars could theoretically boast a similar level of performance to standard petroleum powered engines [5].

There are several drawbacks to industry, however, namely the storage and distribution of hydrogen, the cost of hydrogen production and the carbon footprint of industrial hydrogen production [6]. The consumer too must first be convinced that new technologies can provide the performance they have previously had, at no further cost. These drawbacks can begin to be minimised through the utilisation of new methods and technologies. While the fuel-cell is well understood and developed, the use of different fuels and in particular allowing the end-user to be a member of the general public rather than a technology enthusiast bring about new challenges. A potential breakthrough may be in the region of catalysis. Catalysts are vital to the survival of our way of life on earth but their development can be considered a historical act of accidental discovery, and continued use 'because it works'. If it is possible to improve the functions of fuel cells, or provide cleaner fuel, or a more efficient fuel conversion through developing better catalysts, then clearly the realm of catalysis is a worthy area of research. The aim is to develop a 'knowledge-based' approach to catalysis; by understanding the fundamental properties of these materials it will be possible to tune their manufacture for greater applicability to the reactions in question.

Intermetallic compounds offer unique qualities in the field of catalysis. The crystal structure of the constituent elements allows both a fixed active site separation and an electronic structure different to that of its constituents. This allows for a material with a tunable set of properties that can be chosen to form ideal catalysts. The intermetallic compounds studied in this thesis offered significant benefits over the industry standard catalysts for the same reactions. They offer comparable if not improved activity and selectivity, while also providing greater resistance to sintering and deactivation.

It is intended that this thesis can contribute to the overall discussion regarding the preparation of new catalysts and new preparation techniques for catalysts from a model-system, 'knowledge-based' viewpoint. The surface properties of these materials on the microscopic or even atomic level can allow for greater control in manufacturing and use in reactions.

The arrangement of this thesis contains a journey through the various subjects contained within. To begin with the relatively structurally simple intermetallic compound, ZnPd, was studied. This involved the development of a preparation route and then subsequent surface characterisation. This material was investigated to understand the characteristics of the clean surface in the idealised system of single crystals. Following from this, the next step was to study the quasicrystalline complex intermetallic compound icosahedral Al-Cu-Fe. This sys-

tem provided the opportunity to study the role of quasicrystallinity in catalysts by recreating Raney catalysts with quasicrystals. This work raised questions about the behaviour of quasicrystals during chemical etching, and the role of crystallographic direction on leaching resistance. By studying a quasicrystal sample that contained surfaces and structure related to both periodic and aperiodic systems, which was possible with a decagonal Al-Ni-Co sample, the relationship between crystallographic direction and leaching resistance could be investigated. A first step towards performing model catalytic studies with molecular deposition is understanding the adsorption properties of a material. Using a test molecule and a clean single grain quasicrystal surface the adsorption properties of Al-Cu-Fe were investigated as a preliminary study, which will lead eventually to model catalytic studies. At the time of submission some of these studies had already begun.

This thesis is arranged in the following manner. Due to the varied nature of the project, each chapter includes its own background and summary of the literature. It is intended that this will allow a more concise introduction to the work undertaken. The remaining section of this chapter (section 1.2) contains a brief description of the main themes and background to provide the context for this thesis, such as the role of the intermetallic compounds in catalysis and the role of model UHV studies in catalysis. Following from there, Chapter 2 provides an explanation of the various experimental systems and techniques used in this study. This includes details of UHV, spectroscopy, microscopy, diffraction and synchrotron techniques.

Chapter 3 is an experimental chapter detailing the work done to prepare and characterize the surface of an intermetallic model catalyst ZnPd. The bulk alloy of this crystal has yet to be studied using surface science techniques and this chapter provides the first atomic scale microscopy on this crystal to be achieved. It also provides an insight into the possibilities for studying polycrystalline material in UHV, a practice which is not well established in the field.

Raney prepared catalysts are common in industry. Chapter 4 details the work done to replicate Raney style preparations on a well-orientated single grain quasicrystal. These materials have been shown to be stronger candidates as catalysts than their crystalline material, but as yet there is still a lack of understanding of the role of the quasicrystalline structure. It was attempted to determine the role, if any, on the leached region of crystal from the bulk. The leaching kinetics of the quasicrystal suggested a strong role of the crystallographic orientation, so to investigate this further a well orientated single-grain quasicrystal with multiple, well-defined surfaces exhibiting both periodic and quasiperiodic ordering was leached. Chapter 5 describes attempts to investigate the role of aperiodicity in the chemical leaching process.

Catalysts must have isolated adsorption sites in order to remain active and maximize the surface area of the material. To investigate the effect of different active site lattices, C_{60} was deposited on three different surfaces of icosahedral quasicrystals, with the intention to investigate the effect of aperiodicity on specific adsorption sites. During the experiments detailed in Chapter 6 an epitaxially grown quasiperiodically patterned molecular thin film atop a quasicrystal five-fold surface was formed which was sensitive to the characteristic of the preferred adsorption sites on the different surfaces.

Chapter 7 presents a brief summary of the work in this thesis and offers a perspective on potential future studies.

1.2 Background

1.2.1 Methanol as a Hydrogen Source

Hydrogen is the most abundant element on the Earth, although there is no source of hydrogen in its pure form, apart from traces in natural gas reserves [7]. Therefore hydrogen must always be produced from other substances, most often from the steam reforming of hydrocarbons or alcohols. For portable use, especially within the motor industry, hydrogen fuelled cars have all but been ignored by manufacturers and consumers alike. It is difficult to envisage a consumer being prepared to run a hydrogen fuelled car with practically no hydrogen supply infrastructure, plus the low energy density of current supply and storage mechanisms [8]. The hydrogen required for fuel cell operation can be produced on board however through the conversion of methanol to hydrogen. The US military have shown interest in the prospect of methanol powered hydrogen fuel-cell vehicles since 1963 [9]. The work was concerned with providing an on-board hydrogen supply for a fuel cell powered submarine. The unit designed was capable of producing between 3 kg and 30 kg of pure hydrogen every hour.

Methanol is unique in its usefulness as a hydrogen storage device due to its sulphur free nature and relatively low activation temperature [10]. It also has a high energy density and a well understood and relatively simple conversion route to hydrogen [11]. Methanol also highlights key requirements for a fuel that is not only easily transportable but could be served by current infrastructure without significant, and costly, modifications [12]. The constituents required for the reforming of methanol are methanol and water. As these two liquids are miscible it is also possible that current fuel delivery systems could provide a methanol-water mix sufficient for the on-board reformer [13], again simplifying the delivery and storage of fuel in comparison to pure hydrogen. However, to take

that viewpoint raises the question of why, in the short term, current hydrocarbon fuels could not be converted to hydrogen? Ignoring the environmental aspect of this argument, methanol is still superior as it has a more attractive steam to hydrogen ratio and a lower conversion temperature [14]. Methanol is also the most attractive alcohol for the process due to having the highest hydrogen to carbon ratio, being just a single carbon atom, three hydrogen atoms and a hydroxyl group.

Methanol has been produced commercially since 1830 and the industry is well developed [13]. The usual conversion route is through the conversion of natural gas, refinery off gas, petroleum or coal into syngas and then the reforming of this product into methanol [15]. Syngas, and therefore methanol, can be made from the partial oxidation of biomass feedstocks. Biomass is a useful fuel as it can be grown anywhere and is the only renewable energy source to exist in liquid form. It also has the benefit of reducing the anthropogenic greenhouse effect.

1.2.2 Steam Reforming of Methanol

The reaction necessary to provide hydrogen from methanol is known as steam reforming of methanol (SRM). This involves the reaction of methanol with steam under certain conditions to provide hydrogen and carbon dioxide. At this point it is worth commenting that methanol steam reforming creates CO_2, which is well known for its greenhouse properties, yet the use of this technology is driven by a desire to be *greener*. Methanol has the highest possible C:H ratio of any hydrocarbon and is entirely sulphur free, so while it is not entirely greenhouse emission free, it is a cleaner option than a petrol or diesel engine.

The ideal reaction that would be desired to create hydrogen from methanol fuel is reaction (1.1). However, where ever SRM takes places the conditions, reactants and catalysts provide the necessary conditions for two other pathways which compete [11]. These are displayed below:

$$CH_3OH + H_2O \rightleftharpoons CO_2 + 3H_2 \tag{1.1}$$

$$CH_3OH \rightleftharpoons CO + 2H_2 \tag{1.2}$$

$$CO + H_2O \rightleftharpoons CO_2 + H_2 \tag{1.3}$$

Reaction (1.1), as already mentioned, is the steam reforming mechanism, (1.2) is the decomposition of methanol, the main competitor in this reaction. The third reaction (1.3) is the water-gas-shift reaction which can take place with the products of the decomposition to achieve the same products overall. As

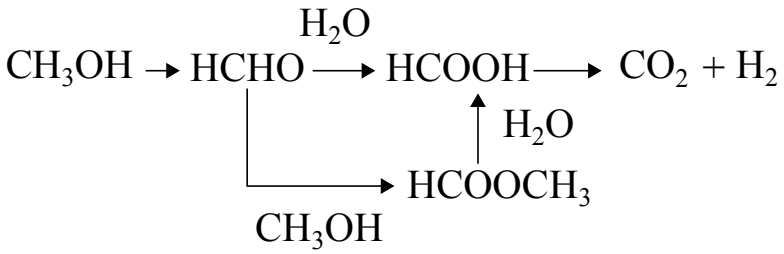

Figure 1.1: Diagram illustrating the reaction route of methanol steam reforming in the absence of competing reactions. (Redrawn from [22])

will be discussed in section 1.2.3, it is desired to have a process which converts methanol to carbon dioxide and hydrogen only. Steam reforming of methanol must be undertaken with high selectivity to avoid carbon monoxide creation [16]. Steam reforming of methanol can be considered an adequate supply of hydrogen as the amount produced is significant, methanol reformate will often contain approximately 60% hydrogen, 15% water, 20% carbon dioxide as well as a small amount of CO (1%) [17, 18].

The reaction is currently carried out industrially on copper-based catalysts. Under these conditions the reaction follows the preferred path and has a high selectivity for carbon dioxide rather than carbon monoxide [19]. Copper-based catalysts have a significant drawback however, in mobile applications where the temperature of the reaction is regularly to the order of 573K the catalyst can become unstable [13]. In these situations the copper catalysts are prone to pyrophoricity (spontaneous combustion), rapid degradation, and agglomeration through sintering at temperatures above 600 K [12, 20]. This would require a reformer to operate at low temperatures, which would cause catalyst deactivation and therefore a reduced lifetime of the fuel cell. The selectivity of the copper based catalyst is, in many respects, the benchmark for a new catalyst with improved stability under reaction conditions. The reaction mechanism on the copper catalyst is believed, although not universally, to begin with the cleavage of O-H bonds on both methanol and water molecules which generate methoxyl (CH_3O^*) and hydroxyl (OH^*) radicals [21]. Formaldehyde (CH_2O) is formed from methoxyl before reacting further with OH to produce hydrogen and carbon dioxide.

The purpose of the catalyst is to not only advance the reaction at an acceptable temperature and rate but to provide the necessary selectivity to carbon dioxide as will be seen in the section 1.2.3. This is of the highest importance when considering methanol as a hydrogen source for portable fuel cell systems.

1.2.3 Fuel Cells

Fuel cells are the device by which the newly created hydrogen will be converted into usable energy, specifically electrical energy. The fuel cell as a concept dates back to 1842 and the invention of the "gas voltaic cell" by Sir William Grove [23]. The basic concepts of a fuel cell involve the dissociation of hydrogen atoms into protons and electrons, the drawing of protons through an electrolytic membrane while forcing the electrons to traverse through a circuit, thus producing electrical current. There are many types of fuel cell but the one which will be discussed in relation to the use of methanol as a fuel is the Proton Exchange Membrane Fuel Cell (PEMFC). This design uses a polymer membrane for an electrolyte, due to good electronic insulation and good hydrogen ion conductance [24]. This membrane is often made from a fluorinated sulfonic acid polymer, which involves a fluorocarbon chain resembling TEFLON© with sulfonic acid groups attached. Either side of the polymer are the anode and cathode, which serve to split the reactant gases into the necessary form to pass through either the membrane or circuit. This is displayed below:

$$\text{anode}: \qquad 2H_2 \rightarrow 4H^+ + 4e^- \tag{1.4}$$

$$\text{cathode}: \qquad O_2 + 4H^+ + 4e^- \rightarrow 2H_2O \tag{1.5}$$

The anode is supplied with hydrogen which is split to protons and electrons, which are attracted to the oxygen at the cathode on the other side of the electron barrier. This has been summarised graphically in Figure 1.2.

The fuel cell itself relies on a precious metal catalyst, often platinum. These catalysts are extremely sensitive to carbon monoxide poisoning, and this is why there is a necessity for adequate methanol reforming to carbon dioxide and hy-

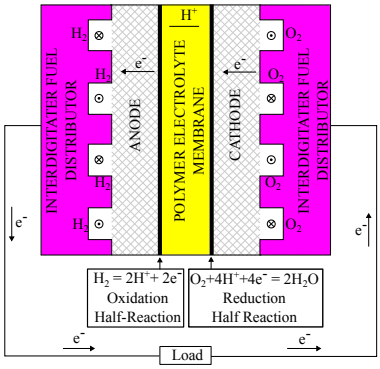

Figure 1.2: Schematic of Proton Exchange Membrane (PEM) Fuel Cell demonstrating the flow of electrons during operation. (Redrawn from [25])

drogen, with minimal CO contamination. Fuel cells are able to tolerate levels of CO_2 which are generated by the SRM process but the reformate could equally be separated into constituent parts after reaction. The performance of the fuel cell drops dramatically after CO exposure and eventually, due to strong chemisorption of CO on catalyst, the catalyst is poisoned and ineffective [17]. The fuel cell is so intolerant of CO that levels entering the fuel cell must be less than 100 ppm (parts per million) but ideally to the order of a few ppm.

The need to incorporate a reformer in the fuel cell design is key, so any additions to the unit as a whole need to be small. The cell and reformer itself must be small, but if the heat from the fuel cell is not sufficient to provide adequate energy to the reformer then anode off-gas can be burnt to heat the reformer. Again, this adds size and weight [24]. Samms and Savinelli, however believed that the heat from the fuel cell would be sufficient to drive the reformer [11]. They describe four theoretical advantages of an integrated reformer:

- Simplification of design (no water-gas-shift reactor)
- Increased overall efficiency (heat from engine to reformer)
- Minimization of system weight and volume
- Inherent system stability (no hydrogen combustion)

The issue of heat is also a challenging area in respect to the reformer catalyst, as already discussed the widely used copper catalyst is unsuited to mobile applications. This drives the need for new, highly CO_2 selective catalysts with greater stability. It is believed that with these new catalysts the development of on board reforming PEM fuel cells can take large leaps forward. Overall, fuel cells are a clear choice for mobile applications in a society where carbon footprints and greenhouse emissions are no longer tolerated, however the cost, difficulty of production, and fragility of catalysts need to be minimised to provide a viable medium term replacement to the reciprocating internal combustion engine.

1.2.4 Heterogeneous Catalysis

Catalysis has become an essential part of modern life without which the world as we know it would not survive. It is required to produce materials, fuel, clean exhaust gases and to produce enough food to support the global population. Approximately 90% of chemicals and materials produced today have involved at least one catalytic process in some way. Although catalysis takes place in living things through the use of enzymes, for example photosynthesis, large-scale human

application of the technology only began in the 20th century. The term catalysis was developed by Berzelius in 1836:

> "Many substances, simple and compound, solid and in a state of solution, possess the power of exercising upon compound bodies an influence essentially distinct from chemical affinity, an influence which consists in the production of a displacement, and a new arrangement of their elements, without their directly and necessarily participating in it ... Accordingly, I shall designate it ... the *catalytic power* of bodies; and the decomposition it produces I shall call *catalysis*." - J.J. Berzelius (1836) [26]

A more modern definition of a catalyst is; a body or material which can induce the phenomenon of catalysis. It enhances the rate of catalysed reaction, and while being intimately involved in the reaction sequence, it is regenerated at the end of it [27]. In heterogeneous catalysis the catalysts and the reactants are in different phases, commonly liquid or gas reactants with solid catalysts.

Possibly the most famous of these processes is the Haber-Bosch process. This used an Fe-based catalyst to produce ammonia from atmospheric nitrogen on an industrial scale. Ammonia is used heavily in the production of fertilizers, and without this process it would be impossible to feed over half the planet's population [28].

The catalytic process is intrinsically linked with the surface of a material, it is the surface atoms and their coordination that determines catalytic activity. At the surface the atoms experience asymmetric bonding environments which leaves free bonds to interact with absorbed reactants and products. In general terms, surfaces with the low coordination of surface atoms have high surface free energy. This will lead to high reactivity for adsorption and strong binding for the adsorbate. Often meaning open surfaces are more reactive than close-packed surfaces. Using single crystals to understand the surface behaviour of catalysts is well developed with a good early example from the group of Somorjai, demonstrating dependence of some reactions of surface termination [29].

Figure 1.3 demonstrates the various morphological features available even on clearly well defined and practically atomically flat surfaces. These various atomic sites, determined by the variation in coordination sites, provide a variety of absorption points and diffusion characteristics which will all affect catalytic behaviour. While real catalytic surfaces are not single crystal, atomically flat surfaces by understanding the energetically favourable sites on these simplified systems, it is possible to determine the mechanics of key processes on real world systems.

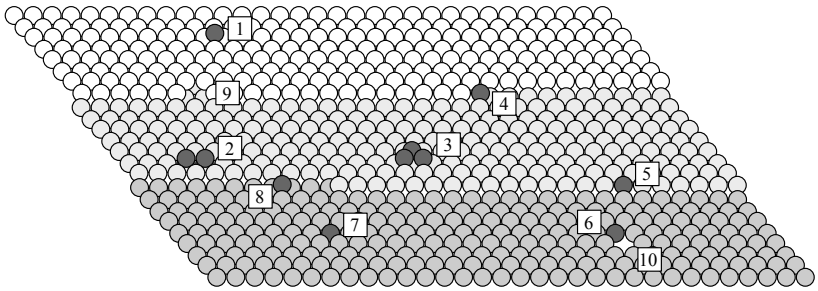

	Atom Type	Top plane co-ordination	Total co-ordination
1	Adatom	0	3
2	Dimer	1	4
3	Trimer	2	5
4	Kink Edge	3	6
5	Step	4	7
6	Terrace Vacancy Neighbour	5	8
7	Terrace	6	9
8	Step Adatom	2	5
9	Step Vacancy	-	-
10	Terrace Vacancy	-	-

Figure 1.3: Crystal surface structure, based on fcc(111) plane with (100) steps, showing different types of atomic and molecular adsorption environments. Adapted from [27].

It is the availability of surface bonding sites that determine the catalytic properties. A catalyst must offer a lower energy pathway for the reactant molecules to rearrange on the surface than in the absence of the catalyst (Figure 1.4).

In Figure 1.4 it can be seen that the energy required for each step is much lower than that required for the gas phase reaction. This, in essence, is the role of the catalyst. It should be observed that the a specifics of adsorption is a key factor in the ability of the catalyst. It is therefore important to fully understand the surface properties to then utilise these to improve the catalyst or catalytic behaviour.

Changes to the surface can cause both positive and negative effects on the catalytic behaviour of the material. This provides the possibility that materials can be improved in their suitability to any given reaction. Thermodynamically, the free energy of the surface can be altered, or microscopically the specifics of adsorption can be altered. Some examples of these modifications are summarised in Table 1.1.

When discussing the positive or negative characteristics of a catalyst, the mark of a successful catalyst is the maximization of the product yield or the minimization of the reaction time for a given yield.

Within this work the three main treatments to be considered when studying the chosen material surfaces are sintering, dispersion and the support. Sintering

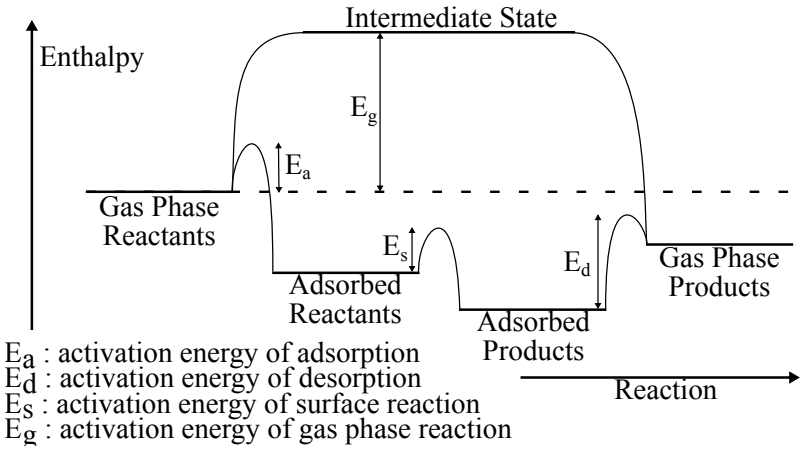

Figure 1.4: Simplified view of the energetics involved in heterogeneous catalysis.

Catalyst Treatment	Probable Effects	Side Effects	Achieved By
Sintering	Loss of activity	Change in selectivity due to changed site type ratio; improved longevity	Thermal/oxidation treatment
Dispersion	Increased activity	Change in selectivity due to changed site type ratio; decreased longevity	More controlled preparation, *in situ* gas treatments (e.g. dispersion of Rh in CO)
Promotion	Increased activity	Can change selectivity, longevity	Addition of alkali salts (e.g. KNO3) during or post preparation
Poisoning	Decreased activity	Can improve selectivity (e.g. Cl in ethylene epoxidation)	Addition of electronegative elements in preparation or during use
Change support	Increased or decreased activity/selectivity depending on dispersion and charge transfer	Can be secondary poisoning or promotion depending on reducibility of the support	In preparation use of different oxidic materials or precursors
Alter pore size	Can alter activity if diffusion limited	Some shape selectivity on reactants/products for microporous materials. Can effect secondary chemistry in oxidation reactants	Use of supports of different structure, or altered preparation method (e.g. ageing or calcination)

Table 1.1: A list of possible catalytic treatments and the associated effects on performance. [27].

is the action of coalescing a powder or small constituents into a larger mass. In catalysis, this is the action of conglomerating many isolated active sites into fewer larger particles during the reaction, either due to the reaction itself or the temperature of the system during the reaction. This results in less active sites and a reduction in surface area of the material. This can also occur in alloy catalysts and is called segregation. By this process, previously separated active atoms will cluster and lose the adsorption properties of the alloy, restoring the single element properties locally [30]. The desire to reduce sintering is key in the development of catalysts, and is a heavy influence in the motivations of this study.

Dispersion is the fraction of catalytic atoms which are present on the surface of the entire catalyst, compared to the number of catalytic atoms in the entire volume of the catalyst [31]. Dispersion is dictated by the size and shape of the particles, and effort is made to maximize the dispersion of the catalyst. By placing catalytically active material on a well chosen support the dispersion can be improved while also reducing the likelihood of sintering and maintaining a high surface area.

For supported catalysts, the support material can strongly influence the performance of the catalyst. It may provide greater resistance to sintering, or provide the required dispersal of the active material. When the support alloys with the catalytic material it can also affect the electronic structure of the system.

The electronic structure of the catalyst plays a vital role in its catalytic properties. The valence band of the catalyst is responsible for the bonding and subsequent un-bonding of the reactant molecules from the surface. This bonding characteristic is important because in order to be a successful catalyst reactants must bond to the surface, but if they bond too strongly the products will not be able to desorb into the reaction mix. Roudgar and Gross summarised this effect;

> "High catalytic activity usually is the consequence of a compromise between a sufficiently strong interaction in order to lead to, e.g. lower dissociation barriers than in the gas phase with a relatively modest binding strength of the products so that they can desorb again."[32]

This was first stated by Sabatier in 1905 [33]. Electronically this is considered in terms of the d-band model, which states that the position of the d-band centre, relative to the Fermi level, will determine the stability of catalyst-reactant bonds [34].

In simplified terms (Figure 1.5), a metal with a d-band centre too high (relative to the Fermi level) will completely fill the anti-bonding state of the molecule and not bond. A d-band centre too low will not offer enough population of the anti-

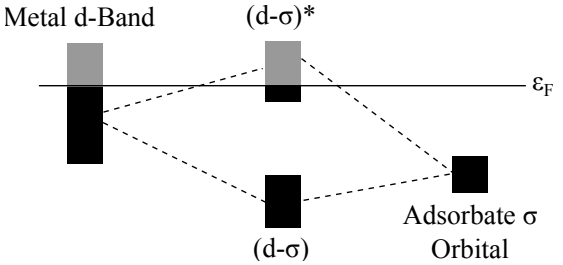

Figure 1.5: Simplified schematic displaying the interaction of the metal surface with adsorbate molecular orbitals. A visual representation of the d-band theory. Redrawn from [35].

bonding states for the products of the reaction to desorb.

In many cases it has been shown that the alloying of metals can allow the alteration of this d-band centre position and provide desirable effects on catalytic behaviour [36, 37]. The d-band model must be used with care however when covalent bonding is present in the system and in case the molecular adsorption alters the shape of the d-band [32, 38].

1.2.5 Intermetallic Compounds as Catalysts

An intermetallic compound (IMC) is a "true compound of two or more metals that has a distinctive structure in which the metallic constituents are in relatively fixed abundance ratios and are usually ordered on two or more sub-lattices, each with its own distinct population of atoms" [39]. They have been considered of interest in heterogeneous catalysis due to the unique characteristics they fundamentally possess. These are caused by exhibiting both ionic and covalent bonding interactions while also containing conduction electrons [30]. Even though intermetallics have been known and used historically, for example brass and bronze, there has been a relatively small amount of research into their properties.

They offer similar motivation to the use of substitutional alloys, by looking to modify one constituent property. Rather than dispersing two or more elements in solid solution, the elements are separated through their crystal structure. The chemical bonding within the crystal structure causes the active sites to remain dispersed and to resist sintering and segregation by drastically reducing the mobility of the atoms in the IMC [40]. This allows IMCs to demonstrate their ability to address the geometrical factors required of catalysts.

This unique mix of bonding in the crystal structure also causes the IMCs to have very different electronic structure to that of its constituents. With these particular blends of electronic and structural properties IMCs are capable of having unique adsorption and desorption characteristics, with therefore unique catalytic properties.

Studies of potential IMC catalysts have demonstrated some excellent candidates for certain reactions such as PdGa compounds for the semi-hydrogenation of acetylene [41–44].

Both ZnPd and PdIn have been investigated with favourable results for the steam reforming of methanol [16, 22, 45, 46]. PdIn has also been considered as a catalyst for the hydrogenation of nitrates or reduction of NO by CO [47, 48].

Research has also shown that the correct choice of initial metals in the compound can provide the desired electronic structure without the drawbacks of the 'cloned' element. Armbrüster *et al.* demonstrated the ability to replace a precious metal, Pd, with an IMC ($Al_{13}Fe_4$) which shared a similar electronic structure and catalytic behaviour but required cheaper ingredients [49]. This was also shown, perhaps counter-intuitively by the work of Tsai *et al.* who demonstrated the IMC ZnPd would mimic the electronic structure of Cu [50]. In this work the surface of a bulk ZnPd sample has been studied in an attempt to characterise the surface to an atomic level and understand its stability and preferred surface terminations. This appears in Section 3.

IMCs also provide the possibility of being used as precursors to catalysts rather than the catalyst itself. Often the role of a good precursor is to provide the required catalytically active sites while ensuring site isolation and stability at reaction temperatures. This general concept was developed by Raney in 1925 and involves the selective removal of one constituent of the alloy until the active species is dispersed in a skeletal, high surface area porous structure [51, 52].

In this work the concept has been extended to use a branch of intermetallic compounds known as complex metallic alloys. These materials have extremely large or, in the case of quasicrystals, infinite crystal unit cells and can have unusual properties. By using the Raney chemical etching method on aluminium based quasicrystals, it was possible to create a model catalytic precursor possessing differing properties to that of regular intermetallic compounds of similar elemental make-up. The details of this experiment are contained within Section 4. Quasicrystals have also been shown to be catalytically active in their untreated form. This has included *i*-Al-Cu-Fe being active for methanol decomposition reactions and *d*-Al-Ni-Co for hydrogenation reactions [53].

1.2.6 Model Catalyst Studies

The studying of single crystal or simplified catalyst systems provides an opportunity to examine a complex procedure or characteristic that cannot be understood when studying practical catalysts. It provides a reductionist approach to remove many factors until an observation can be made in isolation. It is not a case of im-

proving the catalytic performance of a material, but of understanding the reasons for a particular catalysts successes or failures [54].

These studies often take place within high vacuum environments using single crystal samples with surfaces cut along well defined crystallographic directions. This surface science approach allows atomic level of detail and understanding in the study of the material in isolation from external interactions. The bonding between atoms on the surface, and their relation to the bulk structure is an important factor in the understanding of behaviour which may be apparent on the other side of the "materials gap".

As adsorption is such a key constituent of the catalytic process, much work has been done on understanding the adsorption behaviour of well defined surfaces of single crystals. This information can provide key insights into the behaviour of catalysts during reactions. In this work, a buckminsterfullerene C_{60} molecule was used to investigate the adsorption sites on an Al based quasicrystal. While the study contained in section 6 investigated specifically the possibility of templated molecular ordering, C_{60} is commonly used as a test molecule for other adsorption studies in surface science. A large size and electronic sensitivity to the surface make it is an easy molecule to study using STM. Following the use of C_{60} in initial studies, understanding of results using smaller or more complex molecules can be improved or simplified

By understanding structural preferences for surface terminations, reconstructions and adsorption a better understanding of the site isolation or surface sensitive electronic structures can begin to add to the ambition of catalyst development through design [55–57].

1.3 Summary

Hydrogen-powered fuel cells can provide a cleaner, renewable source of energy for the transportation industry. Methanol can reduce the cost and inconvenience of hydrogen technology to the consumer through the use of the steam reforming of methanol. The current stumbling block is the lack of suitability of established SRM catalysts in the mobile environment.

Intermetallic compounds display a clear potential as catalysts for the steam reforming of methanol as displayed by numerous studies. By perfecting the use of these materials it would ultimately be possible to add to the concerted effort to introduce greener technologies to global consumers. Work is needed to greater understand the materials that have been initially investigated in order to develop the ideas through a knowledge based approach.

This work aims to provide a greater understanding of the fundamental char-

acteristics of catalytic surfaces for the steam reforming of methanol, both IMC catalysts and IMC catalyst precursors. By adopting surface science techniques and model-system approaches, the key surface characteristics as surface stability and structure can be obtained.

Chapter 2

Experimental Methods and Techniques

In order to study a surface, an initial decision must be made regarding the length or depth scale from which the measurements are to be made. Based upon this decision, it is then possible to implement certain techniques in order to make the measurements. Information which must come from the very outermost atomic layers of the surface will require the surface to undergo a much more demanding level of preparation and cleanliness compared to observations made on a larger, macroscopic level.

This thesis includes both truly surface sensitive studies and also more generalized studies. In the case of ZnPd (see Chapter 3) the use of surface sensitive techniques allowed the determination of atomic structure at the surface as well as chemical composition and bonding of the surface. In Chapter 6 Scanning Tunnelling Microscopy was used to understand the adsorption properties of the five-fold *i*-Al-Cu-Fe quasicrystalline surface. Both these sections required the use of Ultra High Vacuum to maintain sample cleanliness and reduce the possible complexities.

The study in Chapter 4 was not truly surface sensitive although Atomic Force Microscopy was attempted in air. Following the treatments performed on the *i*-Al-Cu-Fe quasicrystal, there was no hope of the surface being flat or ordered enough for surface sensitive structural studies. Most of the microscopy was performed in air or medium vacuum. Chemical information was obtained through surface sensitive spectroscopy to complement the structural findings.

A summary of the methods and techniques used in this study is presented in this chapter.

2.1 Experimental Methods

2.1.1 Ultra High Vacuum (UHV)

When it is necessary to study the atomic surface of a crystal it is imperative that the experimenter can be certain of the nature of surface with which they are working. In atmosphere, samples are constantly being bombarded with molecules from the air. If one assumes that every molecule that impinges upon the surface, subsequently sticks then the surface of the crystal will be completely covered (and thus unrecognisable from its 'ideal' state) within 10^{-9} s at atmospheric pressure and room temperature. If the pressure is reduced to 10^{-10} mbar (1 mbar = 0.001 atm) the time taken for the surface to be entirely covered, again assuming a sticking coefficient of 1, is increased to roughly 8 hours. This is an acceptable time to perform experiments and make observations of the surface.

Of course, being able to place a sample into UHV and keep it clean for 8 hours is good but of little use unless experiments can be performed. As will be seen in later sections, most experimental techniques which study the surface require some 'probe', most often a particle which is brought into contact or near contact with the surface, and then the result measured. It is therefore vital to make certain that it is possible for these particles to reach the surface unhindered. An important idea, with regards to this requirement, is the mean free path of a particle. This is the average distance a particle travels between interactions. At atmospheric pressure a particle can expect to travel roughly 10^{-8} m in between interactions, this is obviously far too small a distance to be of practical use. If the pressure is reduced to 10^{-10} mbar, as was the case when demonstrating surface contamination, the mean free path is increased to 10^{5} m, much larger than any vacuum chamber. This means that within the UHV pressure range, the experimenter can be confident of the probe's ability to reach and interact with the surface. In addition, any released particle has a realistic chance of reaching any detector.

2.1.2 Sample Preparation

To measure the properties of a surface, it is important to make certain that the surface is clean. Thus, a process of removing both macroscopic and microscopic layers of impurities from the surface must be undertaken to provide the desired levels of cleanliness.

An initial process of polishing is used to clean any thick layers of impurity or to restore the surface to a repeatable starting point. To achieve this, the surface is mechanically polished by hand using successively finer grades of diamond polish

until a mirror finish void of scratches is achieved (the finest grade being 0.25 μm). At each step the crystal is cleaned in methanol using a sonic bath to remove the diamond paste from the previous step.

To then achieve a clean surface free from the impurities due to preparation in air, cycles of ion bombardment and subsequent annealing are used. Ion bombardment involves the acceleration (1-2 keV) of ionized Argon gas toward the sample, causing collisions at grazing angle to remove the outer layers of the surface (Figure 2.1). The angle of the sample surface relative to the ion beam can be varied. This is mostly used to maximize the current being generated from the interaction of Ar^+ ions on the sample, a measurement analogous to the bombardment intensity. After this step, the surface can be used for many chemical analyses but structural studies require the surface to be recreated and, ideally, made atomically flat. This is achieved through the process of annealing the crystal at a determined temperature and for a set time. Different samples will require different preparations although there are commonalities. In practice the sputtering conditions remain unchanged, and only the annealing temperature and duration is varied. Annealing temperature can be considered characteristic of the individual sample and is determined through careful consideration of melting and vapour pressures under vacuum conditions. Annealing duration is empirically determined to be the shortest time required to achieve atomically flat terraces large and frequent enough to perform suitable data analyses.

Sputtering will not affect each surface atom uniformly, often some elements are removed much more readily from the surface under sputtering than others. Prolonged sputtering can lead to a non-stoichiometric surface composition, sometimes dramatically. The other function of annealing is to replenish the surface to bulk composition, or an energetically favoured surface composition. QCs are found to be most often bulk terminated, and annealing is important to return

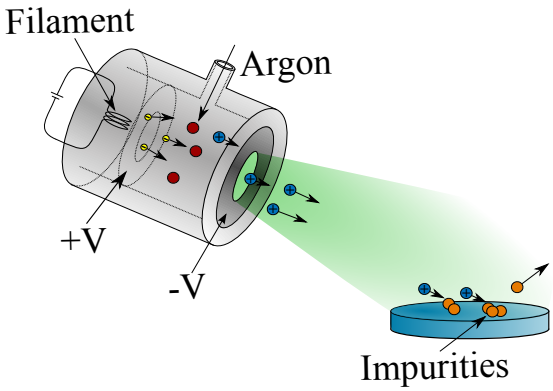

Figure 2.1: Operational setup of an Ar^+ ion gun during the sputtering process. Momentum transfer from the incident ions causes the impurity species in addition to the substrate material to be removed.

the surface to a bulk-terminated, quasicrystalline, stoichiometric state. In other intermetallics the effect of sputtering and annealing on surface composition must be thoroughly investigated and can lead to large changes in surface composition [58].

2.1.3 Surface Modification

When studying the clean surface of a crystal is not the sole focus of a study, it is necessary to understand how a surface reacts to different modifications. This may be to understand surface stability, chemical reactivity, epitaxial ordering or catalytic activity among many others. In the work of this thesis two different types of surface modification have been used; leaching and molecular deposition.

Leaching is a process by which a certain element or species is removed from a material chemically. In the case of this work, it was the ability of high concentration alkali (NaOH) to remove Al from Al based quasicrystals. This was done in two methods. The first method was to maintain a droplet on the surface of the crystal by using a pipette. This allows a clear definition to be observed between leached and unleached regions. The second method was to immerse the surface or surfaces of the crystal in a reservoir of solvent, as seen in Figure 2.2. This benefited from creating homogenous leaching conditions across the surface.

Molecular deposition was carried out using 'homemade' evaporators (see Figure 2.3 for layout) which consisted of a glass tube sealed at one end surrounded by a thoriated tungsten filament. By heating the filament the material inside the glass crucible is brought to sublimation temperature, and leaves the glass tube. Although the directionality of the evaporator is provided by the hole at the end

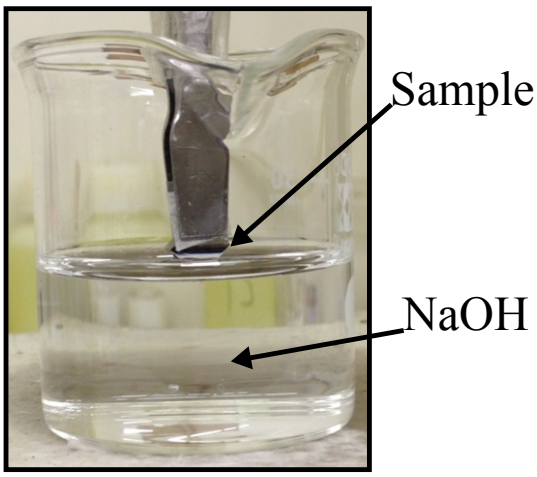

Figure 2.2: Set up for leaching of QC samples in NaOH solution. The sample is suspended to the point where the surface just meets the solution.

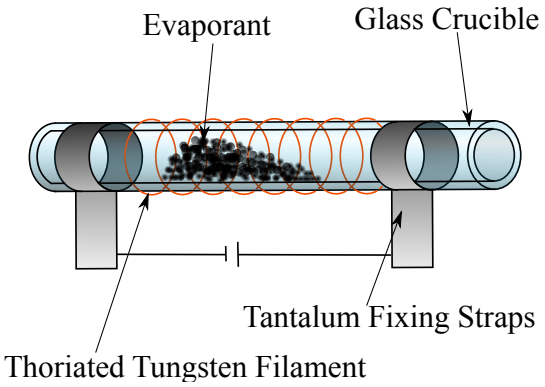

Figure 2.3: Schematic of 'home-made' molecular evaporator. The heated filament causes the evaporant to sublime and diffuse along the tube towards the sample.

of the tube, the sample-evaporator distance must be minimised as the evaporants escape through a large solid angle. The flux of material arriving at the surface of the sample is therefore dramatically reduced with increasing distance. These evaporators are a very simple design but are reliable and ideal for deposition of organic molecules with low sublimation temperatures.

2.2 Spectroscopy

2.2.1 X-ray Photoelectron Spectroscopy (XPS)

X-ray photoelectron spectroscopy can claim to be one of the most popular surface chemical analysis tools available to the surface scientist. The technique makes use of the photoelectric effect:

$$E_B = hv - E_K - \varphi \tag{2.1}$$

first postulated by Albert Einstein in 1905 for which he subsequently won the Nobel Prize in 1921 [59]. The technique itself was invented and pioneered by Karl Siegbahn, for which he also won a Nobel Prize [60].

The surface atoms of a sample are bombarded by photons of a specific energy, which causes excitation of the electronic states within the atoms. This causes electron emission from the surface in line with the photoelectric effect. This means the binding energy E_B can be determined from the kinetic energy of the emitted electron E_K, the energy of the incident radiation hv and the energy required to liberate and electron from the Fermi level to vacuum, work function φ (as in equation 2.1). While the equation above refers to the work function of the material undergoing the photoelectric effect, in XPS the work function of the detector is used [31]. This is because the sample and the spectrometer are in

electrical contact and their Fermi levels are aligned [61]. This can be seen in the diagram in Figure 2.4. An illustration of the basic mechanisms carried out in the electronic states of atoms during XPS is given in Figure 2.5.

Within a laboratory equipped with XPS the choice of incident photon energy is limited to the choice of anode from which the x-rays are generated. Most common are Mg and Al sources. Within an x-ray source, high energy electrons are accelerated toward a water-cooled metal target, resulting in the production of characteristic x-rays. This x-ray production follows a similar process to that in Figure 2.5, following the removal of the core-level electron the electrons in the atom rearrange. Less tightly bound electrons relax from the higher levels to the core level, resulting in the emission of a photon. Lab sources of Mg and Al have prominent emission doublet peaks from electron vacancies in the K-shell. This produces two peaks; K_α and K_β on a continuous bremstrahlung background. Mg and Al have K_α energies of 1253.6 eV and 1486.6 eV respectively. When referring to X-rays the Siegbahn notation is used rather than atomic level notation which is used for subsequent electrons. The relation can be seen in Figure 2.6.

In experimental setups without a monochromator, this can cause 'satellite' peaks in the spectra where photoelectrons produced from both K_α and K_β x-rays are recorded. Using a monochromator crystal and diffracting the x-ray beam removes K_β photons until only the K_α photons are remaining in the beam. This removes features such as the satellite peaks. The work in this thesis was not conducted with a monochromated XPS system.

Once liberated from the surface the electrons are energy filtered by a series of electrostatic lenses, which focuses them on the entrance slit to the hemispherical analyzer (Figure 2.7) . The hemispherical analyzer applies a repulsive, negative bias on both inner and outer surfaces of the analyzer allowing a certain energy window or pass energy for the electrons which enter. The system can be operated in two methods either fixed analyser transmission mode (FAT) or fixed

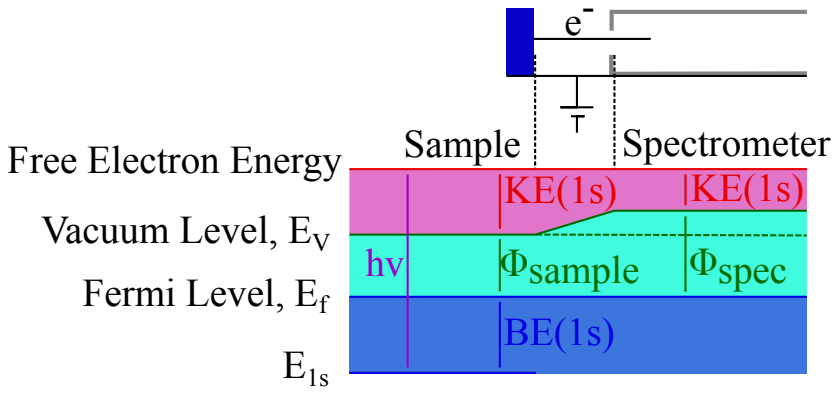

Figure 2.4: Band structure of XPS sample compared to spectrometer.

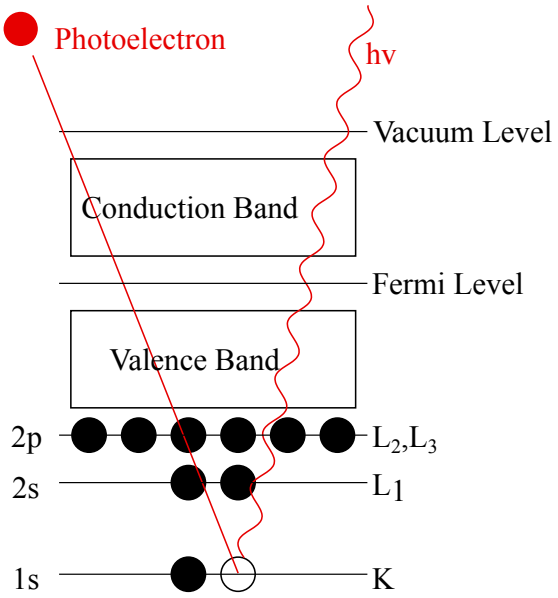

Figure 2.5: Photoemission process in XPS

retardation energy mode (FRR). In FAT mode; the electrostatic lenses either retard or accelerate electrons so that all electrons enter the analyser with the same kinetic energy. This energy will be equal to the pass energy of the electron energy analyser. In this mode the biases of the lenses are varied so that electrons with a specific initial kinetic energy are focussed on the analyser entrance slit and retarded or accelerated to the pass energy of the analyser. In FRR mode, the analyser pass energy is also adjusted to maintain a constant value for the value of initial electron energy divided by the pass energy. In this work all data was taken in FAT mod, which is able to provide a greater signal intensity at low kinetic energies.

Due to the quantization of core electron levels in solid-state atoms, the spec-

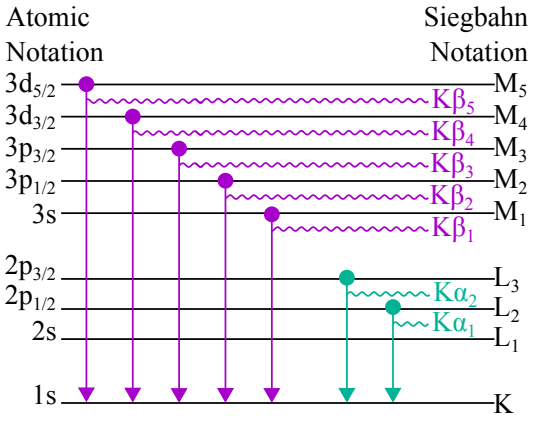

Figure 2.6: The relation between Atomic notation and Siegbahn notation for use in XPS analysis.

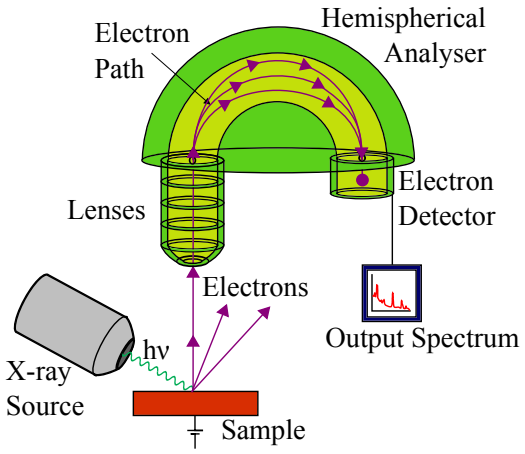

Figure 2.7: Experimental features of an XPS experiment

tra produced in XPS contain clear resonances in intensity characteristic of the elements, or chemical species present. This is due to unique electronic structures for the elemental, molecular or compound species.

The electron detector measures the current created by the incident electrons. The number produced from the sample is far too small to accurately measure the current, for the detector to function correctly an electron multiplier must be utilized. This involves applying a high voltage to a tube with a very high resistance coating to inhibit the electrons passing through the walls. The coating will absorb an incident electron and then emit an increased number of secondary electrons. This produces a cascade of electrons causing the signal to be massively amplified.

The number of electrons collected within the detector can be used to deduce the chemical composition at the surface of the crystal. Although the x-rays probe several microns into the surface, only photoelectrons from the outermost layers reach the detector with the characteristic energies associated with the core levels. Photoelectrons from deeper within the crystal are likely to interact with atoms in crystal and lose energy through inelastic collisions. This creates a continuum of detected electron energies which manifests in the spectra as a continuous background intensity. Other features of the spectra include 'final-state' effects such as shake-up, shake-off and plasmon peaks. Also prominent are peaks due to the Auger process, whereby an electron is released to relax the atom after electron rearrangement following the creation of a core-level hole.

Comparison of the intensities of the peaks in XPS is not a appropriate way of determining surface composition. To achieve this aim it is important to compare the relative intensities of the spectra. Different elements will respond differently to the x-ray bombardment, either by having a lower cross section for interaction or by emitting electrons that have a higher chance of recapture inside the crystal.

The analyzer will also have differing efficiencies of electron detection depending on the energy of the electrons. Peak intensity correction was performed using normalization factors derived from the characteristic response of the analyzer, the photoionization cross section of the elements' transition and the inelastic mean free path of the emitted electron. The transmission function of the analyzer was used as below [62–65];

$$ATF = \left(\frac{a^2}{a^2 + r^2}\right)^b \tag{2.2}$$

where a and b are specific to the analyzer and r is the kinetic energy of the electron E_{k} divided by the pass energy of the analyzer E_{p}. The pass energy is the energy window chosen for each point along the spectrum when performing a scan.

$$N = ATF \cdot \sigma \cdot \lambda \tag{2.3}$$

where N is the normalization factor, σ and λ are the photoionization cross section and inelastic mean free path respectively. The inelastic mean free path was calculated using the Tanuma Powell Penn formula [66–68] shown below in equation 2.4a.

$$\lambda = \frac{E}{E_p^2\left[\beta \ln\left(\gamma E\right) - \left({}^{C}/_{E}\right) + \left({}^{D}/_{E^2}\right)\right]} \left(\text{Å}\right) \tag{2.4a}$$

$$\beta = {}^{-0.10+0.944}/_{\left(E_p^2+E_g^2\right)^{0.5}} + 0.069\rho^{0.1} \tag{2.4b}$$

$$\gamma = 0.191\rho^{-0.5} \tag{2.4c}$$

$$C = 1.97 - 0.91U \tag{2.4d}$$

$$D = 53.4 - 20.8U \tag{2.4e}$$

$$U = {}^{N_v\rho}/_{M} = {}^{E_p^2}/_{829.4} \tag{2.4f}$$

where ρ is the density (g cm^{-1}), M is the atomic weight, $\mathrm{N_v}$ is the number of valence electrons per atom, $\mathrm{E_g}$ is the band-gap energy (eV) for nonconductors and E is the electron energy in eV. The photoionization cross sections were taken from data tables by Yeh and Lindau [69]:

$$I = {}^{I_0}/_{N} \tag{2.5}$$

I represents the corrected relative intensity and I_0 is the measured intensity. By performing this correction the intensities of transition peaks can be compared and used to obtain a composition of the surface.

A full understanding of the chemical environment at the surface can also be obtained by careful consideration of both peak shape and peak position. The peak position is a key indicator of a change in chemical environment of the atoms. Often only small shifts are observed in the spectra but these form key insights into the determination of chemical species at the surface. The first step before any consideration of peak shape is to correctly approximate the contribution from the inelastic background. There are several functions that do this by numerically calculating best estimates, there is no universal background fitting function that provides an absolute representation of the background counts in the spectra due to inelastic interactions. It is important when correcting for the background to check that the results are physically possible. One example of this is that the $2p_{3/2}$ and $2p_{1/2}$ peaks should have an intensity ratio of 2:1, due to the electron orbital rules determined from the Pauli exclusion principle. Whenever backgrounds are subtracted from peaks, a fundamental physical rule like this can be used to test the reliability of the procedure.

Spectral peaks from XPS will often contain peaks from different core levels of an atom. In this case component peaks are generated, in most cases, using a convolution of Gaussian and Lorentzian functions. The Lorentzian function is used to simulate the broadening of the peaks due to lifetime effects and the Gaussian function represents the broadening due to instrument effects. The resolution of the instruments used in this study were 1 eV at a pass energy of 20 eV and 1.5 eV at a pass energy of 50 eV. Wide scans were collected at a pass energy of 50 eV, and detailed scans collected with a pass energy of 20 eV. A mixture of the two line-shapes mentioned were used in analyzing the quasicrystal catalytic precursors and in understanding the chemical bonding on the surface of the intermetallic ZnPd. In ZnPd, however, the use of an asymmetric component was required and a Doniach-Sunjic line shape was used. In the case of metals, it is also important to consider any asymmetry characteristic of the peak. In most cases line shapes can be found from data repositories and used to generate component curves. All XPS data in this thesis was analysed using the CASAXPS software [70].

2.2.2 Ultraviolet Photoelectron Spectroscopy (UPS)

UPS as a technique is considerably similar to XPS in respect to the fundamental processes that take place in the sample. In this case however ultraviolet light is utilized to excite the atoms of the surface. The technique is powerful in measuring the energy states near the Fermi level because of the increased resolution. This can be interpreted as a representation of the density of states at the Fermi level.

The UV lamp used contains an electron gun which ionizes incoming helium

gas. The He is released into the UV source which has to be pumped separately to maintain UHV in the adjoining chamber. It is vital for the source to be directly connected to the chamber, any window would absorb too much UV to make it practicable. The relaxation of the helium ions causes characteristic photons to be emitted in the UV range. There are two transitions for helium that are of significant use, due to the very sharp spectral lines they produce. The transition between singly ionized helium atoms and doubly ionized helium ions, giving 21.21 eV and 40.82 eV respectively. The He lamp used in this thesis produced He I ions and an incident photon energy of 21.21 eV. These energies allow for the study of a material's valence electrons, which are the electrons responsible for chemical bonding in the sample.

The same processes take place following UV photoionization of the sample surface as following x-ray photoionization. However due to the resulting electron emission from the valence band, the technique provides an insight into the nature of bonding in the surface region. It also allows an understanding of the density of states near the Fermi level. The technique can be particularly important when investigating the nature of any adsorbed molecules on the surface, where one can measure molecular orbitals.

2.2.3 Energy Dispersive X-ray Spectroscopy (EDX)

The result of bombarding a sample with photons to generate electrons has been discussed but the reverse can also be used to find valuable information about a sample. This is the case in EDX where the sample is bombarded with electrons (often in conjunction with an electron microscope - see Section 2.3.1) and the characteristic x-rays emitted are measured as a spectrum. Just as characteristic photoelectrons are emitted, the atom will have a characteristic x-ray emission based on the relaxation of the atom from its excited state. These x-rays are named by the transition which takes place to relax the atom. If, following the emission of a K shell electron, an electron from the L shell takes that place the atom will emit an x-ray known as the K_α photon. If an electron from the M shell takes its place then a K_β photon is ejected. The first letter describes the shell from which the electron was removed and the second character describes the shell the replacement electron came from in relation to the first. This is the same effect as has been utilized by the x-ray or UV source in the previous sections.

The emitted x-rays are detected using a semiconducting device with a large bias across a p-n junction. When the x-ray passes through the material, it ionizes with atoms in the semiconductor and creates a cascade of free electrons and holes. These are then swept by the bias to electrodes which measure the current.

This then creates the signal, whereby the energy of the photon is determined by detecting the current from the photon once it has fully deposited its energy within the crystal.

EDX is a useful technique for elemental analysis but does not have the precision or detail of XPS. It also lacks true surface sensitivity as the information depth (the depth of the material from which emission can be detected) is of the order of 1-2 μm. Despite these limitations the technique holds several benefits to the user. EDX is often combined with electron microscopes forming an ideal side-by-side setup, there is also not the same stringent need for UHV, as medium vacuum is sufficient (10^{-6} mbar). EDX also benefits from an ability to modify the beam diameter *in-situ*, meaning the experiment can contain a large area elemental analysis or a spectrum from a small region. This makes the technique useful for materials traditionally difficult to analyze with surface science techniques, such as polycrystals or powders.

2.3 Microscopy

2.3.1 Scanning Electron Microscopy (SEM)

The resolution limit of microscopes which use light in the optical wavelength range is a few hundred nanometres at theoretical limit. For the understanding of smaller length scales it becomes necessary to utilize a different diffracting particle. The theoretical resolution limit when using diffracting beams of electrons is less than an Angström. This makes the use of an electron microscope highly attractive for understanding surfaces of materials to a small scale.

The scanning electron microscope (SEM) uses an electron beam focused to a small area which is then rastered across the surface of the sample. Electrons are generated from a filament (either thermionic emission or cold cathode discharge) and then accelerated with an accelerating potential between 15-30kV. The beam is passed through a series of condenser lenses, scanning optics, objective lens and detectors before reaching the sample. The set up can be seen in Figure 2.8. This causes an electron probe width of 1-10 nm at low beam currents but 0.1-1 μm for higher beam currents [71]. The magnification of the SEM is controlled by maintaining the image size at the screen (historically a Cathode Ray Tube), but reducing the deflection of the scanning coils. In relation to previously discussed techniques it is relevant to mention that SEM does not take place in UHV. In order for the use of an electron beam it is necessary for vacuum, however standard SEMs are operated in the 10^{-6} mbar region and differentially pumped to maintain an improved vacuum around the filament.

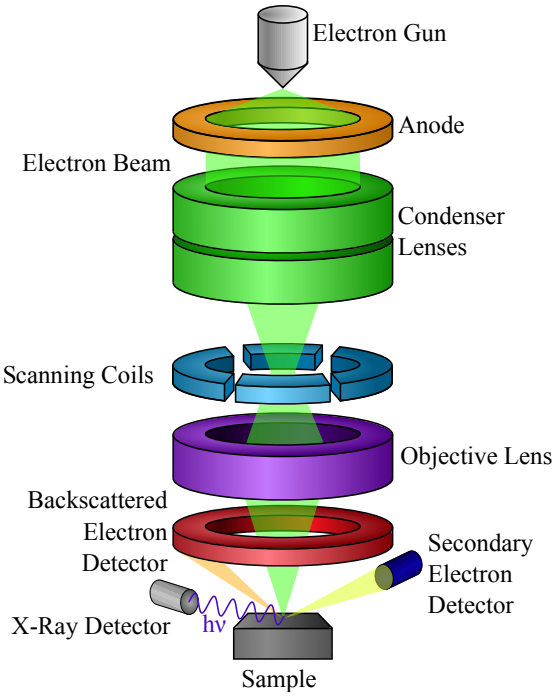

Figure 2.8: Schematic of Scanning Electron Microscope in operation.

One is not able to truly refer to SEM as a surface sensitive technique, in the sense that although the technique can give valuable information about the surface of a sample, the information is gained from much deeper than just the top, or top few atomic layers (Figure 2.9). This is because the interaction volume for SEM is large in comparison to genuine surface sensitive techniques. It is not simply the penetration depth of the electrons that causes this but the lack of discrimination on the electrons that are liberated from the sample. In SEM characteristic electrons are counted along with the inelastically scattered electrons. What this does mean is that SEM can be used in different ways to investigate different characteristics of the material. As previously discussed in Section 2.2.1, the x-rays released can be utilized to obtain chemical information about the surface. The two different types of emitted electrons (Auger electrons are not specifically considered in standard SEM) are able to produce two different contrasts in imaging.

For topological images of the surface, secondary electron imaging is commonly used. This involves detecting the low-energy (<50 eV) electrons emitted from the secondary processes within the sample. Electrons are accelerated toward the detector with a positive potential of approximately +1 kV across an outer grid. Once through the grid an accelerating potential of several thousand V is applied to sufficiently energize the electrons to activate the scintillator detector, which then provides signal to the photomultiplier tube and light detector via a light pipe. This type of detector is known as the Everhart-Thornley detector. In this mode, contrast is dependent on escape depth from the material. Steep surfaces

and edges can therefore appear brighter than the surrounding regions, providing a three dimensional appearance.

Backscattered electrons are the higher energy electrons emitted from the material, which have elastically interacted with the atoms within the interaction volume. Heavier elements are more likely to undergo elastic backscattering interactions with the electrons. This makes it possible to create an image where contrast is influenced by elemental species. Although not a chemical map in the sense of scanning auger microscopy, it is useful for identifying different phases, when studying polycrystalline materials or other surfaces with heterogeneous distributions of surface species. The backscattered electrons are of high enough energy that the accelerating grid of the secondary electron detector would be unable to collect the electrons. This is why there is a concentric detector around the beam, either scintillation or semiconductor, to allow a large solid angle and maximum possibility of detection. Another possible technique that can be utilized in SEM is Electron Back Scattered Diffraction. This will be discussed subsequently in Section 2.4.2.

SEM is a powerful tool for microscopy due to the range of magnification. Although the microscope may not be able to provide images focused at the very small level, the ability to start at a large scale and zoom in creates a very usable technique.

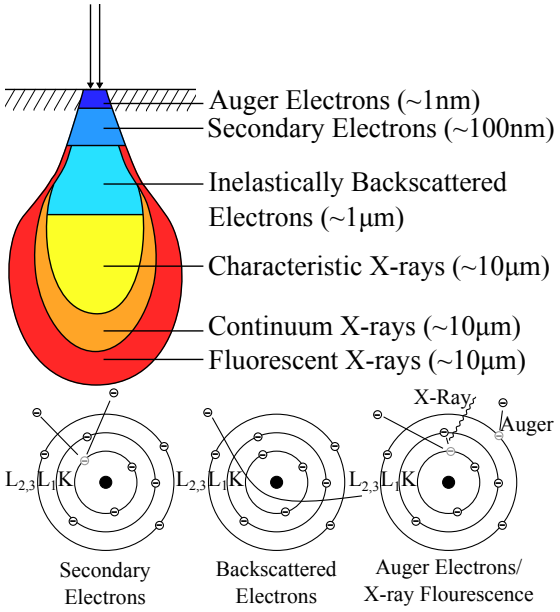

Figure 2.9: Schematic of SEM interaction volume and related processes.

2.3.2 Atomic Force Microscopy (AFM)

AFM is a high resolution, high magnification technique capable of imaging surfaces down to the atomic scale. The technique was originally realized by Binnig et al while working in IBM Zurich in the 1980s [72]. AFM has three modes; contact, tapping and non-contact. In this thesis all work carried out with AFM used contact mode although the other modes will be discussed briefly for completeness.

The basic operation of an AFM in contact mode can be seen in Figure 2.10. The basic components of an AFM are the tip, cantilever, laser and photodiode. A laser is shone onto the back of a cantilever with the reflection being positioned onto the photodetector. The tip is brought into contact with the surface and the sample is rastered underneath relative to the tip. As the height of the tip is changed due to height changes on the surface, the laser is deflected to a different part of the photodetector. This change in laser position is then used to generate a height map of the scanned area, as well as being used to drive a feedback loop which continually attempts to return the laser light to its original position. This can avoid the cantilever being over or under stretched. This is the process used in contact mode.

Surface damage or scratching can be a problem when using contact mode, especially when surfaces are soft or fragile. Tapping mode, while still involving contact with the surface, reduces the chance of damage. Rather than allowing the tip-cantilever system to be 'passively' scanned across the surface, in tapping mode the cantilever is driven with an oscillating force close to its resonant frequency [73]. This creates a large amplitude oscillation in the Z direction. The system is set up to allow the tip to only just touch the surface at the negative maxima of its z oscillation, under scanning conditions this provides a periodic touch of the surface. If the tip touches the surface at a higher point, or indeed misses the surface altogether, this changes the oscillation and the change in frequency can be measured, again creating a topological height map of the surface, this time

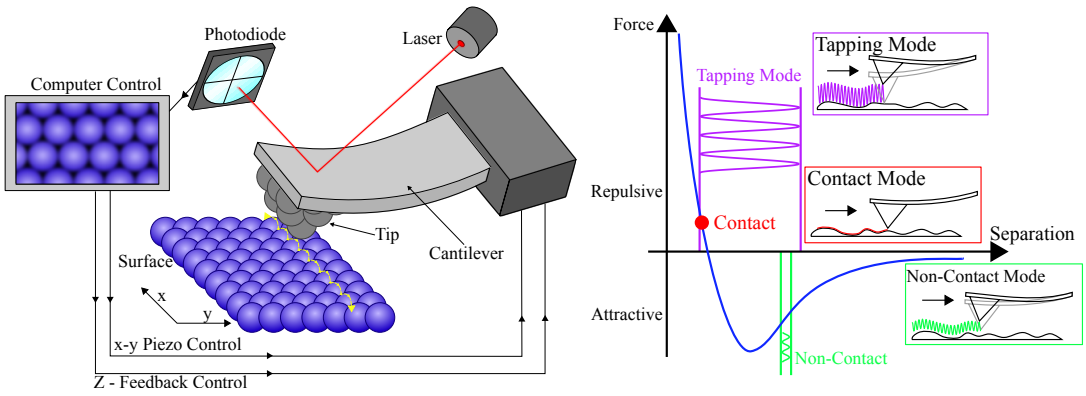

Figure 2.10: Basic Operation of Atomic Force Microscope.

with only a small amount of contact.

Non-contact mode continues the idea of tapping mode but takes it to its logical extreme. In this system the tip-cantilever is driven with an oscillation and held just out of reach of the surface [74]. As the surface becomes closer to the tip's oscillation region, small changes to the tips oscillation can be detected and an image can be created. This method allows a complete separation from the surface reducing the effects of the tip. There are two types of non-contact AFM, frequency modulation and amplitude modulation. In frequency modulation mode, the tip is driven at resonance and the small changes in frequency due to surface force interactions are recorded and used to drive a feedback loop. In amplitude modulation the tip is held just above its resonant frequency, as the tip-surface distance changes, as does the resonant frequency of the tip. This induces changes in the amplitude of the oscillation which again are used to drive a feedback loop and create an image of the surface.

AFM has been shown to be an incredibly high-resolution technique. Researchers at IBM Zurich were able to image individual bonds of a pentacene molecule by picking up a single CO molecule and using it as a tip (see Figure 2.11) [75] . The technique also benefits from an increased level of robustness in comparison to other SPM techniques such as scanning tunnelling microscopy. It is more capable of imaging rough surfaces, and in the case of tapping or non-contact mode the tip is much less susceptible to damage. AFM does not necessarily require UHV, will work on non-conducting surfaces and can also work through liquids. It is capable of damaging surfaces which are particularly vulnerable to scratches and holes created by the tip.

2.3.3 Scanning Tunnelling Microscopy (STM)

Binnig and Rohrer were awarded the Nobel Prize in 1987 for their discovery and development of scanning tunnelling microscopy (STM). The technique is

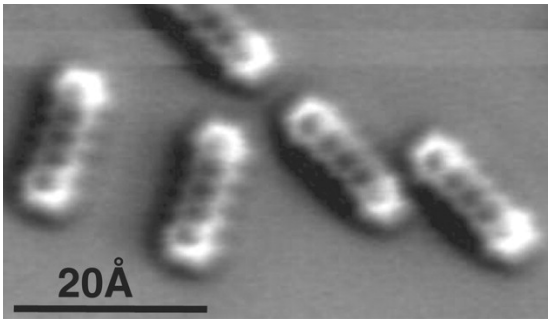

Figure 2.11: AFM image of pentacene molecule including bonds. Image modified from [75].

capable of not only high resolution imaging of surfaces but also has the ability to manipulate the surface making it a powerful technique for surface science investigations. By scanning an atomically sharp tip across a surface, the change in electron density close the surface can be detected, this will often be a direct representation of surface topology although any assumption to this effect must be made with careful consideration of other factors.

The main principle involved is the phenomenon of quantum mechanical tunnelling. A particle is able to cross a boundary that, classically, it would be unable to do so. An example of this, in addition to the STM, is in α radiation. During α radiation the nucleus emits α particles without enough kinetic energy to break free from the coulomb forces acting on them from the remaining daughter nucleus. The α particle must tunnel through the coulomb barrier to escape the nucleus. If the barrier is narrow enough that the wavefunction of the particle incident upon it would remain non-zero following an exponential drop through the barrier, then there remains a non-zero probability of the particle tunnelling to the other side. In STM the classically forbidden barrier that the electron in the tip is unable to cross is the gap between the tip and the surface. The ability of electrons to tunnel from the tip to the surface is very sensitive to the distance between the two due to the exponential decay of the electrons wavefunction across the boundary. This can be expressed by the equation: $I(d) \propto e^{-Kd}$ where $K = \sqrt{2m\phi}/\hbar$, with I(d) equal to the tunnelling current with respect to the boundary distance d, and ϕ is the average work function of the tip and sample.

Assuming the tip is close enough to the surface for the tunnelling conditions to be satisfied, when a bias is placed between the tip and surface, electrons tunnel across the gap and a current can be measured of the order of nA. This current is the key measurement in the operation of the device. If the tip is rastered across the surface at a constant height the measured current will represent the convolution of topography and electron density at the surface. This signal is then used to produce a current intensity at each pixel of the scan providing a intensity map. This shows the joint density of states of the tip and sample at the Fermi level combined with information about the topography at each pixel, which may be a simple representative of the topology of the surface but will certainly contain information regarding the atomic coordinates. This is known as constant height mode. If the system is optimized to maintain a constant current throughout the scan by changing the tip-sample distance using the feedback loop in the microscope software, again the surface electron density can be scanned in a similar fashion although rather than current intensity, the relative height of the tip is recorded. Constant current mode was most frequently used during this work. It dramatically reduces the possibility of crashing the tip into the surface

when the roughness of the surface is not known. On very flat surfaces and when high scan speeds are required such as in the case of graphite, it is advantageous to use constant height mode as the electronics can record the changes in current faster than a feedback loop could drive the piezoelectric manipulators.

With metal surfaces the scan image can often be considered as representative of the topology of the surface. However once compounds that exhibit covalent bonding or molecules are scanned it can become much less related. Due to the localized nature of the electrons in them, covalent bonds can appear brighter than atoms in the image and careful attention must be given when analyzing STM images. It can also be the case where different atoms from different elements in the surface can have a significantly higher, or dominant, density of states within the scanning conditions and appear significantly brighter than neighbouring atoms without any physical difference in height.

In situations where scans are not accurate representations of surface topology, as described above, a key consideration is the tip-sample bias. Atoms with highly localized density of states may have a preference to tunnel an electron out of their highest occupied molecular orbital (HOMO) into the tip or to receive an electron from the tip into their lowest unoccupied molecular orbital (LUMO). This will dramatically effect the intensity of that atom or pixel in the scan image and is a major factor when scanning molecules on surfaces. This was shown dramatically by Repp and Meyer *et al*, while scanning pentacene molecules [76]. When the bias was set to be somewhere in the molecular band gap the molecule appeared simply as a rod but by using a bias at or beyond the LUMO (positive V w.r.t. tip) and HOMO (negative V w.r.t. tip) the microscope was able to image the orbitals.

The components of STM are shown in Figure 2.12. An atomically sharp tip is held less than 1 nm away from the surface, by maintaining a constant current. A

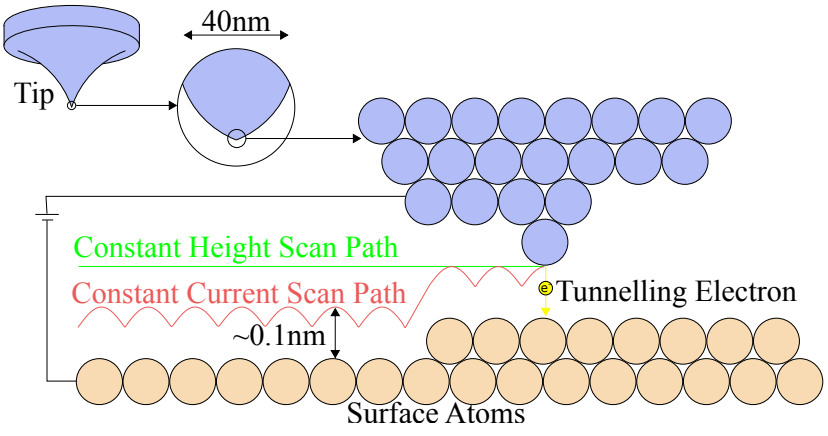

Figure 2.12: Scanning operation of STM.

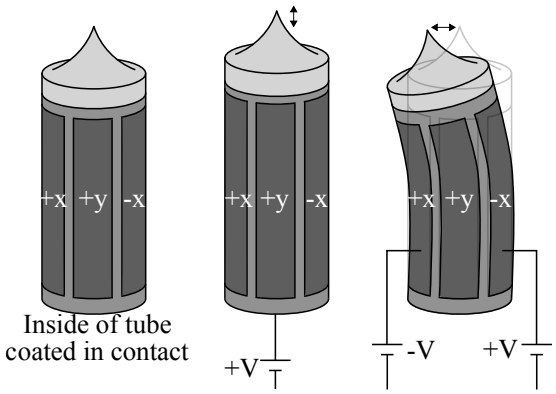

Figure 2.13: Scanning mechanism of STM tip using piezo electronics.

feedback loop dictates the voltages applied to the piezoelectric material attached to the tip which is able to make sub-Ångström sized movements across the surface and in height to maintain the tip-sample separation while scanning across the surface. Piezoelectric material is a substance that will change shape under the influence of an applied bias. There are two common setups for this. One of them is the 'piezo tube' at the base of the tip (Figure 2.13). This tube is coated on the inside with a metal contact and a quartered metal coating on the outside. By applying equal bias on all contacts the tip will grow uniformly in the z direction. Placing opposite bias on opposing quarters grows one and shrinks the other. The tube will bend and move the tip in either x or y. One issue with the use of this piezo setup is that when scanning a large flat area, the tip will unavoidably raise at the edges of the scan region providing a concave view of a flat area. This flaw requires data correction during analysis, which is done with polynomial fitting, although small scan regions do not exhibit dramatic curvature. The other, older, design is that of a orthogonal tripod of piezotubes without any quartering of the coatings. Each one is only capable of increasing or decreasing in its own axis but by combining all three, the range of motion of the tip in 3 dimensions is achieved (see Figure 2.14).

The tip itself is made to be atomically sharp through a combination of *ex-situ*

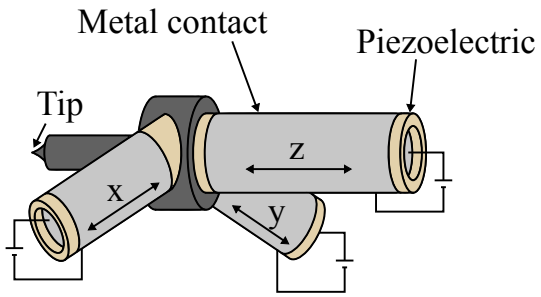

Figure 2.14: Schematic of tripod scanner arrangement of Piezo tubes for STM operation.

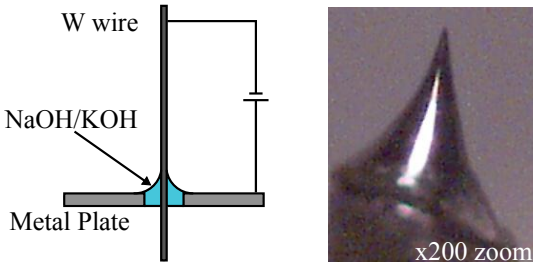

Figure 2.15: Cross section of tip making process and an example of a tip produced using this method.

manufacture and *in-situ* preparation. 'Homemade' tips were produced through the electrochemical etching of W wire suspended through a NaOH or KOH meniscus as shown in Figure 2.15. Once inserted into UHV the tip is cleaned through heating to degas then placed into the microscope. Applying short voltage pulses to the tip will cause the tip to sharpen or remove any molecules or adsorbates picked up by the tip. This process allows the maintenance of sharp, single tips. Occasionally a tip will terminate with an atom in more than one lateral location, leading to the corruption of images by multiple features. This 'multiple tip' is also removed with pulsing. All STM data taken in this study was analysed using either WSxM or Gwydion software packages [77, 78].

2.4 Diffraction

Diffraction is a key tool when studying crystal structure, indeed, by definition a material must exhibit a sharp, definitive diffraction pattern to be called a crystal. While the field of crystallography is mostly interested in the diffraction patterns obtained through the use of x-rays, electrons provide a valuable probe when characterizing crystals, periodic or otherwise. The Braggs were the first to use the coherent interference of photons with crystals to understand their structure, deriving what is now known as Bragg's Law for which they won their Nobel prize in 1915. Electrons can also be used for diffraction due to the wave particle duality postulated by de Broglie in 1924 using their wavelength as calculated by;

$$\lambda = \frac{h}{p} \tag{2.6}$$

where h is Plank's constant, p is the particle's momentum and λ is the wavelength. Davisson and Germer observed an electron diffraction pattern from a Ni single crystal in the first reported instance of electron diffraction. Bragg's law must be

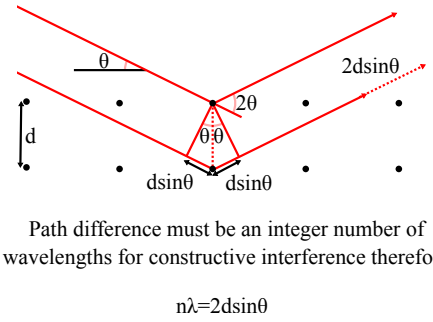

Figure 2.16: Illustrating Bragg's Law.

satisfied in order for diffraction to occur;

$$n\lambda = 2d\sin\theta \tag{2.7}$$

where θ is the Bragg angle, d is the lattice spacing and $n = (h^2 + k^2 + l^2)^{1/2}$. The hkl represents the miller indices of the surface being investigated. Bragg's law is illustrated in Figure 2.16.

Diffraction can also be described in terms of wave vectors using Laue's equations. If an incident electron has a wavevector $\mathbf{K_i}$ and the scattered electron has a wavevector $\mathbf{K_d}$ then the condition for diffraction is;

$$\mathbf{K}_d = \mathbf{K}_i + g_{hkl} \tag{2.8}$$

given that the magnitude of both vectors are equal (elastic scattering) and where the reciprocal lattice is described by;

$$\mathbf{g}_{hkl} = h\mathbf{a}^* + k\mathbf{b}^* + l\mathbf{c}^* \tag{2.9}$$

with **a***, **b*** and **c*** being the primitive vectors of the reciprocal lattice. This can be summarised using the Ewald sphere construct developed by Ewald as shown (in 2D) in Figure 2.17. Diffraction will occur in the crystal from all points in the reciprocal lattice that intersect the Ewald sphere. This means that a knowledge

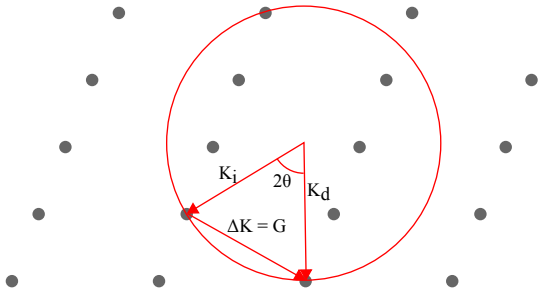

Figure 2.17: Ewald sphere representing diffraction in the reciprocal lattice in 2D.

of the energy of the diffracting probe and the resulting pattern will allow the calculation of the plane separation. When combined with the shared symmetries of diffraction patterns and the crystal structure, diffraction can provide quantitative data about a crystal.

2.4.1 Low Energy Electron Diffraction (LEED)

A key tool in the field of surface science is low energy electron diffraction. This technique makes use of backscattered diffracted electrons to provide information about the surface. Low energy electrons, typically 20 - 500 eV, are used as they ensure the surface sensitivity of the technique. This is evident by comparison with the universal curve [79], an empirically derived relationship between electron kinetic energy and the inelastic mean free path of electrons in a solid (Figure 2.18). LEED only makes use of elastic interactions, so any electrons which are emitted from deeper in the crystal are highly likely to undergo inelastic scattering. These electrons are removed from the scan by the biased grids in the LEED system. This reduces the reciprocal lattice points from the Ewald construction (Figure 2.17) to rods extending out perpendicular to the surface. Diffraction spots in LEED appear when the Ewald Sphere crosses one of these rods. The resulting pattern can be considered as a projection of the reciprocal space lattice of the surface real space lattice.

A LEED system consists of an electron gun directed normal to the surface, focusing and retarding grids and a phosphorescent screen. This system is always contained within UHV to both preserve the required surface cleanliness and the sensitive electron gun filaments. These are usually one of two materials; W or LaB_6. A schematic of a basic LEED system is displayed in Figure 2.19. Electrons are accelerated at a low potential towards the sample, the backscattered electrons are filtered by the suppressor to only permit elastically scattered electrons and filter inelastically scattered electrons. The grid before the suppressor shields the sample and area directly around it from the retarding field. The phosphorescent

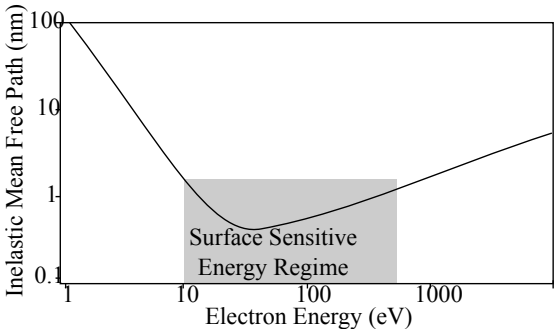

Figure 2.18: The universal curve of electron mean free path in solid matter.

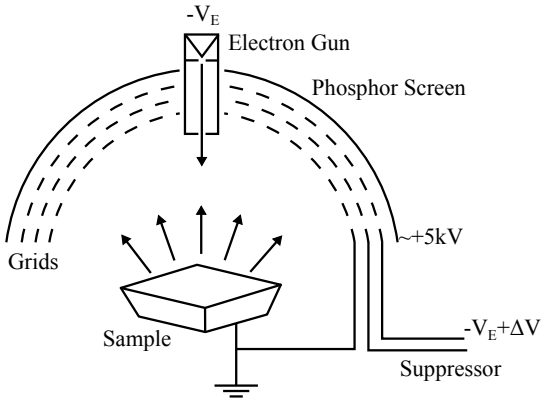

Figure 2.19: Schematic of LEED system.

screen emits light when electrons strike it allowing for a real time display of the diffraction pattern.

LEED patterns can be used to observe the symmetry of an ordered surface for comparison with other techniques such as 2D fast Fourier transforms of STM images. In this study, LEED was used to confirm the ordering of clean surfaces following preparation, before being placed in the microscope. LEED taken using a Low Energy Electron Microscope (Section 2.5.2) was used in this study to determine the surface structure of individual ZnPd grains by calculating lattice constants and comparing it with known models. The coherence length of this technique is of the order of 100 Å, meaning that surfaces which may be too rough for analyses with an STM can provide structural information though diffraction.

2.4.2 Electron Back Scattered Diffraction (EBSD)

Electron Back Scattered Diffraction has been developed as a powerful technique in the understanding of polygrain material surfaces. The technique is able to provide individual grain orientation and phase identification. The technique makes use of diffraction lines first observed by Nishikawa and Kikuchi in 1928 and subsequently known as Kikuchi diffraction [80]. The researchers were investigating electron diffraction from transmission electron microscopy when they also placed a sensitive film in front of the sample to obtain an image from the backscattered electrons. They witnessed patterns of regular arrangements of parallel bright bands forming patterns across the plate that corresponded to the crystal structure of the interaction volume.

Kikuchi diffraction occurs when the sample is suitably thick, and the electrons have sufficient energy to penetrate into this volume. Electrons which are elastically scattered at Bragg angles will form the common diffraction spots, but electrons that are inelastically scattered inside the crystal but then subsequently

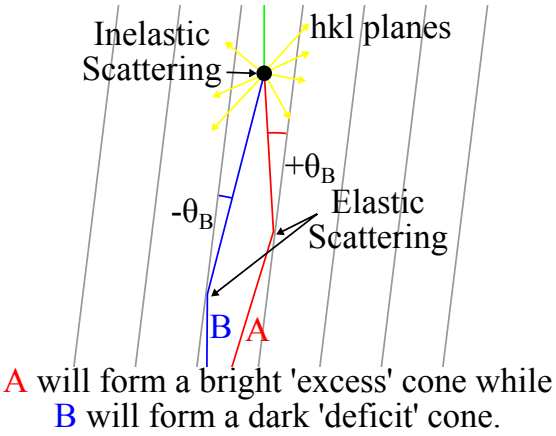

Figure 2.20: Diagram of Kikuchi diffraction from a crystal.

elastically scatter at Bragg angles will form pairs of cones ejected from the sample (Figure 2.20). Only two cones form due to the electrons having to have either positive or negative Bragg angles to the plane. One cone is of significantly higher intensity than the other (the excess line and the deficit line respectively), as one cone will have had a smaller angle of scattering compared to the incident electron and will contain more electrons. This diffraction can take place in transmission mode as well as backscattered mode. Kikuchi patterns can be considered as a projection of the crystal lattice on a flat screen as the distance between the dark and bright lines must be the Bragg angle.

EBSD is now regularly fitted on SEMs and comprises an addition of a CCD camera, phosphor screen and adaptions to the sample stage to allow a 60° - 70° tilt between sample an incident electron beam.

The electron beam is rastered across the surface in similar fashion to regular SEM imaging mode. In EBSD mode the beam stays on each pixel only long enough to record a Kikuchi pattern for that point. The software will then take the pattern produced and solve it for the structure from a library of pattern-structure pairs. It is able to do this with some preliminary information about the unit cell of the crystal being observed [81]. The acquisition software then stores this data in a map. The map can then be imaged using further software to interpret the patterns and provide a colour map where colours represent crystal terminations as summarised in Figure 2.21.

2.4.3 Selected Area Electron Diffraction (SAED)

Selected area diffraction (SAED) is, in general, part of the transmission electron microscope (TEM) setup. It is a powerful tool that allows diffraction analyses of materials that would prove prohibitively challenging to study otherwise, such as polycrystalline samples. The system is able to combine direct imaging with

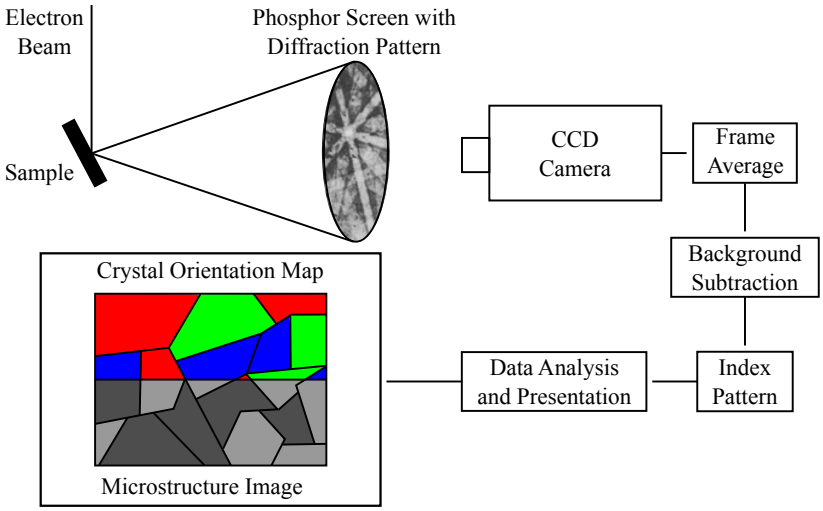

Figure 2.21: Experimental setup of EBSD as contained within an SEM in scanning indexing operation.

diffraction in real time. The key feature is the ability to select small areas on the sample surface to take diffraction patterns, such as single grains, phases or regions of chemical difference. The drawbacks or limitations of the technique are related to sample preparation for TEM. Only very thin samples are able to be used, and preparation of a sample can be painstaking and difficult. Often techniques such as focused ion milling are required to reduce the size of a sample to that required by the technique.

SAED in TEM utilizes the appearance of the diffracted beams on the back focal plane of the microscope. In imaging mode the electrons that are transmitted through the sample are all recombined and refocussed to provide the image, but in SAED the electrons are not recombined in the same way and the diffraction pattern at the back focal plane is maintained to the detector (Figure 2.22). This is achieved through the use of the intermediate lenses.

SAED patterns will contain diffraction spots as well as Kikuchi lines and can provide a multitude of information. The tilt of the sample relative to the beam will cause a significant change to the beam and must be well known before indexing of the pattern can take place. This can be calibrated using the Kikuchi lines. Polycrystalline or multiphase samples will generate rings of intensity in the diffraction pattern in much the same way as x-ray powder diffraction, as the 'spots' are present in all orientations leading to a circular pattern.

2.5 Synchrotron Techniques

Diamond Light Source is the UK's national synchrotron facility, Beamline I06 is the nanoscience endstation within the surfaces and interfaces 'village'. The

beamline utilises high photon flux soft x-rays for use with a photoemission electron microscope (PEEM) to provide both microscopic and spectroscopic facilities [82]. By utilizing the various apertures, lenses and imaging modes the microscope can provide chemical information through x-ray absorption and x-ray photoemission spectroscopy, with microscopy then possible using the electrons only from a single transition or element. The microscope is also combined with a high stability electron gun allowing use as an low energy electron microscope (LEEM), plus allowing imaging based on specific diffraction spots.

The system allowed the spectroscopic, microscopic and diffraction analyses of individual grains in the polycrystalline ZnPd sample. Polygrain samples provide challenges towards traditional UHV methods, but the ability to isolate grains for study in direct comparison to neighbouring grains, is hugely powerful.

The ZnPd sample was also taken to Brookhaven National Laboratory (BNL) in the USA for investigation using PEEM/LEEM. Most of the diffraction data was taken at BNL while the chemical studies were performed at Diamond.

2.5.1 Photoemission Electron Microscopy (PEEM)

In PEEM photons impinging on the surface produces photoelectrons which are guided through electron optics to enable spatially resolved spectroscopy and topography. The local variations in electron emission create image contrast at once across the whole area being illuminated. As such there is no need for rastering of a beam. This is beneficial for the study of dynamical processes. This operates in

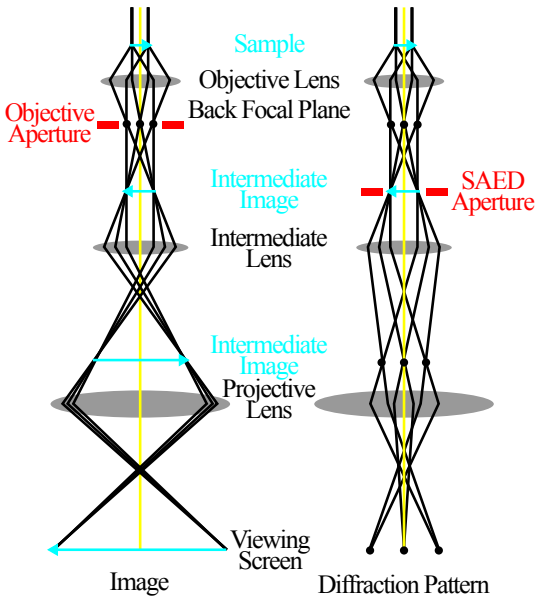

Figure 2.22: Difference between paths of electrons in imaging and diffraction mode in a TEM.

much the same way an SEM would do except with the use of photons as a probe.

The generation of core excitations and the emission of photoelectrons allows for a cross-over from microscopy to XPS. Using the lenses as an energy filter allows a small range of emitted kinetic energies to be obtained, in the form of a line on the CCD detector at the end of the imaging column. The line has varying brightness and a line scan provides an intensity spectrum similar to that in XPS, although wide scans were not possible. By correcting each scan for energy per pixel and correcting for the work function from the Fermi edge for each photon energy used, the data can be used to study core level shifts and other changes such as alterations of line shape or extra species.

2.5.2 Low Energy Electron Microscopy (LEEM)

LEEM operates in the same manner to PEEM although the use of electrons as both source of illumination and extracted species require the use of a beam separator in the microscope (Figure 2.23). This separates incident and emitted or reflected electrons from each other. The LEEM can be used to scatter the electrons from the surface region of the sample or in Mirror Electron Microscope (MEM) mode.

In standard LEEM mode the high energy electrons (~20keV) are accelerated toward the sample which is held at a similar bias to the gun through an objective lens held at ground potential. The electrons therefore slow down and become more surface sensitive. The depth of interaction of these electrons can be tuned by altering the sample bias. The elastically scattered electrons then leave the sample and after passing through the objective lens are re-accelerated to the gun potential. They are then separated from the incident electrons though a magnetic electron prism. By insertion of different apertures it is possible to change the field

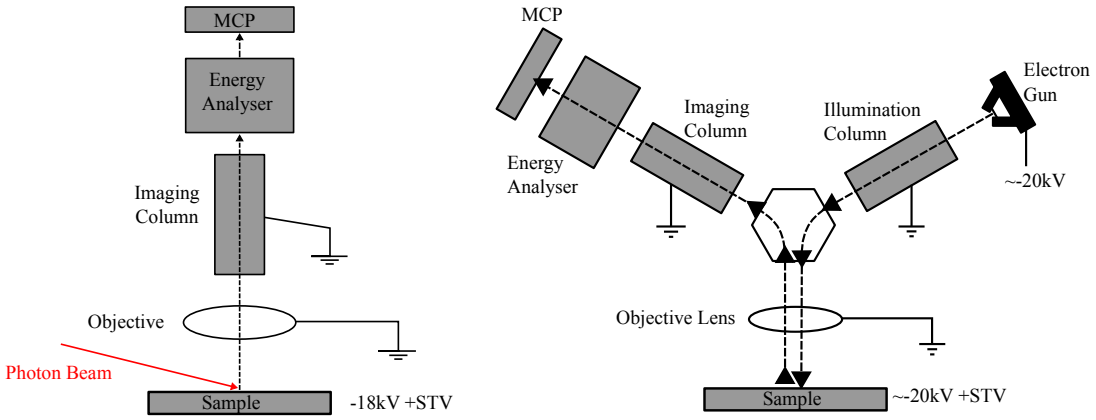

Figure 2.23: Schematic of a PEEM/LEEM (left and right respectively) experimental system.

of view of the microscope, to image the backscattered electron diffraction pattern or to generate the surface image using one of the non-specular electron beams. This creates the ability for diffraction contrast of the surface region.

Micro-spot LEED or micro-diffraction is a key advantage of the LEEM technique. While sharing the ability to display localized LEED patterns with TEM, in LEEM the diffraction comes solely from the surface region and is more analogous to traditional LEED. Interestingly in this mode, the diffraction spots do not change position with increasing incident electron energy. This is due to all emitted electrons being re-accelerated to the gun potential following the objective lens. Therefore the positions stay fixed although the changes in intensity still occur. Diamond Light source was used to prepare preliminary LEED patterns. Further work and the diffraction images shown in this thesis in Section 3.3.4 were recorded using an Elmitec V PEEM/LEEM in the Centre for Functional Materials at Brookhaven National Laboratory.

The diffraction images were analysed by comparison to a pattern taken at the same settings of a Si (111) 7×7 surface. By calibrating the diffraction window to the Si pattern, lattice constants were calculated as a proportion of the d-spacing in Si (111) 7×7.

In MEM mode the sample is held at a greater negative bias than the electron gun so as to reflect the incident electrons. By tuning the sample bias it is possible to allow the electrons to get close enough to the surface without direct interaction with the surface. In this mode the electrons are affected by the near surface region. As such the reflected intensity is representative of local changes in both topology and work function. In this mode the microscope can be made to image in work-function contrast mode, although this is highly influenced by any variation from normal between surface and incident electrons.

Chapter 3

Characteristics of the Surface Structure of an Intermetallic Compound Catalyst - ZnPd

3.1 Introduction

In the pursuit of a knowledge-based approach to catalysis the properties of ZnPd intermetallic compounds are being thoroughly investigated. Currently there have been many studies on surface-alloyed ZnPd produced *in-situ* through deposition and annealing. There is little published information about the surface properties of bulk ZnPd IMCs and there have been no reported UHV studies on single crystal samples. In order to provide greater understanding of the role of the bulk crystal surface in catalytic measurements it was attempted to characterize the clean surface of a bulk crystal. To conduct these experiments a detailed and careful preparation procedure of ZnPd is needed to produce a chemically clean and atomically ordered surface. The work in this chapter describes an examination of the surface structure of bulk IMCs, using scanning tunnelling microscopy (STM), x-ray photoelectron spectroscopy (XPS) and low energy electron microscopy (LEEM). This has been supplemented with additional work using photoemission electron microscopy (PEEM), electron backscattered diffraction (EBSD) and optical microscopy. While the study as presented here is experimental, the chapter contains calculated models and structures using density functional theory (DFT) techniques. The DFT work was performed by Dr. A Al-Mahboob and is included to complement the experimental results.

Single phase polycrystalline ZnPd was polished mechanically with diamond paste and cleaned ultrasonically in methanol before being placed in UHV (base pressure 10^{-10} mbar). The sample was cleaned through cycles of ion bombardment

and annealing. XPS was utilized to monitor the level of contamination of the surface. ZnPd is particularly susceptible to carbon contamination and so removal of carbon was a key requirement for cleanliness. Once a chemically clean surface was obtained, the process was then optimized in an attempt to produce atomically flat terraces and atomic order at the surface. It was hoped that a clear preference of surface termination or terminations would be apparent to aid the manufacture of these catalysts.

This work was performed as part of the Network for Intermetallic Compounds as Catalysts for Steam Reforming of Methanol, an action of the European Co-operation in Science and Technology (E-COST) research framework. Experimental work was performed at The University of Liverpool (UK), Institut Jean Lamour (Nancy, France), Diamond Light Source (Harwell, UK) and Brookhaven National Laboratory (New York, USA).

3.2 Literature Review

ZnPd is an intermetallic compound consisting of the two *d*-block transition metals Zn and Pd. Intermetallic compounds are discussed in detail in section 1.2.5. Pd has a face centered cubic structure and Zn has a hexagonal close packed structure [83, 84]. ZnPd was first found to be of interest for catalyzing the steam reforming of methanol by Iwasa *et al.* after investigating the effect of supporting a Pd catalyst on a Zn-Oxide support [22, 85]. The pure Pd catalyst exhibited nearly 100% selectivity for carbon monoxide but the Pd supported on Zn oxide showed selectivity similar to copper based catalysts, nearly 95% selectivity to carbon dioxide. This has led to investigations into what component of the system was responsible for the improved carbon dioxide selectivity, focusing on whether it was the Zn which was responsible or the formation of an alloy between Pd and Zn. It became apparent that the combination of ZnPd with the ZnO support combines to provide the highest selectivity, suggesting the ZnPd can be a replacement for Cu when supported on ZnO. This was found to be the case [86], and so in this section I will discuss the properties and capabilities of the IMC.

3.2.1 Bulk Structure

ZnPd IMC has a body-centered tetragonal structure with lattice parameters of a=2.8931 Å and c=3.3426 Å [19]. This can be seen below in Figure 3.1.

This structure is of the CuTi type with a space group of P4/mmm and a Pearson symbol of tP2. It has been suggested that ZnPd is also capable of forming a cubic lattice but this has yet to be conclusively confirmed by experiment

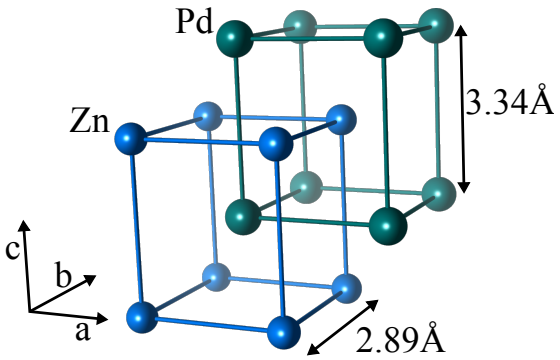

Figure 3.1: Bulk structure of the ZnPd intermetallic compound, illustrating the interlocking tetragonal structures of Zn and Pd. The body centred tetragonal structure can be perceived by considering the atoms bound by the blue Zn atoms and bonds. (Zn-Pd bonds not drawn for clarity)

[87]. Friedrich *et al.* found that all attempts to produce single phase cubic structures resulted in tetragonal structures. They used several methods to modify the tetragonal structure to cubic that involved heating in closed quartz ampoules, lengthy annealing processes and rapid quenching. At no point were they able to create the cubic modification. Theoretical calculations provided a minimum c/a ratio of 1.15, quite distant from the cubic structure. The tetragonal distortion was attributed to Pd-Pd interactions within the (0 0 1) plane of the lattice. Most interest, as judged through the literature, has been focused on the largest solid phase containing between 40% and 60% Zn [19, 45].

When describing the structure of ZnPd it is possible to use either the body centered tetragonal (BCT) structure with Zn atoms at the corners of the unit cell or the face centered tetragonal structure (FCT) with Pd atoms at the corners of the unit cell. This thesis will consistently use the BCT notation to describe the surfaces studies. In consideration of other studies which may have used the FCT unit cell a conversion table is shown in Table 3.1.

Surface	
BCT	FCT
(0 0 1)	(0 0 1)
(1 0 1)	(1 1 1)
(1 1 0)	(1 0 0)
(1 1 1)	(2 0 1)
(1 1 4)	(1 0 2)

Table 3.1: Selection of Miller indices for ZnPd surfaces and their conversion from BCT to FCT unit cell notation.

3.2.2 Surface Properties and Growth

Most samples of the IMC used for model UHV studies have been grown as a surface alloy in the form of a Zn layer on a defined Pd surface, often the (1 1 1) surface. The Pd surface leads to almost 100% selectivity for methanol decomposition. It was only when the metal is combined with Zn that the favourable results were achieved. An initial question however, which was addressed through studies of the surface, was whether the superior CO_2 selectivity was actually caused by the alloying of Zn and Pd. There are two models which were proposed to describe the formation of a catalytic surface. Firstly there was a model which suggests that the Zn forms an overlayer, and another which suggests surface alloy formation. The first model in which the reactivity is caused by a Zn over-layer was proposed by Gabasch *et al.* [14], in which Zn was deposited onto a Pd(1 1 1) sample. Using LEED they determined that 0.75 monolayers (ML) of Zn produced a p(2 × 2) LEED pattern. Increasing the coverage to >3 ML at 750 K caused the formation of an ordered surface alloy, which displayed a LEED pattern comparable to the bulk ZnPd (1 0 0) surface. The sample was annealed to ever higher temperatures once deposition had taken place and the surface composition was analysed to help interpret Zn behaviour at the surface. A summary can be seen in Figure 3.2.

Initially the surface is covered with up to 3 ML of Zn, and upon heating the Zn desorbs from the surface until the monolayer remains. This is deemed to be the reactive form of the surface alloy. Under continuous heating the Zn begins to diffuse into the substrate. This is not an ordered surface alloy. This diffusion continues until the remaining surface Zn is desorbed at the higher temperatures. Bayer *et al.* provide the other model for alloy formation [88]. They created a similar sample to Gabasch *et al.* and the two experiments can be considered analogous. Studies were performed using XPS and LEED. This experiment observed the formation of the p(2 × 1) superstructure atop the Pd between 450

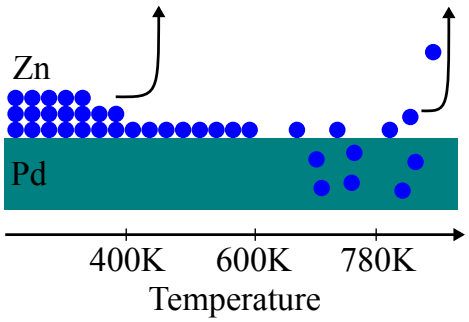

Figure 3.2: Growth modes of Zn on Pd(111) described by Gabasch *et al.* while growing the surface intermetallic compound ZnPd. (Figure adapted from [14]).

and 600 K, while also containing a 1:1 Pd:Zn ratio. Bayer *et al.* interpreted their data to describe the formation of an ordered surface alloy stable upto 600 K after annealing the Zn covered Pd sample above 310 K. Above 600 K the Zn begins to diffuse into the bulk, although no desorption of Zn was observed until above 800 K. Stadlmayr *et al.* also observed this evolution of the system and their interpretations were in agreement with the other groups [20].

The two models are very similar, the only difference being in the middle of the temperature scale, where either an ordered surface alloy is formed or a 1:1 surface adlayer is formed. Most studies on the surface structure of the Zn deposited on Pd system agree with the conclusions reached by Bayer et al. whilst there is little agreement with the growth system proposed by Gabasch et al. [16, 85, 89–91]

Relatively few studies have been performed in which Pd has been deposited on Zn. In one study the Pd was deposited on polycrystalline Zn oxide and studied with XPS and X-Ray-Excited Auger Electron Spectroscopy (XAES) [92]. It was found that the Pd grows on the surface in a layer by layer mechanism with some island formation. In all cases, although there were some differences in growth mechanism, the same electronic properties were achieved. As all the experiments in this study were performed at 300 K, within the Bayer 'multilayer' region of IMC formation, it can be assumed that the same alloy is forming when Pd is deposited on Zn.

The surface of the surface alloys has been characterised as being a corrugated surface, with Zn atoms sitting 0.25 Å higher than the Pd in the Pd(1 1 1) substrate studies and the Pd sitting 0.06 Å higher on the Pd(1 1 0) substrate [20, 93]. On the Pd(1 1 1) surface, which has been most heavily studied, the surface consists of alternating Zn and Pd atomic rows, in a 3 domain p(2 x 1) structure [89]. This surface alloy, when formed through deposition, is often only several atomic layers thick. The Pd-Zn bond is stronger than both the Pd-Pd bond and the Zn-Zn bond, which draws surface Zn atoms into the subsurface layer and also creates the ordered, perturbed rows on the surface[94]. The Zn preferentially adsorbs in sites with a maximum number of neighbouring Pd atoms, either the bridge site with two Pd atoms or the hexagonal close packed site are the most stable [95]. This structure is highly sensitive to the proportions of Zn at the surface [96]. Between 1 and 3ML a 1:1 alloy is formed, and at lower coverage small ZnPd islands form, which in the context of SRM would be highly undesirable. A summary of the surface alloy studies is included in Table 3.2.

System	Method	Information	Reference
Pd/Zn(0 0 1)	UPS	Valence Band	[97]
Pd, Zn/Ru(0 0 1)	XPS, TDS	stability, valence band, CO adsorption	[98]
Zn/Pd(1 1 1)	XPS, LEED, UPS	growth mode, structure, stability valence band	[88]
Zn/Pd(1 1 1)	TPD, LEED	Structure and stability	[14]
Zn/Pd(1 1 1)	LEED, HREELS, TPD	Structure, CO adsorption	[85]
Zn/Pd(1 1 1)	LEED	Structure, H_2 and CO adsorption	[91]
Zn on sulphur covered Pd(1 1 1)	AES, TPD	Sticking Coefficient	[99]
Zn/Pd(1 1 1)	STM, LEED, DFT	Growth mode, structure and stability	[100]
Zn/Pd(1 1 1)	LEIS	Growth mode, structure, stability and valence band	[20]
Zn/Pd(1 1 1)	XPS, LEIS, PM-IRAS	Growth mode, structure, steam reforming	[101]
Zn/Pd foil	LEIS, AES	Composition and stability	[89]
Zn/Pd(1 1 1)	DFT, STM	Growth mode, structure and stability	[95]
Zn/Pd(1 1 1)	Monte Carlo	Growth mode	[96]
Zn/Pd(1 1 0)	LEIS-ICISS, LEED, AES, TPD	Growth mode, structure and stability	[93]
diethyl zinc/Pd(1 0 0)	UPS, AES, TDS	Growth and reactivity	[102]

Table 3.2: Summary of experimental and theoretical studies on the ZnPd surface alloys.

3.2.3 Electronic Properties

The catalyst Cu/ZnO is the starting point for all SRM catalyst comparison. This is the catalyst which provides the necessary selectivity benchmark which ZnPd needs to be comparable to but with improved stability. Bayer *et al.* observed that the average electronic structure of ZnPd is the same as that of Cu/ZnO [88]. With Pd having a $4d^{10}$ structure and Zn containing a $3d^{10}4s^2$ structure, the two combine to form a $d^{10}s^1$ configuration. The density of states of ZnPd around the Fermi level once alloying has taken place begins to resemble that of the Cu catalyst [95]. This change in electronic properties occurs during the change to the surface alloy 'multilayer', and through XPS it was shown that the binding energies of the Zn $2p_{3/2}$ and the Pd $3d_{5/2}$ orbitals were altered. This is due, in part, to the charge transfer from Pd($4d$)→ Zn($4p$) and the rehybridization Pd($4d$)→ Pd($5s$,$5p$)[98]. The shift in binding energies is important as the larger the shift in the binding energies during alloying the lower the desorption temperature of CO during SRM [19]. The conclusions reached by Nozawa *et al.* show that SRM CO_2 selectivity can be correlated to the d-band energy. Zn reduces the CO chemisorption ability of Pd through a weakening of the Pd($4d$)-CO-(2π) bonding. ZnPd surfaces with a high concentration of Zn show Pd-CO bonds 12-16 kcal/mol weaker than on a metallic Pd surface, which can improve resistance to poisoning effects [98].

The IMC also displays lower density of states near the Fermi level compared to Pd, and this is important as CO selectivity is believed to be directly related to the density of states around the Fermi level [45]. ZnPd was found to be more catalytically selective than the isostructural ZnNi and ZnPt [50]. It was the only one of these materials to have a DOS that closely matched Cu, leading to the conclusions regarding selectivity and band structure near the Fermi level. Equally the Zn:Pd ratio at the surface and subsurface is a key determinant in the electronic properties, as long range effects from subsurface layers control the electronic structure and hence influence catalytic properties of the IMC [16, 103].

3.2.4 Chemical Properties

When considering the chemical properties of ZnPd in SRM, one of the main concerns is the behaviour regarding CO in reaction situations in comparison to that of elemental Pd. This is because the adsorption of CO onto the ZnPd catalyst surface will begin to deactivate the catalyst and damage the CO_2 selectivity of the reaction [104]. A deactivated ZnPd catalyst can be repaired by breaking the constituents up through oxidation to PdO and ZnO. These constituents are then recombined back into nanoparticles of ZnPd through reduction at 250 ^{o}C [105]. This, however, would be undesirable within mobile applications as this would

require significant overhaul with also unknown damage being done to the fuel cell before servicing could take place.

Carbon monoxide will readily adsorb onto elemental Pd, although CO does not react so easily with elemental Zn. Jeroro and Vohs found that CO molecules adsorbed at three-fold hollow sites on the Pd(1 1 1) surface will desorb at 460 K, whereas at the same position on the ZnPd surface (which resembles the Pd(1 1 1)), the molecule will desorb at 440 K [103]. The carbon monoxide only reacts weakly with the Zn within the surface and does not adsorb on sites which contain Zn. It is the long range effects of the Zn on the Pd that cause the change in CO adsorption. This ligand effect is where the charge transfer between the atoms causes a change in the reactivity of the Pd. There is further evidence that the subsurface Zn atoms are the largest creator of this ligand effect. At the surface the ligand effect is reduced by the strain effect, whereas in the subsurface the Zn is not affected by the strain effect and can contribute fully to the ligand effect [21].

The other important chemical property to investigate in this situation is the mechanism or pathway of the reaction on the ZnPd surface. As increased knowledge of this pathway can improve catalyst design and reaction optimization. On the ZnPd surface alloy methanol is converted to formaldehyde through reaction between the oxygen and alloy. Formaldehyde (CH_2O) is seen as the key intermediate to achieving high CO_2 selectivity, but only up to temperatures of roughly 573 K [16]. Above 573 K the CH_2O is dehydrogenated to form CO. This is due to the break-down of the surface alloy as Zn diffuses into the bulk and the 'multilayer' is replaced with the 'monolayer'. Under these conditions water is not activated and CH_2 is not able to become formic acid. In bulk ZnPd IMCs it was found that increasing the temperature leads to increasing disorder at the surface, which may disrupt the electronic effects throughout the system and reduce the CO_2 selectivity [91]. As can be seen in Figure 3.3, formaldehyde is converted back to methanol but bonded through the oxygen atom as a ligand. This is then dehydrogenated to formic acid and then decomposes to CO_2 and H_2.

The temperature of 573 K is therefore important for selectivity and this can be considered a 'Thermal/Thermo-chemical stability line' for SRM (CO_2) selectivity [101].

3.2.5 Performance in Steam Reforming of Methanol

The key performance indicator for ZnPd in methanol steam reforming is the selectivity towards producing CO_2 in the reaction through steam reforming rather than CO through decomposition. Most results demonstrate a best CO_2 selec-

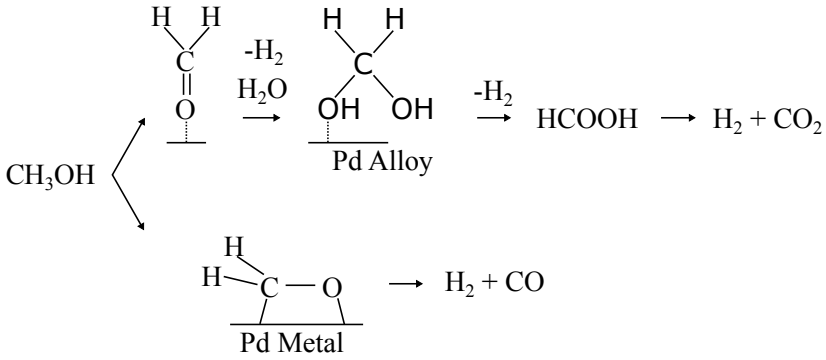

Figure 3.3: Diagram of the reaction route for methanol steam reforming over Pd alloys and metallic Pd (Figure adapted from [106]).

tivity of 99.5% as achieved in the work of Friedrich *et al.* [45]. This highest selectivity was achieved with a compound with a 48.4:51.6 Zn:Pd ratio and a reaction temperature between 350 and 400 ºC. The work of Isawa *et al.* also found that catalytic performance and selectivity is greatly improved by reducing the catalyst at higher temperatures before use in catalysis [22]. It would be useful if this general trend could be extended beyond individual work, but the reality is that experimental results may oversimplify the relationships between catalyst and selectivity. The selectivity of the catalyst is dependent on a number of things involving any one of synthesis parameters, oxidative and reductive gas treatments, annealing and reaction conditions. This causes the recreation of any correlation from laboratory work on an industrial scale to be extremely difficult, which leads to uncertainty as to why similarly treated catalysts can possess very different selectivities [16]. The advent of high precision, ambient pressure XPS may reduce this uncertainty in the near future.

3.3 Results

3.3.1 *Ex-Situ* Preparation

In order to understand the fundamental properties of the intermetallic compound surface, the first requirement was to produce a chemically clean and atomically/microscopically flat surface. Previous work by other groups had focused on a preparation technique of high temperature annealing during oxidation in an O_2 environment and reduction in an H_2 environment [107]. While this technique was shown to provide a chemically clean intermetallic surface, it was not expected to provide a flat surface, as oxidation and reduction can be destructive to flat terraced surfaces.

A polycrystalline bulk ZnPd intermetallic sample was produced through spark

plasma sintering. This involved the combination of pure Zn and Pd powders in an Ar atmosphere, after which high pressure and large currents were passed through the powder mixture until the polycrystal was formed. The resulting ingot was then annealed at high temperature in an attempt to increase grain size. For further reading on the spark plasma sintering process see the review paper by Munir *et al.* [108].

It was decided to adopt the familiar UHV preparation route as described in section 2.1.2, but to optimize the process for the ZnPd crystal. The crystal was polished using successively finer grades of diamond paste (6 μm, 1 μm and 0.25 μm), before being cleaned ultrasonically in methanol. The sample was then mounted on a sample plate using tantalum wires before being inserted into UHV, base pressure 10^{-11} mbar. The sample can be seen in Figure 3.4b. Figure 3.4a shows an EBSD map overlaying the corresponding SEM image of the surface of the ZnPd sample. This is complemented by a polarized light optical microscope image in Figure 3.4c. These micrographs demonstrate the spread of grain sizes in the sample with a range of approximately 5 - 20 μm. The EBSD map also shows very little indication of an overwhelmingly preferred surface termination. It should be noted that large tilt angles between grains would have made analyses by this method highly unreliable. For this reason surface terminations relating to each colour have been omitted. The map is therefore presented to qualitatively demonstrate the range of terminations and/or grain angles (relative to beam

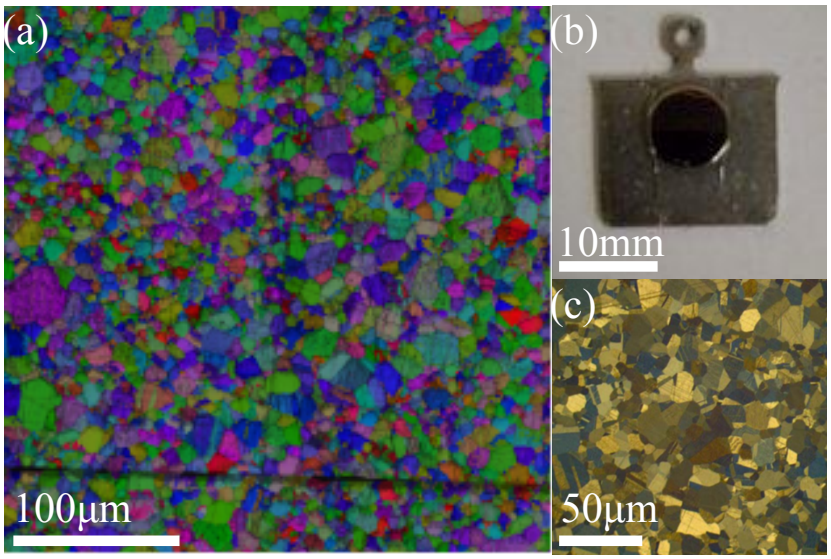

Figure 3.4: (a) EBSD map of ZnPd surface overlain on SEM image of the same area. The map demonstrates a large range of present surface orientations without any clear preferences visible with this technique. (b) Optical image of ZnPd sample made by spark plasma sintering secured to a sample plate. (c) Polarized optical microscope image of ZnPd surface.

normal).

Polycrystalline samples are not well suited to surface science techniques due to the inherit complexities and unknowns when moving from the macroscopic to the microscopic scale. Spectroscopic techniques used in the laboratory have a sample size of several mm, far larger than the grains in this sample, so while this can provide information regarding the chemical environment of the entire surface, any deviations or special conditions related to surface termination are lost in the integrating process. Similarly, diffraction techniques such as LEED provide too large a beam to limit the number of grains creating the pattern. Even if this were possible, it is not possible to 'aim' the beam at one isolated grain if they are smaller than a few mm or poorly distinguishable. STM is capable, in many respects, of treating each grain as an individual, isolated single crystal. However, scan ranges are not possible over a suitable large region to fully target grains with any certainty, reducing the possibility of a truly systematic study. Techniques such as PEEM and LEEM are designed to provide small beam spots combined with the real time microscopic ability to aim the beam. This in theory provides all that is needed to individually study each crystallite.

A significant difficulty that arises in the specialized techniques and even in the standard laboratory facilities is tilt. Even thorough polishing and grinding of the crystal leaves grains that are differently orientated relative to one another, sometimes drastically. In diffraction or particularly surface sensitive spectroscopic techniques, this causes large problems. Diffraction can be subject to dramatic misalignment to the point where the completely backscattered specular beam cannot be visualized in the back projection screen, or astigmatism causes skewing and stretching of patterns. In spectroscopy the angle of incidence determines the path length of the electron through the material and has a strong influence on the resulting spectrum, particularly in very surface sensitive scans with low incidence energy probes. Experimental systems are capable of correcting for tilt mismatches between incidence and surface perpendicular. Often the built in correcting mechanisms can correct up to around 2° - 3°. In practice with this sample it was rare that this was enough. As a result, many of the diffraction patterns are significantly distorted reducing the amount of usable data.

3.3.2 Development of Sample Preparation Using XPS

The sample was initially placed in UHV to undertake spectroscopic studies using XPS. Results were taken from the sample, as entered into the chamber, after sputtering, degassing to 180 °C and following the 5 sputter-anneal cycles (Figure 3.5). An initial sputtering time of 85 minutes was used to overcome the long period

Element/ Transition	Element	IMC	Air Exposed Surface	Sputtered Surface	Prepared Sample
Pd $3d$	335.0 eV [109]	336.2 eV [45]	335.7 eV	335.0 eV	335.9 eV
Zn $2p$	1021.8 eV [110]	-	-	1020.8 eV	1021.3 eV
Zn LMM	992.1 eV [111]	992.0 eV [45]	992.5 eV	993.2 eV	992.7 eV
Zn $3d$	10.0 eV [112]	9.2-9.6 eV [45]	9.24 eV	9.0 eV	9.3 eV

Table 3.3: Comparison of observed binding energies for core levels and kinetic energies for Auger peaks from XPS data. The surface undergoes changes following sputtering which are as yet not understood. The peak positions after several cycles are representative of the clean intermetallic compound. Uncertainties estimated at 0.1 - 0.2 eV.

of time the crystal had been at air, and the lengthy polishing procedure. Several sputter-anneal cycles were used to maximize the probability of a clean surface. Temperatures were measured using a K-type thermocouple on the manipulator heating stage.

Concerns regarding the high vapour pressure of Zn in UHV led to the practice of positioning the sample directly in front, and within 30 mm of the mass spectrometer located in the preparation chamber. It was then possible to detect any evaporated Zn from the sample, which was observed at 780 K [14] for the surface alloy. During the annealing processes in this work, no Zn was observed in the mass spectrometer spectra, which verifies the stability of surface Zn below 780 K.

Peak positions and areas were calculated using a Shirley background and a mixture of Gaussian-Lorentzian convoluted lineshapes and Doniach-Sunjic lineshapes for asymmetrical peaks. Both Zn and Pd core levels display the expected characteristics for the intermetallic compound as described in the literature [45]. The key amongst these are characteristic binding energy shifts and modifications of the line profiles. A summary of these changes is shown in Table 3.3. It can be seen that following the UHV cleaning process elemental Pd is encouraged to bond with the bulk and form the intermetallic compound. What is less clear is the behaviour of Zn during this process. While there is confidence that following the cleaning process, the IMC is satisfactorily prepared, the status of the sputtered crystal is unclear. The only Zn species that would conform to the observed $3d$ band would be either ZnS or ZnSe. There is no evidence of either S or Se. Therefore it is unclear as to the reasons for the observed shifts.

Following entry into the system, the unprepared sample is heavily coated in both O and C. What is somewhat unusual is absence of an oxide compound, especially ZnO. The Zn 3d core level for ZnO would be expected at 10.6 eV and this is not observed. What is seen suggests that the IMC remains under a layer

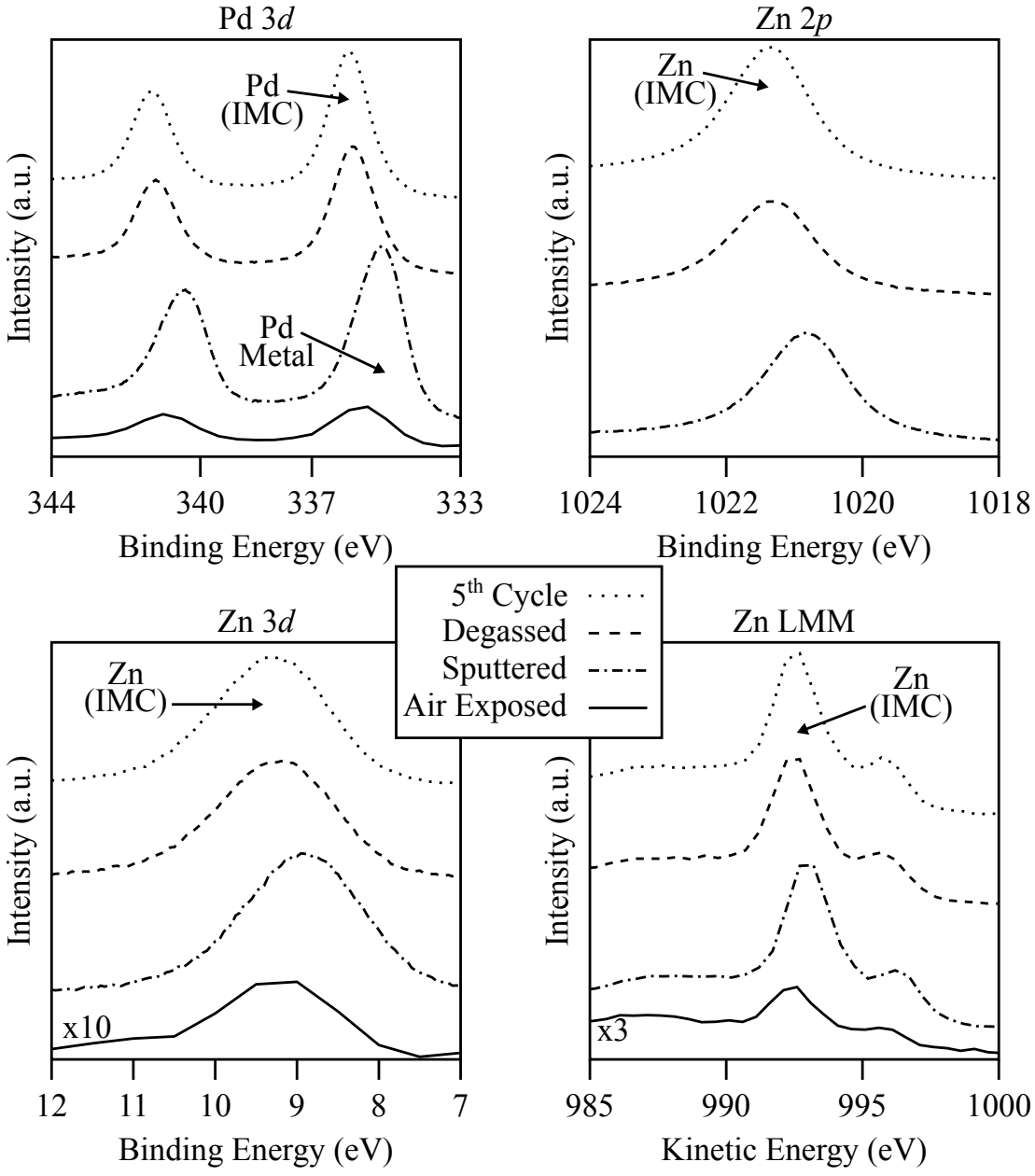

Figure 3.5: XPS spectra for Pd 3*d*, Zn 2*p*, Zn 3*d* and Zn LMM following preparation in UHV. Following several sputter-anneal cycles the surface displays the characteristic peak shapes and positions of the intermetallic compound.

of adventitious C and O.

After sputtering the surface presents some unexpected features. Evidence of Pd metal can be observed through the binding energy shift and adjusted symmetry of the Pd 3d core level. This would suggest that there is segregated elemental Pd and Zn on the surface which after preparation form the ZnPd IMC surface. Compositional analyses (Table 3.4) suggest a preferential sputtering of the Zn in the surface. The is a large difference between elemental Pd and Zn surface energies (1.92 Jm^{-2} and 0.99 Jm^{-2} respectively) [113]. This would be in agreement with evidence that elements of the smallest size and lower surface energy are particularly susceptible to preferential sputtering [114]. This possibility explains the Pd 3d modifications but is less convincing when considering the behaviour of the Zn core levels. The core level and Auger shifts do not conform to any accepted compound or elemental positions. It is suggested that sputtering may cause some extensive defect sites of crystal strain that is influencing this shift. These shifts can be seen in all peaks, including Auger peaks.

A subsequent study investigated the surface using XPS or UPS following air exposure and subsequent sputtering. The sample was measured following entry to vacuum, sputtering, two complete preparation cycles, as determined from the above processes and following sputtering of the prepared sample. The peaks are always shifted approximately 1 eV to lower binding energy following sputtering. The results of this experiment are shown in Figure 3.6. This confirms that the previous observations are consistent although the true nature of the surface modification is still unknown. This would form a key goal in further work on this system. Although there are questions which remain regarding the surface following sputtering the XPS analysis in this study was sufficient to confirm the presence of the IMC surface in agreement with previous studies in the literature.

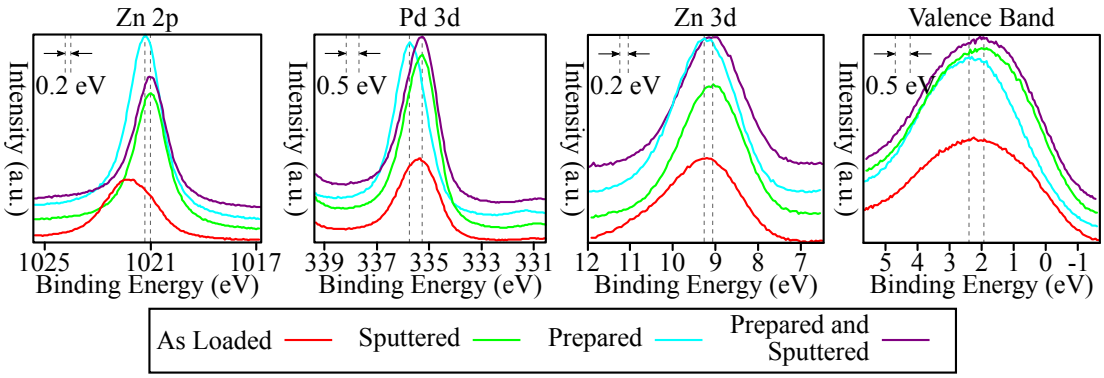

Figure 3.6: XPS spectra showing the effect of sputtering both on the air exposed surface and the clean prepared surface. The same shifts to higher binding energy of 0.2 eV in Zn species and 0.5 eV in Pd species are present after sputtering regardless of the initial condition of the surface.

Preparation State	Zn (at%)	Pd (at%)
Sputtered	38.6	61.4
Degassed	47.3	52.7
5^{th} Cycle	50.5	49.5

Table 3.4: Change in atomic concentration, as measured by XPS, of the surface of ZnPd following cleaning cycles. The uncertainty is estimated at 5 at% for all values.

Compositional information regarding the surface was gained using laboratory XPS. Although this is an integrating method and cannot provide information for individual grains the use of this method added to the confidence in IMC preparation. The results of this can be seen in Table 3.4. The XPS compositional analysis shows the effect of re-establishing bulk concentrations at the surface with the preparation conditions. All XPS analyses were performed as described in section 2.2.1.

Utilizing the PEEM capabilities of Beamline I06 at Diamond Light Source [82] (see section 2.5), it was also possible to compare the chemical environment of different grains. Grains were differentiated using LEEM in MEM mode, to form contrast using the work function. The comparison of key transitions are shown in Figure 3.7. It can be seen that at the experimental conditions of the equipment, very little distinction can be made between the grains. With the method used, it was not possible to obtain an accurate composition of the surfaces. Each scan is taken in isolation from the others. At the lower incident photon energies it was expected that there may be enough surface sensitivity to detect single element terminations. Only the (0 0 1) surface of the crystal would provide a Pd or Zn only terminated surface, and this was not observed. In practice the significant variation in tilt of grains with respect to the incident beam would have made this observation unlikely regardless of whether this termination existed or not.

3.3.3 STM Investigations

Following the cleaning treatments of sputtering and annealing the sample was allowed to cool then placed into an Omicron VT-STM. The surface was found to be very rough, and contained large regions of highly stepped terraces across the majority of the surface. One difficulty with this technique is that although macroscopically the crystal is perpendicular to the x and y planes of the tip, each individual grain can vary substantially from this. While large scale scans of the crystal were relatively fruitless, on occasion there were flat areas of the crystal which yielded atomic resolution. This was used to determine the structure present.

In areas where it was possible to find atomically flat terraces, these were limited to being no more than approximately 30 x 30 nm. Only a small subset of possible surfaces were observed, these were the (1 1 0), (1 0 1), (1 1 1) and (1 1 4) surfaces. A summary of the observed surfaces in STM is shown graphically in Figure 3.8. The most commonly observed surface structure was that of the (1 0 1) surface. Evidence of this surface can be seen in Figure 3.9. Comparison with the model and simulated STM images provides confirmation of the expected results for the (1 0 1) surface (Figure 3.10), which can be expected to be the highest density plane. The STM was operated in constant current mode with a positive bias between 0.8 - 1.2 V with a tunnelling current of 1 nA.

The surface can be seen to be in good agreement to the expected structure of the bulk terminated structure provided from experimental results by Freidrich; and Nozawa *et al.* [19, 45]. These results also agree with structural calculations performed by collaborators as part of this study. Full details are available in the work of Al-Mahboob *et al.* [115]. In the DFT calculations a bulk supercell of 6 or

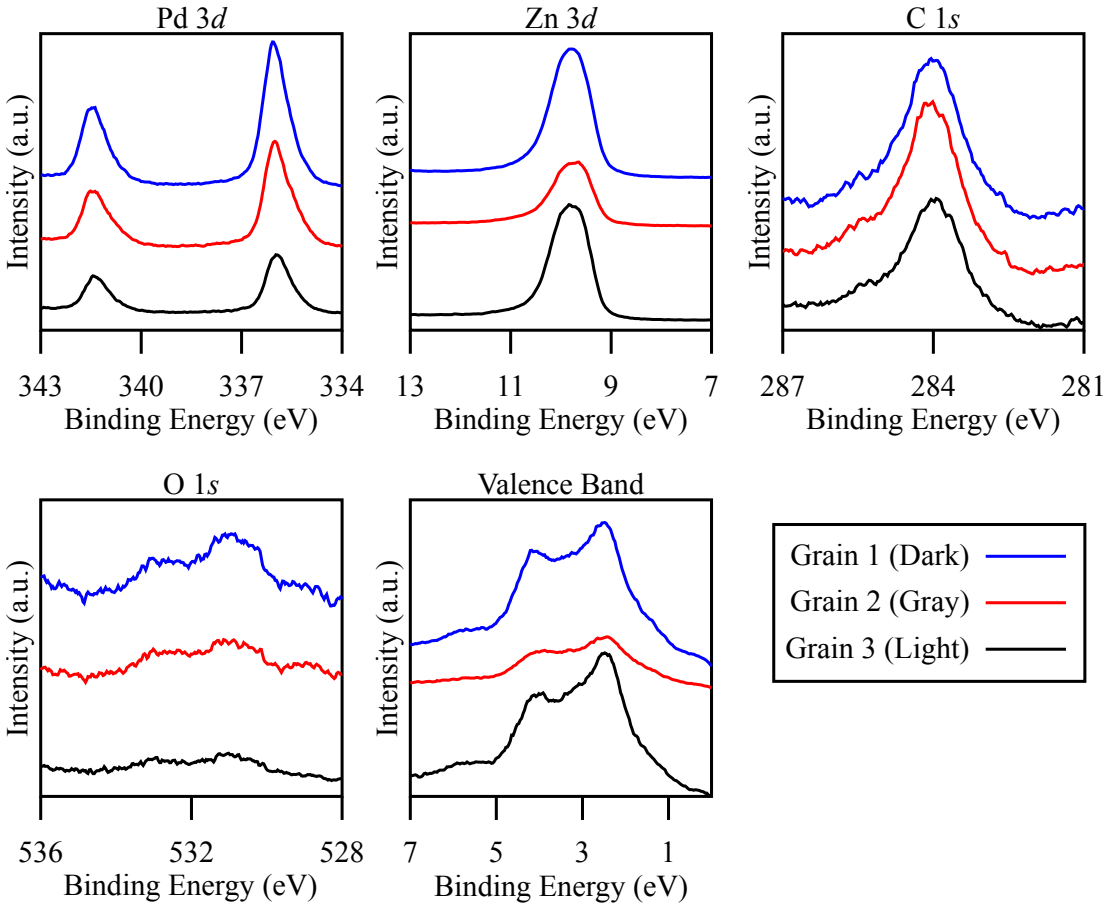

Figure 3.7: XPS grain comparison of bulk ZnPd sample using PEEM. Grains were labelled by their apparent colour using MEM mode in the LEEM. The colour difference is due to local variations in surface work function. The sample appears chemically uniform across the different grains on the crystal.

8 atomic layers was formed and optimized. The surface supercell was made from the bulk supercell and the surface atomic layers were relaxed for the primitive surface cell. An approximately 10 Å vacuum slab was used with an orbital cut-off of 4.5 Å. The STM simulations were then generated using CASTEP software integrating the electron density at a fixed height above the surface [116].

Importantly, it is necessary to recognize the lack of clear Zn atoms in the STM image. This was previously reported by Weirum *et al.* in their studies on surface alloys [100]. It is suggested that the large Pd $3d$ band near the Fermi level is so dominant at tunnelling conditions that Pd appears significantly brighter than any Zn atoms in the surface. This is not a condition that appears to depend on the tip-sample bias, as no obvious distinction was observed. It was much easier to obtain atomic resolution with positive bias, and most images that provided the possibility of atomic scale analysis were taken with positive bias.

The (1 1 1) surface of the crystal is much less prevalent than the (1 0 1) surface but is capable of forming large (relative to others in the crystal) terraces as can be seen in Figure 3.11. This surface can be compared to the model in similar fashion to the (1 1 1) surface as shown in Figure 3.12.

This surface demonstrates larger discrepancies from the model which is attributed to drift and/or creep in the STM image. This could be due to a particularly large tilt of this particular grain, or facet on the grain. The (1 1 1) surface is either Pd or Zn terminated, but the surface imaged is Pd terminated from comparison with simulated STM images. If the surface is Zn terminated, the Pd still plays a large role in the surface electron states and results in a very flat STM image, with little corrugation. The Pd terminated surface, however, has highly exaggerated corrugation as seen in the experimental data.

No other flat terraces large enough to analyze and displaying atomic resolution were found on the crystal. The surface of the crystallites are more likely to be constructed from highly stepped surfaces and vicinal planes. Some of these were

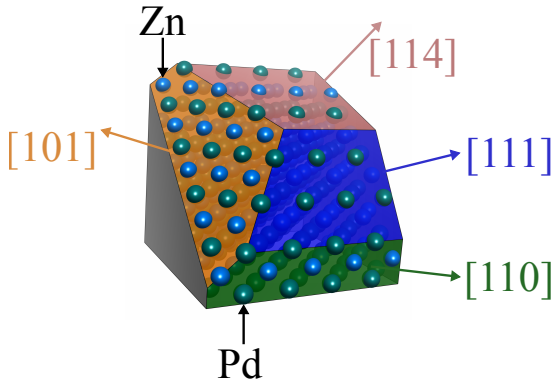

Figure 3.8: Graphical summary of all surfaces observed using STM on the ZnPd polycrystalline sample.

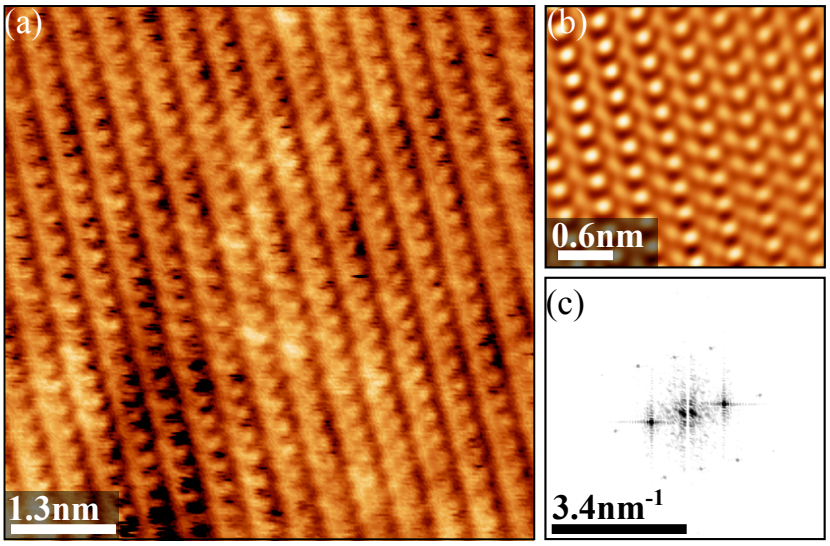

Figure 3.9: a) STM image (merged with FFT filtered image shown in (b)) showing the (1 0 1) surface of ZnPd. (c) FFT raw image from (a) used for the filtering.

imaged and have been compared to the bulk model. As can be seen from Figure 3.13, the surface which provides the resolution is the (1 1 4) plane of the crystal. By comparing this facet to the bulk model, the (1 1 0) surface can be distinguished. This then provides evidence of the three low index planes which were expected following calculations.

Ultimately, in the absence of single crystal samples to study, a large part of this study was to discover the most common surface structures in order to improve understanding of the surface most likely involved in the catalytic reaction. This

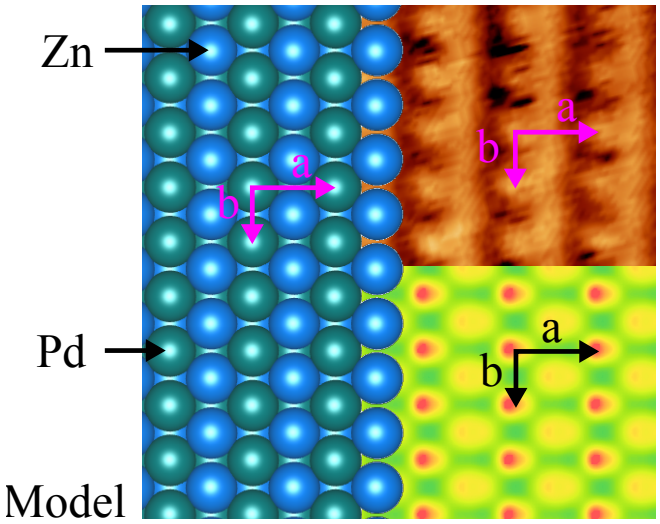

	STM	Model
a	4.2 Å	4.3 Å
b	2.7 Å	2.9 Å

Figure 3.10: Comparison of STM results to model structure and simulated STM data of ZnPd (1 0 1) surface. In both the experimental data and the simulation the clear spots can be observed as Pd atoms, while the striped patterns are related to the Zn atoms which are much less resolved.

has not been achieved due to the technical limitations in taking larger-scale, reliable assessments of multiple surface terminations. It has been possible to confirm the presence of the most promising candidates as predicted from surface calculations. The (1 0 1) and (1 1 0) surfaces of the crystal are calculated to have the lowest surface energy from DFT (Table 3.5) [115], and the Wulff plot of the crystal at the preparation temperatures suggests that the crystal should only demonstrate these two surfaces. The presence of the (1 1 4) surface is suspected to be related to the crystallites attempts to form the preferred (1 1 0) surface, leading to highly faceted and stepped surfaces.

An observation of this study was the imaging of the Pd terminated (1 1 1) surface. It is not possible to rule out the appearance of Zn terminated (1 1 1) elsewhere in the crystal as no resolution on them was possible. Terraces with the same symmetry can be seen but display no features unique to the (1 1 1) surface. Atomic terraces which terminate with angles relating to the three-fold symmetry of the plane appear frequently but without atomic resolution it is not possible to confirm the surface.

The calculations show that at the levels of heating used to anneal the crystal, the only favoured surface structures are (1 0 1) and (1 1 0). This was observed anecdotally during experiment as the crystal would only form imageable flat terraces following a small number of preparations. Too many cycles or too high a temperature and the surface would become extremely faceted and unsuitable for scanning. The optical microscope image in Figure 3.14 shows the surface following several sputter-anneal treatments and demonstrates the faceting of the surface.

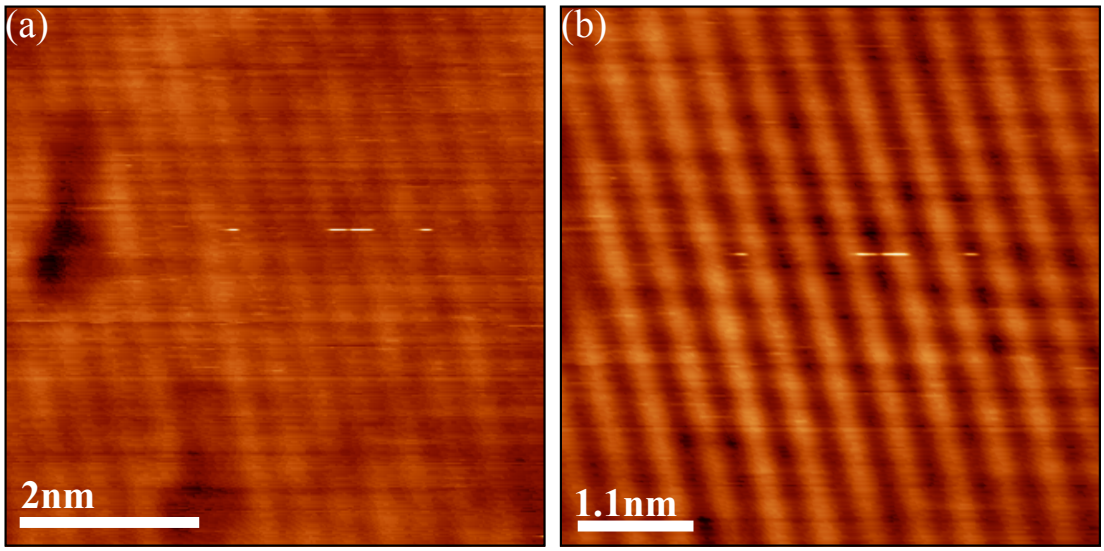

Figure 3.11: (a) STM image of clean (1 1 1) surface of ZnPd. (b) FFT filtered image of (1 1 1) surface of ZnPd. The use of FFT filtering allowed the appearance of discrete atoms as opposed to row structures.

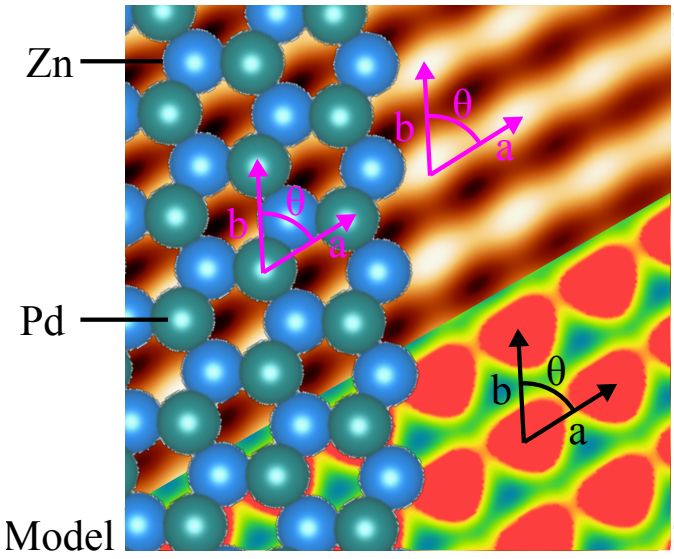

	STM	Model
a	4.3 Å	4.1 Å
b	4.6 Å	4.4 Å
θ	63.0°	62.4°

Figure 3.12: Comparison of STM results to model structure and simulated STM data of ZnPd(1 1 1) surface. The STM data shows good agreement with both the model and the simulated STM data. The finer detail of the STM simulation is not apparent however.

The lines across each grain were initially mistaken for polishing grooves. Grooves from surface modification and polishing can be distinguished by the differences in direction and uniformity. The polishing grooves are randomly spaced, randomly orientated and cross multiple grains whereas the faceting is uniform and does not cross grain boundaries. After a 12 hour anneal, to further understand this issue, the faceting and roughening of the crystal was such that it was no longer mirror shiny and appeared rough to the naked eye. This is expected from the Wulff plots generated using DFT [115].

3.3.4 LEEM and μLEED

LEEM allows the ability, among others things, to form diffraction patterns from small areas on a crystal making it ideal for use with a polycrystalline sample. An initial LEEM map was taken using the LEEM in MEM mode, to create a work function based contrast. The contrast in these images however is highly sensitive to tilt. The observed differences must be considered with this in mind.

Surface	(1 0 1)	(1 1 0)	(1 1 4)	(1 1 1)
DFT Surface Energy (eV Å^{-2})	0.0662	0.0697	0.0832	0.0802

Table 3.5: DFT Surface energy comparison for ZnPd surface terminations observed in STM. These surfaces displayed particularly lower surface energy than the others generated, which indicates it was not surprising that these surfaces were most readily viewed.

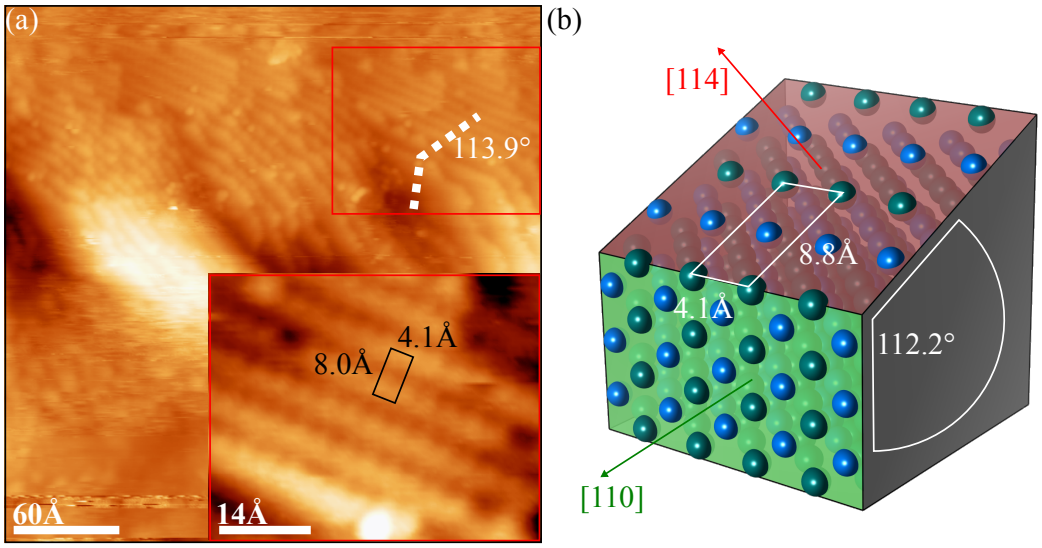

Figure 3.13: (a) STM scan of the region of the surface displaying highly stepped terraces (inset) atomic resolution at the step edges only.(b) Recreation of this facet with the bulk model which allows the identification of the (1 1 0) and (1 1 4) surfaces. The discrepancy between the larger surface unit length is attributed to the large tilt of the plane with respect to the tip, also demonstrated in the variation of angle between the two surfaces.

The image in Figure 3.15 is taken from the full map which was constructed from approximately 300 images with field of view 50 μm . The piecing together of these scans is not seamless, and so there is some change in contrast between connected scans due to this. Once this map was created, it was used to find areas with grains containing 3 or more different contrasting polycrystallites which appeared to have similar tilts. This was then used to perform preliminary LEED which is shown in Figure 3.16 .

Initial LEED data suffered from severe astigmatism due to the often large

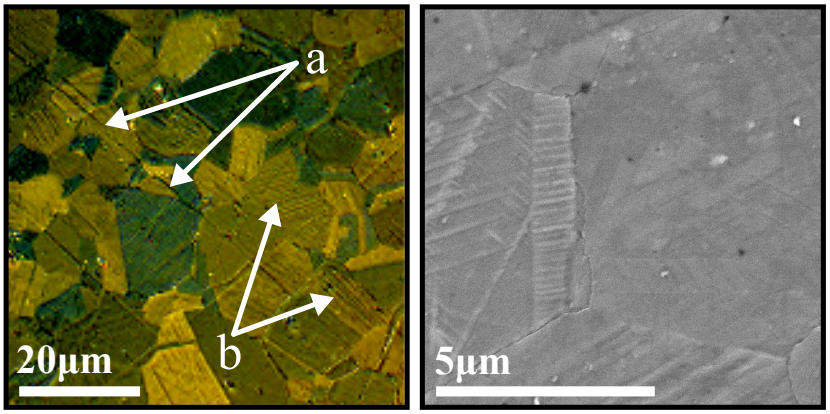

Figure 3.14: (left) plane polarized optical micrograph of ZnPd polycrystal surface. (a) represents polishing grooves (b) represents faceting due to high temperature surface modification. (right) SEM image of surface faceting on different grains.

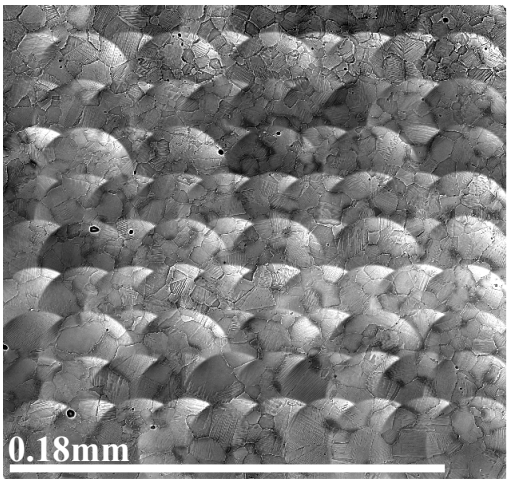

Figure 3.15: Map of ZnPd polycrystal surface using multiple LEEM scans in MEM mode. Scan windows of 50μm were stitched together to provide an overview of the map. The circular patterns are artefacts of the stitching process and not present on the sample.

tilts between grains. The system is set so that the beam is perpendicular to the surface, internal systems in the microscope allow for a tilt correction to the order of 2 ° - 3 °. Grain orientation was often far from this point. To overcome this, it was decided to take LEED patterns of well aligned grains even if they were not

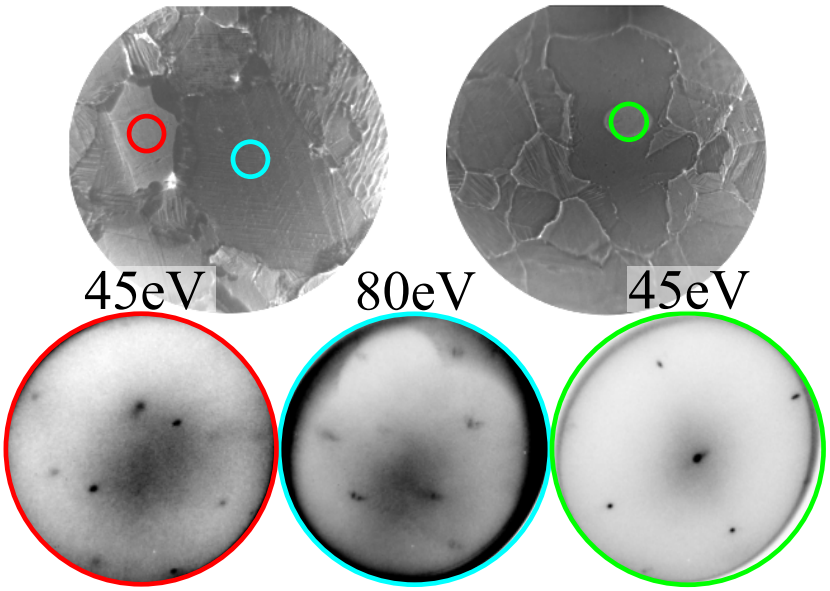

Figure 3.16: Preliminary results from μLEED showing the different LEED patterns present across the surface, distinguishing grains by colour in MEM mode. MEM scans taken with a 50 μm aperture. The blue and green scans show both two-fold and three-fold symmetry as expected for this sample. It appears that the red pattern is a combination of two patterns, possibly due to some twinning in the crystal.

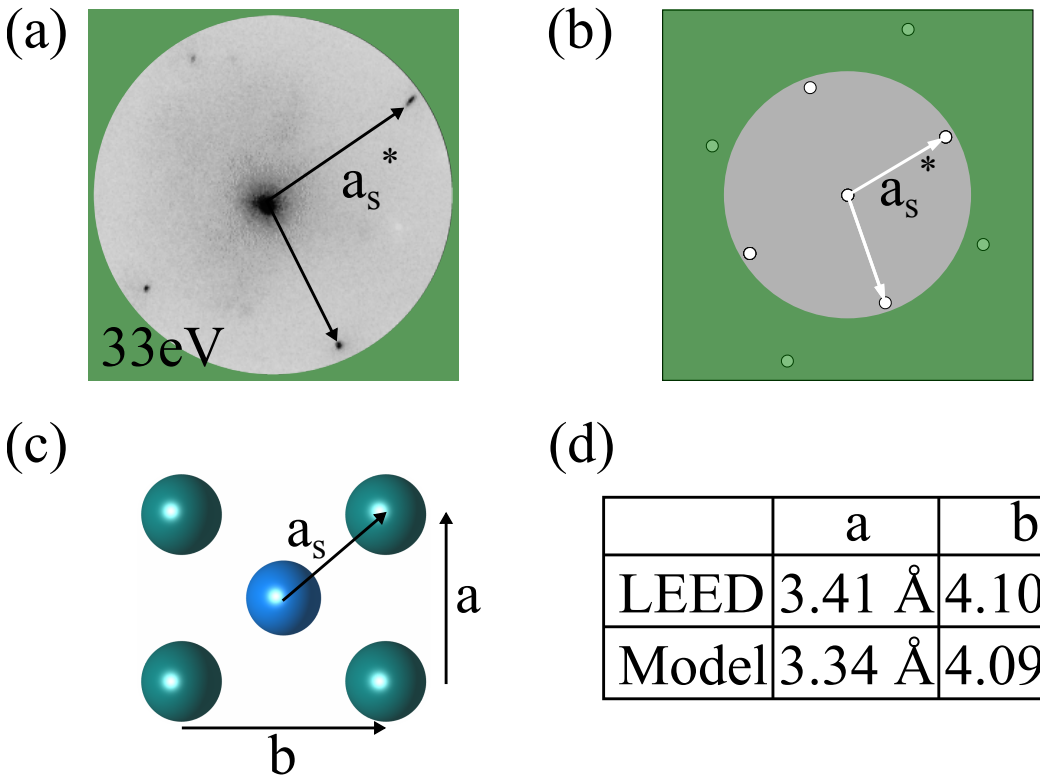

	a	b
LEED	3.41 Å	4.10 Å
Model	3.34 Å	4.09 Å

Figure 3.17: (a) LEED pattern from the (1 0 1) surface of ZnPd. (b) Simulated LEED pattern from model [117]. (c) Surface unit cell from bulk model. (d) Comparison of lattice constants from LEED with model with an estimated uncertainty of 0.1 Å.

in direct proximity to other measurable grains.

Using this technique, improved LEED patterns were achieved that allowed for structure determination. The two-fold diffraction pattern relating to the (110) surface was observed in LEED and can be seen in Figure 3.17. Calculation of the lattice vectors from the LEED patterns was done by scaling each pattern at to a Si(1 1 1) 7×7 diffraction pattern taken on the same machine at the same energy. Scaling took the form of scaling each scan window to the scan window for the Si pattern. This provided a constant value of cm^{-1} per pixel. The reciprocal lattice vector was then calculated by comparison to the reciprocal lattice vector in the Si diffraction pattern. The lack of movement of diffraction spots in LEEM meant that once the window was scaled at the same energy, patterns of different incident electron energies could be compared to the Si pattern. It was then possible to average out the effect of distortions or difficulty in finding the centre of diffuse spots. This pattern is observed frequently across the surface. This suggests that this termination is common but that large flat terraces are not favoured by the crystal due to the limited appearance in STM. Another pattern observed is a three-fold pattern relating to the (1 1 1) surface termination (Figure 3.18). The lattice constants calculated from this surface and characteristic angles between

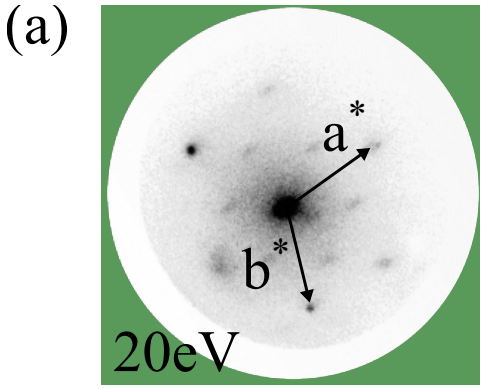

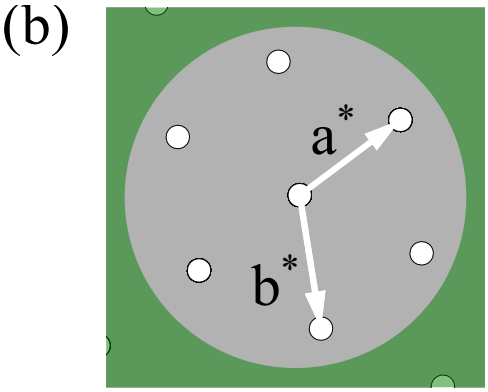

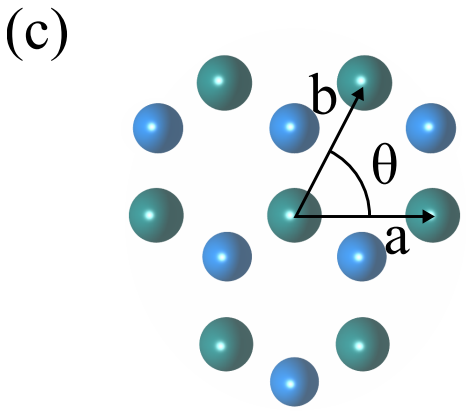

(d)

	LEED	Model
a	4.4 Å	4.1 Å
b	4.7 Å	4.4 Å
θ	63°	62°

Figure 3.18: (a) LEED pattern from the (1 1 1) surface of ZnPd with labelled reciprocal lattice vectors. (b) Simulated LEED pattern from model [117]. (c) Surface unit cell from bulk model with Zn atoms from second layer included. (d) Comparison of lattice constants from LEED with model with an estimated uncertainty of 0.2 Å and 1°.

atoms are in good agreement with the model and STM.

In other areas a two-fold pattern of simply two spots and a specular were common. This is suggested to arise from certain surfaces where the termination is not perpendicular to the macroscopic surface and the periodicity of the step edges produces the diffraction pattern in one direction but there is no coherence along the atoms in the terraces as each terminates at a different point. The levels of astigmatism in the scans and the resulting shift of spots make the calculation of the lattice constant difficult and highly unreliable, and thus this is omitted.

3.4 Summary

A preparation procedure has been developed to enable structural studies on the nm scale of a polycrystalline ZnPd intermetallic compound. The sample was checked with XPS to confirm the intermetallic nature of the surface and the chemical cleanliness of the sample. Following this, STM and LEED studies were

	STM			LEED			Model		
Surface	a	b	ϑ	a	b	ϑ	a	b	ϑ
(1 1 0)	-	4.1 Å	-	3.4 Å	4.1 Å	90°	3.3 Å	4.2 Å	90°
(1 0 1)	4.2 Å	2.7 Å	90°	-	-	-	4.4 Å	2.9 Å	90°
(1 1 1)	4.4 Å	4.6 Å	53°	4.4 Å	4.7 Å	54°	4.1 Å	4.4 Å	55°
(1 1 4)	4.1 Å	8.0 Å	90°	-	-	-	4.1 Å	8.8 Å	90°

Table 3.6: Summary of the measured surfaces using LEED and STM in comparison to the bulk model. All identified surfaces fit well with the ZnPd model.

performed to understand the surface termination tendencies of the crystal. Experimental studies were in good agreement with surfaces associated with bulk structures previously obtained by experimental methods. The presence of certain favoured terminations was also in agreement with DFT calculations performed by collaborators on surface stabilities.

The (1 1 0), (1 0 1) and (1 1 1) surfaces of the crystal were found across the crystal using a combination STM and/or LEED, summarised in Table 3.6. The presence of the (1 0 1) and (1 1 0) surfaces was in good agreement with DFT calculations of surface stability. The tendency of the crystal to undergo an elevated temperature modification to the (1 0 1) surface was predicted from calculations and observed experimentally. The presence of the (1 1 1) surface is somewhat unexpected as this is a single element terminated surface, although not forbidden. It is suspected that the (1 0 1) and (1 1 0) surfaces may be responsible for some of the catalytic behaviour of the material. At reaction temperatures, the crystallites would be expected to undergo the modification to the (1 0 1) surface, also the most dense in the BCT structure, which would provide a fixed site isolation for the Pd atoms.

The observed common surface terminations are relevant because they all contain surfaces constructed from Zn-Pd atomic pairs (Figure 3.19) . This is in agree-

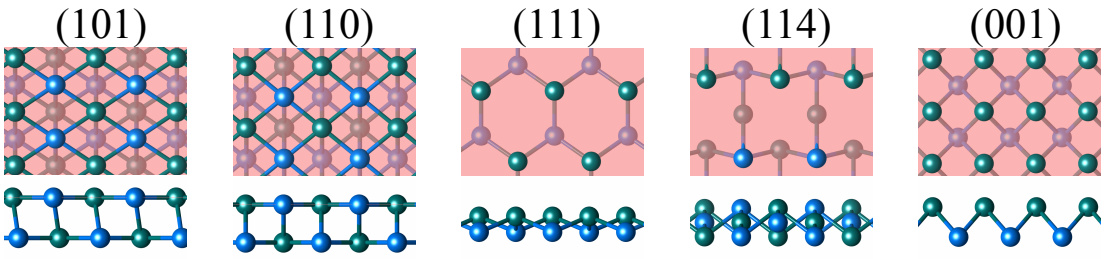

Figure 3.19: Graphical summary of observed and predicted common surfaces, plus the (0 0 1) surface which is not present for comparison. Side view demonstrates that the surfaces which were single element terminated had Zn-Pd bonds close to parallel with the surface. The (0 0 1) surface, which has not been observed has single element termination and no bonds close to the surface parallel.

ment with the observations from the literature about the greater bond strength between Zn and Pd compared to Pd-Pd or Zn-Zn bonds in the crystal. Even the Pd terminated (1 1 1) surface is constructed from Zn-Pd pairs, as the Zn sits only slightly lower than the Pd in the structure (approximately 0.9 Å). An omission in the observed surface is the (0 0 1) surface which is the only fully single element terminated surface, no evidence for this surface has been seen, and this is suggested to be due to the lack of Zn-Pd bonded pairs in or close to the surface. While other surfaces are single element terminated, the d spacing to the next layer is small, except for the case of (0 0 1).

Further work would be to use these surfaces to perform deposition studies, to investigate the relationship between Pd-Pd separation in the (1 1 0) and (1 0 1) surfaces and the adsorption of methanol or water. Also, to bridge the materials and pressure gaps, it would be interesting to use small ZnPd nanoparticles, heat treated for long enough to ensure the completed modification of the surfaces to (1 0 1), and then perform flow reactor experiments under reaction conditions.

Chapter 4

Quasicrystals as Precursors to Catalysts for Hydrogen Production

4.1 Introduction

Quasicrystals (QCs) are intermetallic compounds with long-range ordered structures but no translational symmetry. Possessing classically forbidden symmetries such as five-fold and tenfold they are only found in distinct stoichiometries. Quasicrystallinity was first observed in 1982, when icosahedral symmetry was evident in the TEM diffraction patterns of rapidly solidified Al-Mn alloys [118]. The physical properties of these materials differ from their elementally similar simple intermetallic compounds or amorphous alloys, in having low coefficients of friction [119, 120], high hardness and wear resistance [121, 122], corrosion resistance [123], low thermal conductivity and low electrical conductivity [121, 124].

The icosahedral Al-Cu-Fe QC, for example, exhibits a coefficient of friction comparable to that of TEFLON© [125, 126], a hardness comparable to silica [121, 127], a thermal conductivity some 200 times less than pure aluminium and an electrical conductivity over 2,500 times larger than aluminium [128–130]. While possessing these promising properties the applications of quasicrystals remain niche.

In recent years there has been increased research into the possibility of utilizing QCs within the area of heterogeneous catalysis, specifically the steam reforming of methanol for hydrogen production [131–135]. Most quasicrystals contain catalytically active elements (for example, Pd, Cu, Fe, Ni), while also being brittle enough to facilitate high surface area through crushing. The steam reforming of methanol is being investigated for its benefits as a reaction for mobile hydrogen

production for methanol fuelled, hydrogen fuel cell powered vehicles [136].

Currently, Cu based catalysts are used industrially for the steam reforming of methanol but suffer from thermal instability and rapid degradation due to sintering of Cu particles which reduces the surface area of the catalyst [13]. In previous work performed by Tsai *et al.*, Al-based quasicrystals were found to show desired activity and stability for the reaction, once powdered samples had been chemically treated in NaOH [131, 134, 135, 137–139]. These materials also contain no precious metals and therefore are relatively cheap to manufacture. This leaching treatment was initially used to remove the passivating oxide layer arising from the surface Al, although the study showed the removal of Al metal from the quasicrystal also. When the Al-Cu-Fe quasicrystal was leached, all that remained in the surface region, as determined by x-ray diffraction (XRD), were Cu and Fe metal plus oxides in the form of nanoparticles. These nanoparticles are believed to be responsible for the catalytic activity, whereby the Fe species act to disperse the active Cu species and inhibit sintering.

This type of leaching process is more commonly used in the production of Raney catalysts, and in the case of steam reforming of methanol, especially Raney Cu catalysts [51, 52, 140]. The leaching treatment in these materials allows the removal of Al species leaving behind a porous 'skeletal' structure of Cu catalyst. Leached QCs have been shown to have a higher surface area, higher surface area of Cu specifically and greater Cu dispersion across the surface [135]. In reaction studies leached QC catalysts have been found to produce more H_2 in comparable conditions. It is known that while sintering of Cu in Raney catalysts begins at even low reaction temperatures, Cu in QC catalysts has been shown to remain dispersed, and 'remarkably stable' [135]. This was attributed to either the dispersion effect of Fe or the interaction with the QC structure. The QC was also found to have a point where the leach depth saturated, whereas this was not found in either the approximant or crystalline sample.

The Al-Cu-Fe approximants, which are periodic but have local structure and chemical composition similar to QCs, show less advantageous behaviour after treatment in comparison to the quasicrystal. A higher Al dissolution rate in the crystalline samples, because of homogeneous distribution of Al, produces layers of Cu species and not the desired dispersal of the active sites, leading to unfavourable activity [137]. This result suggests that the crystal structure, namely the periodic access to Al in the structure, may affect the behaviour of the crystal during leaching. This was also evidenced by the variation in leaching depth observed using cross sectional TEM. The QC catalysts were found to spontaneously cease leaching at a depth of approximately 500 nm, whereas there appeared to be no limiting factors in the leaching penetration of compositionally similar crystalline

materials [138].

The inherent complexity associated with quasicrystals have made the understanding of the changes associated with the surface difficult to determine. It was with this motivation that our experiment focused on recreating the treatments carried out by Tsai *et al.* on simplified model systems. These model systems are single grain crystals with well oriented and well-understood surfaces. Nanoparticles of the catalytically active metals are produced on the surface, through an adaptation of the leaching treatment. X-ray photoelectron spectroscopy (XPS), ultraviolet photoelectron spectroscopy (UPS) and energy dispersive x-ray spectroscopy (EDX) were used to investigate the influence of leaching treatment on surface chemical composition and valence band structure of the five-fold surface of *i*-Al-Cu-Fe QC. The electronic structure and chemical nature of the surface are known to be key influences on the catalytic behaviour of a crystal. In this case it is important that the surface exhibits Cu-like electronic structure from the Cu present in the structure. The microstructure of the surface after leaching was also investigated by transmission electron microscopy (TEM), scanning electron microscopy (SEM) and atomic force microscopy (AFM). The concept of active site separation is well established in catalysis, and by understanding the microstructure of the surface, it is possible to come to conclusions about the surfaces ability to provide this separation. Selected area electron diffraction (SAED) is used to establish the epitaxial relationship between the nanoparticles and the underlying quasicrystal.

In addition the five-fold surface of *i*-Al-Cu-Fe was leached and studied as a model system to understand the nanoparticle formation and the effect of the interaction between these particles and the underlying QC structure. The results presented below provide insight into the requirements for the preparation of model catalysts for the steam reforming of methanol.

4.2 Experimental Methods

In order to recreate the studies performed by Tsai *et al.* on model systems a single grain of *i*-$Al_{63}Cu_{24}Fe_{13}$ was grown by the Bergman method [141]. The surfaces were polished and cleaned before each leaching treatment, polishing was performed manually with diamond paste down to 0.25 μm size. The samples were then placed in methanol and cleaned using a sonic bath. Figure 4.1a shows an SEM image of the unleached, polished *i*-Al-Cu-Fe five-fold surface which displays virtually no features barring some scratches resulting from polishing. An EDX derived surface composition of Al: 63.4 at%, Cu: 23.2 at% and Fe: 13.1 at% (O: 0.3 %) was found, which is close to the expected nominal composition. The

oxygen component was as expected from the air exposed sample.

Figure 4.1b shows the LEED pattern obtained from the *i*-Al-Cu-Fe five-fold surface following repeated cycles of UHV treatment (sputter-anneal, see section 2.1.2) of ion bombardment with 2 keV argon ions for 30 minutes and annealing at 870 K for 4 hours. The pattern displays five-fold symmetry consistent with icosahedral structure and τ scaling of the diffraction spot distances. The irrational number, τ or golden mean, is intrinsically linked with quasiperiodicity and its presence in this pattern, plus the five-fold symmetry serves to confirm the single grain nature and consistency of the exposed surface. After this the leaching treatments were performed.

Leaching was performed in ambient conditions by pipetting 10 mol conc. NaOH onto the sample surfaces for systematically increasing times. Following leaching the samples were cleaned in deionised water then methanol to remove all remaining traces of the alkali solution. This is explained further in Section 4.3.4. The microstructure of the surfaces was then studied using SEM, EDX, AFM and TEM/SAED.

The effect of leaching on the surface was initially studied optically. In Figure 4.1a (inset), optical micrographs of the *i*-Al-Cu-Fe crystal before and after leaching are shown. It is clear from these that the surface was aggressively leached during process. The surface had a mirror finish before leaching and then had greatly reduced reflectivity and become a reddish brown colour. This changes to black with increased leach time.

TEM was carried out by collaborators on a thin strip of the leached sample (10 μm thick) using a FEI-Tecnai 20 G2 electron microscope at 200 keV employing imaging and diffraction modes. TEM provides a powerful combination of techniques as it allows for near simultaneous observation of both high resolution

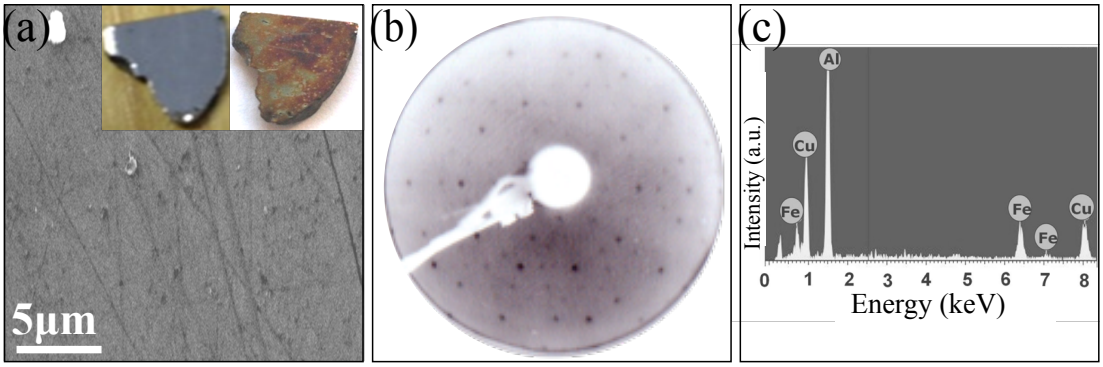

Figure 4.1: (a) SEM image of polished *i*-Al-Cu-Fe surface (inset: optical images of polished and leached surfaces). (b) LEED pattern from same surface after UHV preparation. (c) EDX spectrum from clean, polished surface showing peaks for Al, Cu and Fe.

microscopy and diffraction through SAED. The thickness of the leached area in the strip was less than 1 μm as estimated from the brightness of the transmitted beam. The sample used for the TEM and SAED measurements was different from the one used for the other experiments. The sample was grown as described in Ref. [142]. The composition was *i*-$Al_{63}Cu_{25}Fe_{12}$, which was very close to the first sample. XRD confirmed the single icosahedral phase of the sample. The sample consisted of multi-grains with grain size of 30 μm - 50 μm. The TEM results analyzed here were obtained from single grains. The sample was leached with the same method as before. Although the orientation of the surface was random in this sample, the sample could be adjusted in SAED experiments in order to probe the interface parallel to the five-fold surface. The SAED patterns presented in this thesis were obtained with a tilt angle of about 2° from the beam normal. Therefore, the surface orientation of the chosen grains was almost five-fold.

Following chemical treatment the crystal was placed in UHV (10^{-10} mbar) for XPS and UPS measurements. XPS measurements were taken in the laboratory of collaborators at the Institut Jean Lamour, Nancy. The sample was placed in the fast entry lock of the system and pumped down for 12-14 hours before being inserted into the analysis chamber. XPS and UPS measurements provide information about the chemical composition and bonding nature of the surface, this is highly important in model catalyst preparation. The electronic structure and adsorption properties of the material are instrumental in determining the catalytic activity and specificity.

Ultrasonic cleaning using methanol is a standard procedure for UHV experiments. However, it was not possible to remove species related to the remains of the leaching solution from the surface by this method. XPS from the surface cleaned with methanol showed the presence of Na salts and oxides as a result of the leaching treatments. The XPS spectra were completely dominated by the peaks associated with the Na core levels, plus large O and C peaks such that the core levels of the expected quasicrystal components were not visible (Figure 4.2) . The residual species from the NaOH solution was dissolved after washing with deionized water. This then allowed the use of methanol cleaning, in line with typical UHV/surface science methods.

The surface after leaching, followed by washing with water, yielded an XPS spectrum exhibiting the core level peaks of the constituents of the quasicrystal. However, the surface was still heavily contaminated from being exposed to air before insertion into UHV. This led to scans lacking in intensity and diffuse peaks. Sputtering the surface using 2 keV Ar^+ for 30 - 40 minutes removed the physisorbed species of both C 1*s* and O 1*s* (Figure 4.3) , increasing the detail of the peaks. As shown in Figure 4.3, the C 1*s* peak could be fitted with four

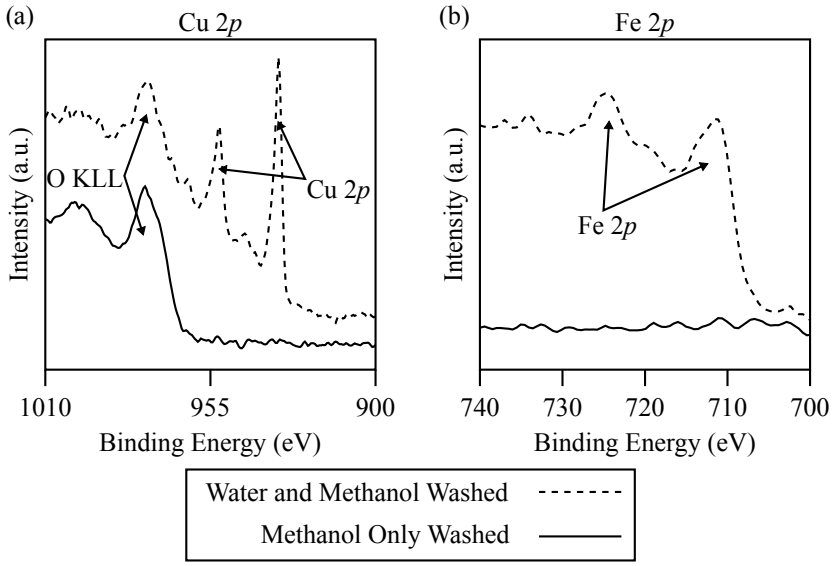

Figure 4.2: (a) Cu 2p and (b) Fe 2p XPS spectra (Al K_α source) from the five-fold i-Al-Cu-Fe surface after leaching (1 hour), followed by water and methanol, and methanol-only washing procedures. The detail of the metal species is completely lost without the extra washing routine.

components corresponding to the C 1s core levels of C-C, C-O, C=O and O-C=O compounds [143]. All of these peaks are absent after sputtering.

The sputtering process also enables the detection of the subsurface region by XPS as this treatment removes several top surface layers. The cleaning process

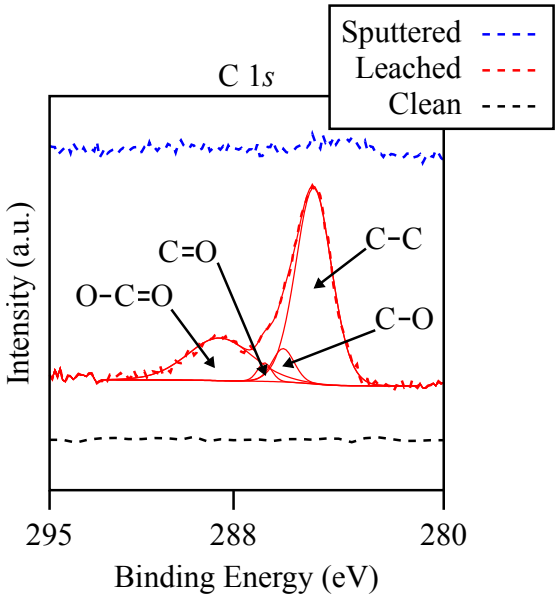

Figure 4.3: C 1s XPS peak (Mg K_α source) from the surface after leaching (2 hours) and subsequent sputtering in UHV. A spectrum of the clean quasicrystal surface prepared in UHV is also given for comparison. Solid curves correspond to the results of fits using a Gaussian Lorentzian convoluted lineshape. The species appear as 'adventitious' carbon but are completely removed by sputtering.

(washing with water followed by methanol) was the same for all of the experiments.

4.3 Results

4.3.1 Effect of Leaching on Microstructure

The SEM micrograph in Figure 4.4 displays the surface microstructure following increasing leach times. Thirty minutes leaching results in large but shallow cracks across the surface. However longer treatments result in greater effects. Indeed after 2 hours the surface begins to display pentagonal cavities in some of the more heavily leached regions. The edge-length of these pentagons varies from 3 μm to 5 μm, with larger pentagons the result of longer leaching exposure, the density of these indentations also increases with leaching time. Interestingly, the pentagonal cavities all share a common orientation and seem to be clearly influenced by the underlying structure of the quasicrystal. In all our studies, only two pentagonal facets were found not to share the orientation of their neighbours, but the orientation was rotated by n $\times$ 36°, still consistent with the underlying QC.

After 8 hours of leaching dodecahedral cavities are formed. These are shown in Figure 4.4d and 4.4e. The boundary between the pentagons is leached much

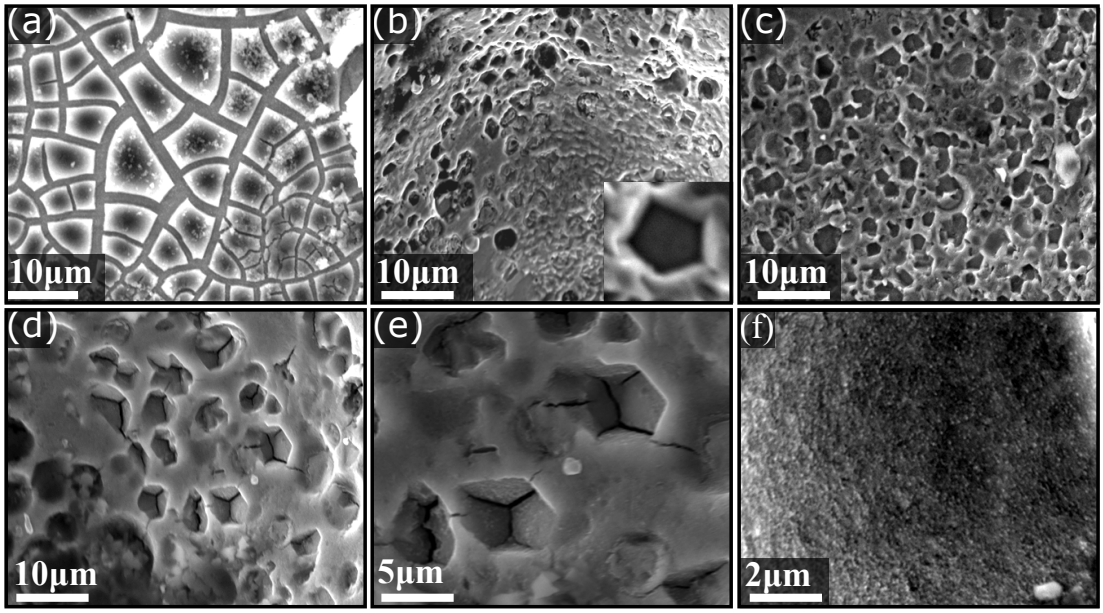

Figure 4.4: (a) SEM images of the five-fold *i*-AlCuFe surface after leaching at increasing times: (a) 30 minutes, (b) 120 minutes, (c) 240 minutes, (d) and (e) 480 minutes, and (f) 60 minutes. Pentagonal facets relating to the quasicrystal are present after 120 minutes of leaching, they then increase in size and number with increasing leaching time.

deeper still. The formation of the dodecahedral cavities can be explained if the surface is preferentially leached along all five-fold planes, and not limited to the five-fold plane parallel to the surface [90]. The icosahedral quasicrystal has six five-fold axes inclined at 63.4° from each other as can be seen in Figure 4.5 . The structure also has ten three-fold axes located 37.4° away from the five-fold axis and fifteen two-fold axes located 31.7° away from the five-fold axis [144]. There was no evidence of any explicitly two-fold or three-fold facets or features on the leached surface. This supports a suggestion that the leaching susceptibility of the crystal is highly influenced by crystallographic direction not surface orientation.

This result closely resembles results of many of the oxidation studies performed on *i*-Al-Cu-Fe. Similar five-fold faceted holes have been seen in oxidation studies on the QC, and a reduced oxidation kinetic observed for the QC in comparison to crystalline samples of similar composition [145–149]. In those studies it was concluded that microvoids in the structure which are common in the *i*-Al-Pd-Mn family of QCs act as starting points for the holes which then grow according to crystallographic directions. Chapter 5 contains further work to help understand this observation.

High magnification of the SEM images shows a seemingly continuous layer of nanoparticles across the surface, atop flat regions, heavily leached regions and facets. AFM was used to get information on particle size. AFM images reveal the porous nature of the surface after leaching (Figure 4.6b-c) , in agreement with high resolution SEM. The root mean square roughness of the surface estimated from the 10 μm × 10 μm AFM image is about 30 nm, although in some places the roughness is much larger. Particles of two different sizes can be identified in AFM; the brighter features have larger lateral size than the grey features. The small particles are predominant. The size of the large particles is up to about 200

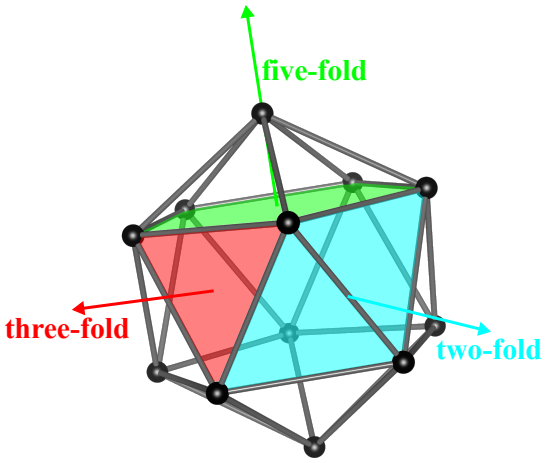

Figure 4.5: The icosahedral structure with two-fold, three-fold and five-fold symmetry axes and surfaces.

nm while the small particles are of approximately 20 nm size, which is comparable to the particle size observed on the leached powder by Tsai *et al.* [131]. This size is also in good agreement with our TEM results, which are discussed in Section 4.3.2.

4.3.2 Study of the Interface Region

Figure 4.7a shows a representative TEM microstructure of a thin strip of the sample after leaching at 8 hours, where the leached and un-leached areas are marked by 'B' and 'A', respectively. Nanosize particles are observed in the leached area, which are clearer in the high magnification image given in Figure 4.7b. The particle size was found to be 5-20 nm, which agrees well with the AFM results and powder samples [131].

The interfacial relation between the nanoparticles and the underlying quasicrystal was determined by comparing SAED patterns from the leached and un-leached areas. SAED patterns recorded by scanning the electron beam across the co-existing leached and un-leached areas are shown in Figure 4.7c, d. As expected, the un-leached region yields patterns characteristic of the icosahedral quasicrystal. However, the leached area produces rings instead of spots, (Figure 4.7d). The ring patterns suggest that the leaching treatment yields nano-grain microstructures aligned randomly on the quasicrystal interface.

The reciprocal lattice vectors (k-vectors) of the rings are consistent with those for elemental Cu and Fe, Cu_2O and Fe_3O_4. The rings are indexed in Figure 4.7e. In addition, the k-vectors of some of the rings match with those of the quasicrystal. The strongest diffraction spots from the quasicrystal, at 3.1 $Å^{-1}$ (= k_0), coincide with the Cu(111) and Fe(110) rings with a mismatch of only 2% - 3%, which is within the experimental uncertainty. The matching of the k-vectors sug-

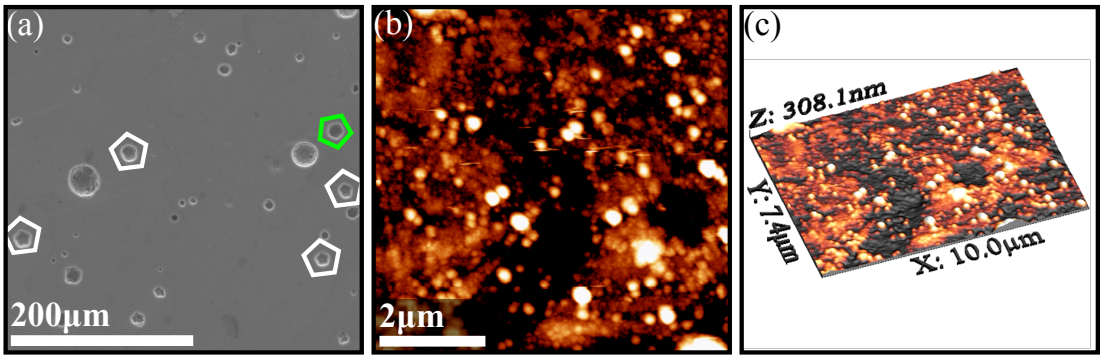

Figure 4.6: (a) SEM image of the five-fold *i*-Al-Cu-Fe surface after leaching at 8 hours showing five-fold cavities across the surface (30 kV beam energy). (b-c) AFM images of precipitate nanoparticles on the surface visualized in both 2D and 3D (leaching time 8 hours). AFM images were obtained in ambient conditions.

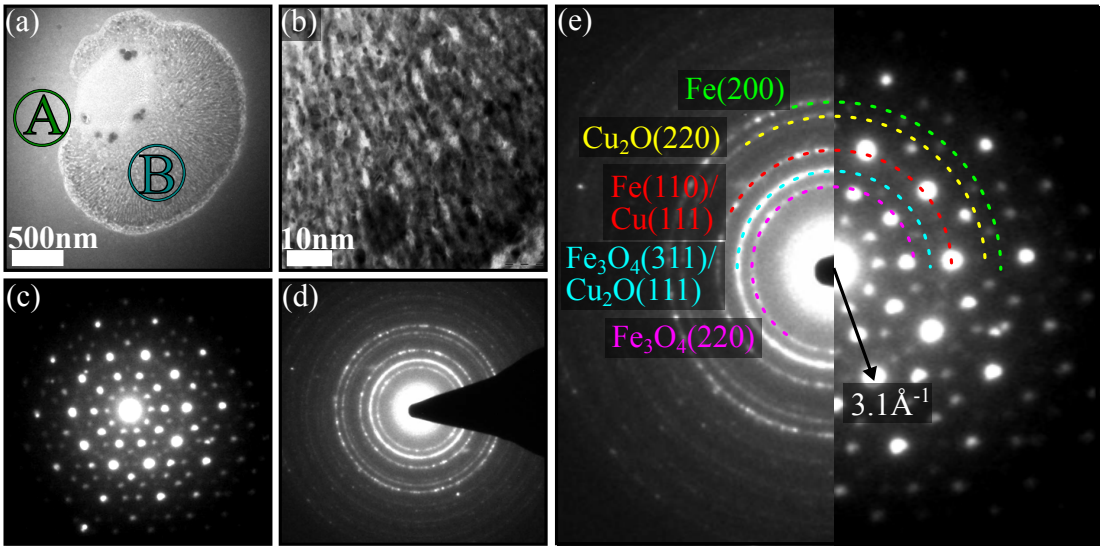

Figure 4.7: (a) Bright field microstructure of the *i*-Al-Cu-Fe quasicrystal after leaching for 8 hours. 'A' and 'B' mark the un-leached and leached areas, respectively. (b) Highly magnified image of the leach region 'B'. (c-d) Selected area electron diffraction (SAED) patterns from region 'A' (c) and 'B' (d). (e) Comparison of SAED patterns from the leached and un-leached area. The k-vector of the high density Fe and Cu metals can be seen to overlap with the brightest spots from the QC structure indicating some ordering in the interface between them. It appears that the Fe(1 1 0) and the Cu(1 1 1) are in contact with the surface.

gest the formation of an interface between the five-fold surface and high atomic density planes of Cu(111), Fe(110) and Fe(200). This is in agreement with the conclusion drawn from the XPS results (section 4.3.4) that the subsurface region after leaching is richer in elemental Cu and Fe than the oxide. Cu(111) and Fe(110) are the highest atomic density planes, Cu and Fe having fcc and bcc structure, respectively. Fe(200) has the second highest atomic density in the Fe bcc structure. Similarly, the five-fold surface of the *i*-Al-Cu-Fe QC terminates at high density planes of the bulk structure. This suggests that the interface is formed between the high density planes of nano-particles and the quasicrystal. Previous studies have shown that the *i*-Al-Cu-Fe quasicrystal powder shows higher thermal stability than metal catalysts in steam reforming of methanol [131]. It is suggested that the interface between high density planes may provide or influence this higher stability.

4.3.3 Chemical Composition of Surface and Near Surface Region

EDX was used alongside SEM during initial studies to understand the local chemical environment on the surface. The observed nanoparticles were composed of

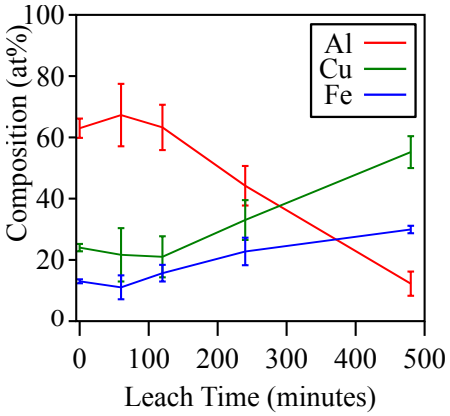

Figure 4.8: Change in chemical composition of the *i*-Al-Cu-Fe five-fold surface as a function of leaching time, determined by averaging EDX measurements across the surface. The Al signal decreases with leaching time as the leaching depth increases. The uncertainties were calculated from the standard deviation after the averaging process.

Cu and Fe which appeared homogeneously distributed across the surface. EDX is unable to provide information about the oxidation states or chemical bonding and cannot be considered truly surface sensitive. A trend of compositional change with leaching time is shown in Figure 4.8. The composition was determined by EDX taken at different locations across the surface by averaging compositions taken across the surface for each leaching procedure. As can be seen in the graph, there is selective removal of Al, while correspondingly the Cu and Fe contents increase. Due to the information depth of EDX, the Al signal (from the bulk) can be considered analogous to the depth of the leached region. This shows that even after 8 hours being leached with high concentration NaOH. This technique is still able to 'see' the bulk. This demonstrates that the leached region is shallow, of the order of several hundred nm.

4.3.4 Study of the Core Level Modifications

The surface chemical composition after different surface treatments was determined by analyzing the XPS spectra. XPS spectra from the clean (sputter-annealed), leached and leached-sputtered surfaces are compared in Figure 4.9 . The core level binding energies of the species after each treatment are presented in Table 4.1 and compared with those from pure metals and their oxides. The core level binding energies were analyzed by fitting the peaks using a Gaussian-Lorentzian curve and Shirley background subtraction. An example of such a fit is given in Figure 4.3. The uncertainty in the given core level binding energies is estimated to be 0.1-0.2 eV. Each of the core levels of each species is discussed in the following order, Al, Cu, Fe and O. Following these a study of the surface

composition is presented.

Al Core Levels

As shown in Figure 4.9a, the Al $2p$ peak of the clean surface disappears after leaching. The Cu and Fe core levels are still detected. This confirms the selective dissolution of Al from the surface. XPS spectra shown in Figure 4.9 were taken

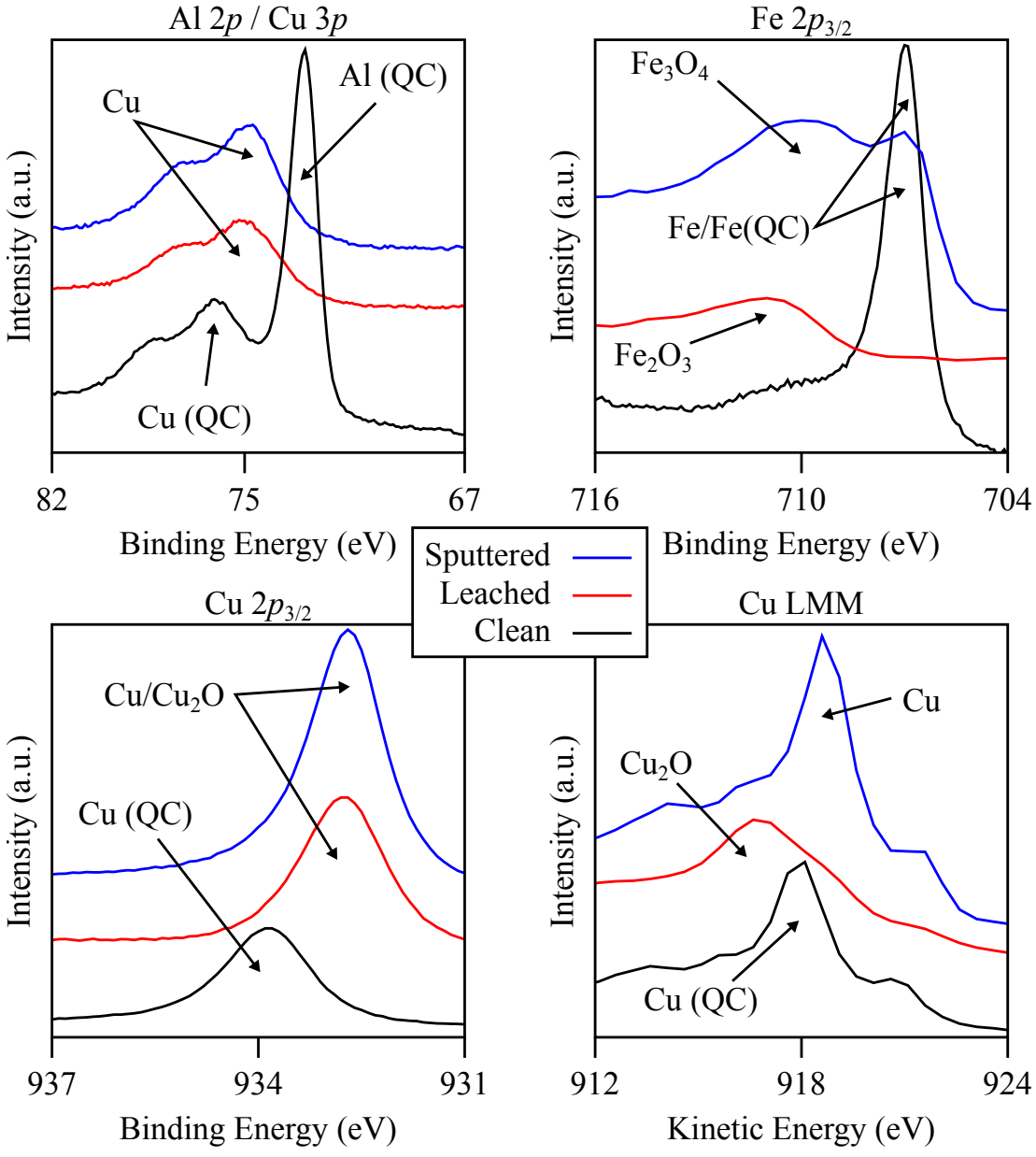

Figure 4.9: (a) Al $2p$/Cu $3p$, (b) Fe $2p$, (c) Cu $2p$, and (d) Cu LMM spectra (Mg K_α source) from the five-fold *i*-Al-Cu-Fe surface after leaching (2 hours) and subsequent sputtering. Results from the clean surface are also given for comparison. The changes demonstrate the removal of any features from the QC following leaching. Following sputtering the Cu_2O is removed to leave Cu metal and Fe_2O_3 is removed to leave Fe_3O_4 and Fe metal.

	Al $2p$	Cu $2p_{3/2}$	Fe $2p_{3/2}$	O $1s$	C $1s$	Cu $L_3M_{45}M_{45}$
Elemental	72.8[150]	932.6	706.9[151]	531.0	284.9	918.6
Clean QC	72.9	933.8	707.0	-	-	918.1
Leached	-	932.7	711.0	530.2, 532.0	284.9	917.1
Leached + Sputtered	-	932.7	707.0, 710.0	530.4	-	918.6
Fe_3O_4	-	-	710.6[151]	530.1[151]	-	-
Fe_2O_3	-	-	711.0[151]	529.8[151]	-	-
Cu_2O	-	932.5[152]	-	530.5[152]	-	916.5[153]
CuO	-	933.8[152]	-	529.6[152]	-	917.8[153]

Table 4.1: Binding energies (eV) of Al, Cu, and Fe core levels in various forms: elemental, oxides, clean *i*-Al-Cu-Fe quasicrystal, quasicrystal after leaching treatment (2 hours) and subsequent sputtering. The last column presents kinetic energies of the Cu LMM Auger transition. This demonstrates the presence of metals following leaching and sputtering in addition to oxide material.

after 2 hours leaching. Other data show that the Al $2p$ peak of the clean surface is already removed after 1 hour leaching. Longer exposure to the leaching solution modifies the composition of the Cu and Fe species in the surface. The Al core levels of the clean surface were not detected even after sputtering, indicating the absence of Al in the subsurface region too. Although no Al from the clean surface was observed, a trace of aluminium oxide is detected. This was evidenced by a shift of the Al $2s$ peak to a higher energy (Figure 4.10). The Al $2p$ peak of the oxide overlaps with the Cu $3p$ peaks and thus it is difficult to identify the oxide contribution by analyzing the Al $2p$ peak. A trace of Al oxide was detected even after the surface was sputtered.

Cu Core Levels

The Cu core levels are shifted to a lower binding energy after leaching (Figure 4.9a and 4.9c). The Cu $2p_{3/2}$ is shifted to 932.7 eV, which is close to the binding energy of elemental Cu or Cu_2O. The Cu $2p$ core level in elemental Cu and in Cu_2O is separated only by 0.4 eV [154]. Thus, it is difficult to distinguish the two species by XPS with the given experimental resolution. However, they can be distinguished by comparing the Cu Auger transition peak, as the Cu LMM Auger peaks of the two species are separated by about 2 eV [153].

The Cu LMM Auger peak from the leached surface is observed at 917.1 eV kinetic energy (Figure 4.9d), which is close to the Cu LMM transition for Cu_2O or CuO [153]. However, the formation of CuO can be ruled out based on the observed Cu core levels. The Cu $2p$ for CuO is expected to be shifted to higher binding energy by 1.2 eV with respect to elemental Cu but no shift is expected for Cu_2O. CuO also exhibits a total of four peaks in the $2p$ region whereas only 2

were observed. No shift in the Cu $2p$ level was observed, confirming the absence of CuO. After sputtering, only a trace of Cu_2O is detectable and a new peak appears at 918.6 eV, which is the characteristic energy of elemental Cu. This suggests the presence of elemental Cu in the subsurface region.

Fe Core Levels

An XPS spectrum from the clean *i*-Al-Cu-Fe surface shows the Fe $2p_{3/2}$ peak at 707.0 eV (Figure 4.9b). The peak appears at almost the same binding energy as elemental Fe [151]. The Fe $2p_{3/2}$ peak is shifted to higher binding energy after leaching, which is attributed to the formation of Fe oxides. After sputtering, an additional peak emerges, as in the case of the Cu species discussed above. This new peak appears at the same position as elemental Fe, or Fe in the *i*-Al-Cu-Fe QC. Since no other evidence of the underlying quasicrystal can be identified by XPS following leaching and even after sputtering, it is concluded that this peak must be due to elemental Fe, and not from the quasicrystal. If the bulk is probed, Al, the dominant constituent, should also be detected. Al was not detected after sputtering as discussed above.

Because of peak width, it is not possible to precisely determine the position of the Fe $2p$ peak of the oxide. However, it is clear that after sputtering the Fe $2p_{3/2}$ peak is shifted to a lower binding energy by about 1 eV. This shift can be explained if the top layers are predominantly Fe_2O_3 and the subsurface contains Fe_3O_4. The Fe $2p$ peak of Fe_2O_3 is expected to appear at higher binding energy

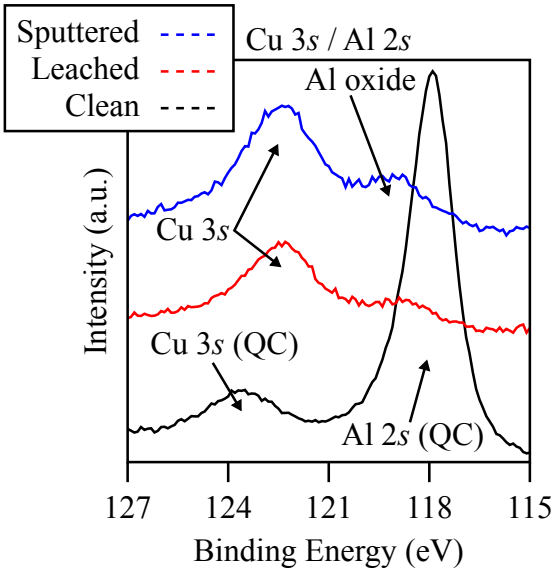

Figure 4.10: XPS of Cu $3s$ / Al $2p$ core levels following treatments. While the Al signal from the quasicrystal completely disappears there is a small shoulder indicating the presence of trace amounts of Al oxide.

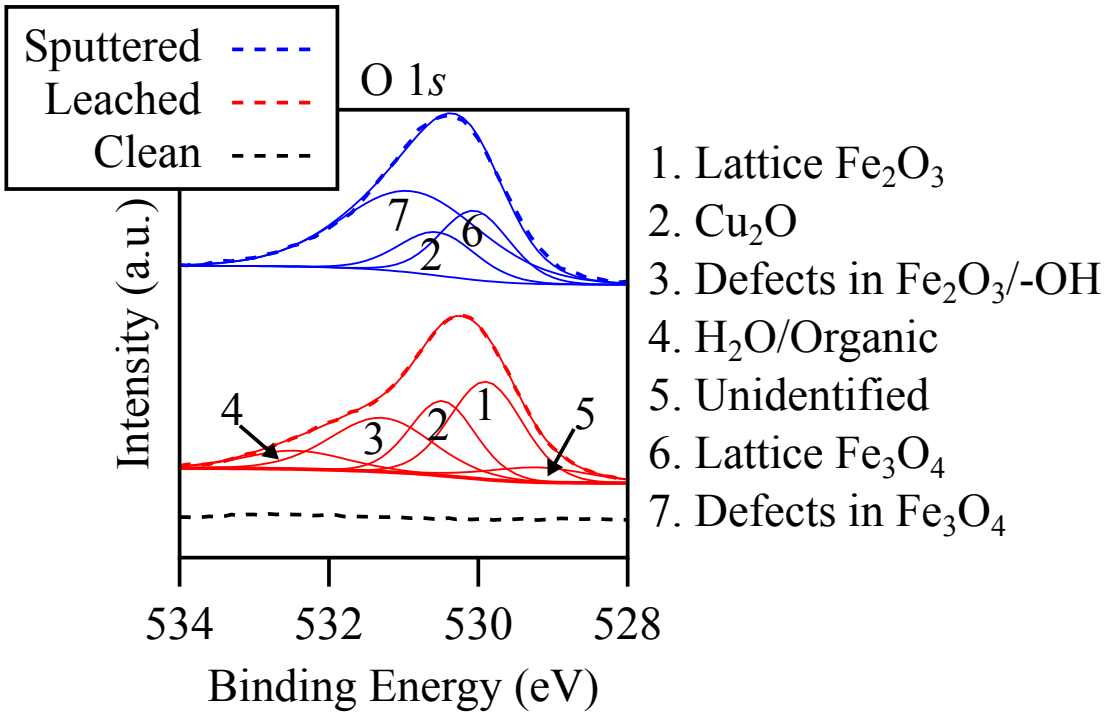

Figure 4.11: O 1s XPS core level (Mg K_α source) from the surface after leaching (2 hours) and subsequent sputtering in UHV. The spectrum from the clean quasicrystal surface prepared in UHV is also given for a comparison. All metal-oxide species identified from metal core levels are confirmed in the O 1s peak. The unidentified species in the leached sample shows some resemblance to FeO but not enough corroborating evidence was observed to confirm this.

than Fe_3O_4 (Table 4.1). Sputtering removes the top layers of Fe_2O_3 and thus exposes the subsurface Fe_3O_4. The existence of both oxides was cross-checked by analyzing the O 1s core level, which is described below.

O Core Levels

Fitting the O 1s peak is challenging because of the presence of multiple oxides and hydroxides. Nevertheless, the O 1s peak after leaching can be fitted by five components (Figure 4.11) . By comparing the peak positions with XPS results from Fe nanoparticles dispersed on a glass substrate [155], it is suggested that peaks 1 and 4 are due to Fe_2O_3 and water, respectively. Peak 3 is related to hydroxide and/or defects in the Fe_2O_3 lattice [155]. Peak 2 is contributed by Cu_2O [152]. The binding energy of peak 5, which is weaker in intensity, is close to the O 1s core level of FeO [156]. However, it is difficult to confirm the existence of FeO by analyzing the Fe core levels because of low peak intensity. After sputtering, the water and hydro-oxide peaks are removed. Nevertheless, a contribution from Cu_2O is still detectable, in agreement with the Auger result discussed above. The O 1s peak after sputtering can be fitted with only three

components: O 1s of Cu_2O, Fe_3O_4 and defective oxygen sites of Fe_3O_4 [155].

Layered Surface Model

Based on the surface chemical composition analyzed above, a model structure of the surface yielded by leaching and subsequently washing with water is proposed. The surface consists of layers of different compositions. The top layers contain Fe_2O_3 and Cu_2O, while the subsurface layer contains elemental Cu, Fe, Fe_3O_4 and a trace of Cu_2O. Fe_2O_3 is expected to form an overlayer in Fe-based compounds upon oxidation [151]. The formation of the layered structure is affirmed based on the fact that only the oxide species were observed before the surface was sputtered, while the elemental species emerged only after sputtering. Our hypothesis is that the top oxide layers are removed by sputtering, exposing subsurface layers to be detected by XPS. Fe_2O_3 is not observed after sputtering and Cu_2O is significantly reduced. This indicates the absence of Fe_2O_3 and only a trace of Cu_2O in the subsurface region.

After the leaching experiments, the surface was polished and prepared in UHV by sputtering and annealing, and was examined by LEED and STM. The surface exhibited quasicrystalline LEED patterns characteristic of the clean surface. Similarly, STM yielded atomic resolution characteristic of the original surface. This indicates that leaching occurs only in a limited depth from the surface. This is expected from the previous leaching experiments of powder samples. Their cross-sectional TEM study showed that the dissolution of Al is restricted to a certain thickness (about 0.5 μm in the given experiment) [137] because of the inhomogeneous distribution of Al inherent to the quasicrystallinity of the sample studied. The thickness of the leached area is expected to be less than 1 μm as described in Section 4.3.1.

Surface Composition

XPS spectra from the surface after leaching at different times from 1 to 8 hours are compared in Figure 4.12a-d . The spectra were taken after the surface was sputtered and thus provide information from the subsurface region of the leached surface. The core level positions of Cu and Fe are not affected by increasing the leaching time. However, there is a change in surface chemical composition. The variation in the composition deduced from the XPS spectra for different leaching times is shown in Figure 4.12e. The composition was determined using the area of the Cu 2p and Fe 2p peaks after Shirley background subtraction and using the photoemission cross section, instrumental response and inelastic mean path of photoelectrons.

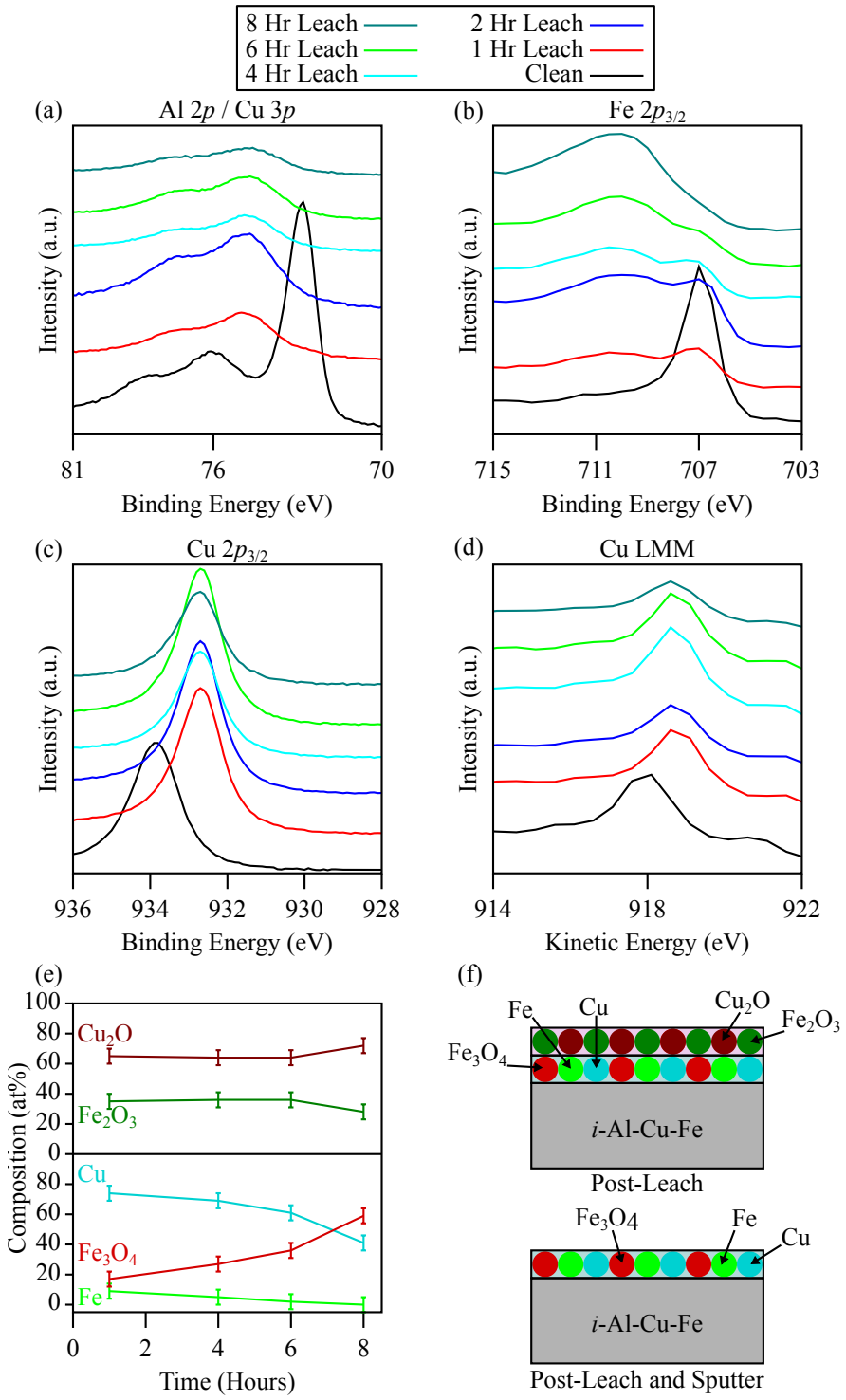

Figure 4.12: (a) Al $2p$/Cu $3p$, (b) Fe $2p$, (c) Cu $2p$, and (d) Cu LMM Auger spectra (Mg K_α source) from the five-fold i-Al-Cu-Fe surface after leaching for different times and subsequent sputtering. (e) Change in composition of the top surface layers (top) and subsurface (bottom). The composition of the subsurface was deduced from XPS spectra given in (b) and (c). (f) Illustration of the surface and subsurface composition after leaching and sputtering.

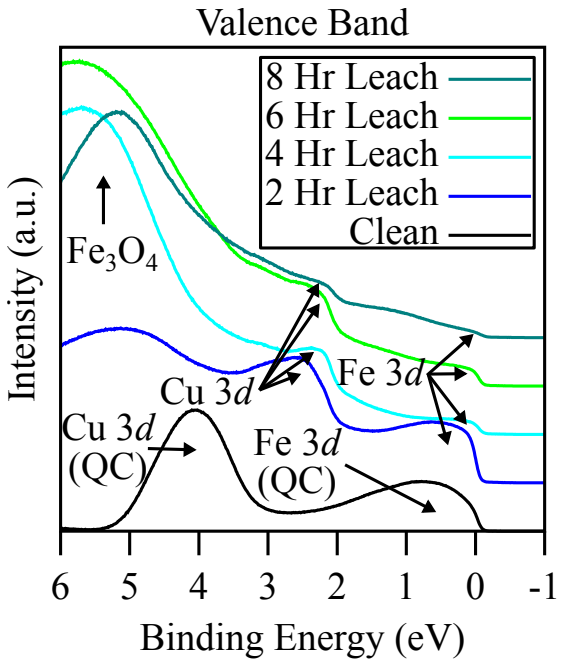

Figure 4.13: Valence band spectra of the five-fold *i*-Al-Cu-Fe surface after leaching for different times taken with He-I radiation. The angle of incidence was 45°. Cu and Fe metal 3d bands are present in the spectra following leaching but then decrease with leaching time as the oxide increases. This is in agreement with the results from XPS.

The content of Fe_3O_4 increases with leaching time, while elemental Fe and Cu decreases. After 6 hours it is no longer possible to identify Fe metal, which was possible after shorter treatments. Elemental Cu is still detectable even after 8 hours leaching. This may be because the subsurface Fe gradually oxidizes with leaching time and becomes rich in Fe_3O_4. After 8 hours of leaching the surface is predominantly Fe_3O_4.

The change in composition in the surface region was also analyzed using XPS spectra from the leached surface, i.e., without sputtering. In contrast to the subsurface region, the Cu species increases and Fe species in the surface region decreases with increasing leaching, especially after 6 hours leaching (Figure 4.12e, top). The influence of leaching time has not been systematically studied on the powder samples. However, the powder sample leached by 5 mol concentration of NaOH for 12 hours exhibited the Cu species [131, 134] and there are no reports of identification of elemental Fe.

4.3.5 Effect of Leaching on the Valence Band

UPS measurements were performed from the surface after leaching for different times and subsequently sputtering in UHV (Figure 4.13). The valence band spectrum from the clean quasicrystal surface shows two peaks corresponding to

the Cu $3d$ band (at about 4 eV) and the Fe $3d$ band near to the Fermi level [157]. After leaching for 2 hours, three peaks appeared in the valence band. The peak at about 5 eV is attributed to Fe_3O_4 [158], the peak at around 2.5 eV to elemental Cu [159] and the peak near to the Fermi level to elemental Fe [158]. With increasing leaching time, the spectra demonstrate the increase in the Fe_3O_4 intensity and the gradual removal of elemental Cu and Fe peaks, in agreement with the XPS results discussed above.

4.4 Summary

The use of quasicrystals as precursors to catalysts for the steam reforming of methanol is potentially one of the most important applications of these new materials. To develop the application as a technology requires a detailed understanding of the microscopic behaviour of the catalyst. This chapter contains a study of the effect of leaching treatments on the surface microstructure, chemical composition and valence band of the icosahedral i-Al-Cu-Fe quasicrystal in an attempt to prepare a model catalyst. The high symmetry five-fold surface of a single grain i-Al–Cu–Fe quasicrystal was leached with NaOH solution for varying times and the resulting surface was characterized by x-ray photoelectron spectroscopy (XPS), ultraviolet photoelectron spectroscopy (UPS), scanning electron microscopy (SEM) and atomic force microscopy (AFM). The leaching treatments preferentially remove Al producing a capping layer consisting of Fe and Cu oxides. The subsurface layer contains elemental Fe and Cu in addition to the oxides. The quasicrystalline bulk structure beneath remains unchanged. The subsurface gradually becomes Fe_3O_4 rich with increasing leaching time. The surface after leaching exhibits micron sized dodecahedral cavities due to preferential leaching along the five-fold axis. Nanoparticles of the transition metals and their oxides are precipitated on the surface after leaching. The size of the nanoparticles is estimated by high resolution transmission microscopy (TEM) to be 5-20 nm, which is in agreement with the AFM results. Selected area electron diffraction (SAED) confirms the crystalline nature of the nanoparticles. SAED further reveals the formation of an interface between the high atomic density lattice planes of nanoparticles and the quasicrystal. This may be one of the factors responsible for the higher activity and improved thermal stability over currently used crystalline catalysts.

Chapter 5

Effect of Aperiodicity on Leaching Susceptibility

5.1 Introduction

It was found that samples of similar stoichiometry but different structural ordering exhibited different leaching rates that could be attributed to their crystal structure, crystalline materials being the most aggressively leached, while the quasicrystalline materials were the most resistant [137]. A result that suggested this was part of a trend rather than a single outcome was the finding that the quasicrystal approximants displayed a leaching resistance greater than crystalline samples but less than quasicrystal samples [135]. Quasicrystal approximants share a similar local atomic structure to quasicrystals, but large 'clusters' of quasicrystalline atoms are arranged periodically within the crystal. Despite previous work, there is to date no clear understanding of the interaction between the quasicrystalline bulk and the leached layer [134].

In Chapter 4, it has been shown that leaching of the five-fold surface of the icosahedral-Al-Cu-Fe produced five-fold facets upon the surface [90]. On the leached crystal there were places where pentagonal and pentagonal-dodecahedral cavities were found on macroscopic surface orientations that were no longer well-aligned exclusively to the original five-fold surface. Similar results have previously been observed during oxidation studies on the Al-Pd-Mn family quasicrystals where aggressive treatments unearthed other 'internal' surface orientations [145, 147]. The pentagonal-dodecahedral cavities also demonstrated the leaching of other five-fold surfaces at angles of 108°. This led to an initial conclusion that the five-fold crystallographic direction was preferred to the others, regardless of which macroscopic surface was exposed to the leaching solution, leading to a hypothesis that crystallographic direction, not macroscopic orientation dictated

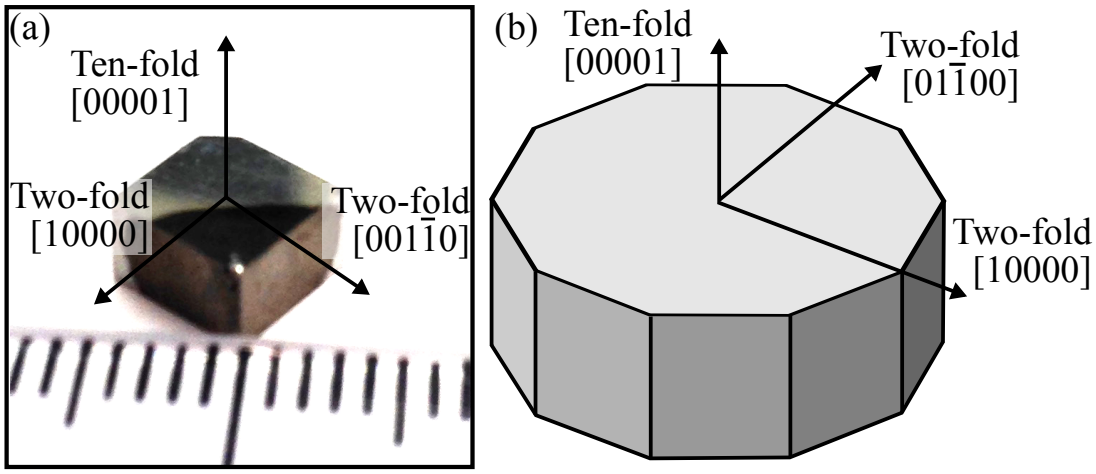

Figure 5.1: (a) Crystal as-grown,polished and leached. The dark area of crystal displays the area leached in NaOH (b) Schematic of the surfaces on a decagonal rod.

leaching kinetics in these materials.

In a bid to test this hypothesis directly, a single crystal decagonal Al-Ni-Co quasicrystal with 3 well orientated surfaces present on the sample was used. Decagonal quasicrystals are characterised by the periodic stacking of quasicrystalline planes [144]. The high symmetry axes of these systems includes a unique ten-fold axis along the periodic direction and two nonequivalent two-fold axes. These two-fold planes appear alternately at 18° to each other and perpendicular to the ten-fold axis. The two-fold planes therefore contain both the periodic and quasiperiodic direction. This allows a direct comparison of the leaching kinetics. An additional advantage over the previously studied powdered samples is the 'simplified' nature of the single crystal surfaces. This section will outline the experiments undertaken to compare the leaching characteristics of 3 surfaces on the d-Al-Ni-Co quasicrystal, two crystalline surfaces (0 0 0 0 1) and (0 1 $\bar{1}$ 0 0), and the 2D quasicrystalline plane (1 0 0 0 0). SEM and EDX were used to investigate both chemical and structural effects of the leaching treatment.

5.2 Experimental Methods

A decagonal Al-Ni-Co quasicrystal was cast into a cuboid with polished (0 0 0 0 1), (1 0 0 0 0) and (0 1 $\bar{1}$ 0 0) surfaces, see Figure (5.1). Figure 5.1a shows the sample 'as-grown' with labelled surfaces, while Figure 5.1b shows the relationship of the surface orientations on the sample with those in the decagonal structure of the crystal.

The surfaces were mechanically polished using diamond paste with diameter

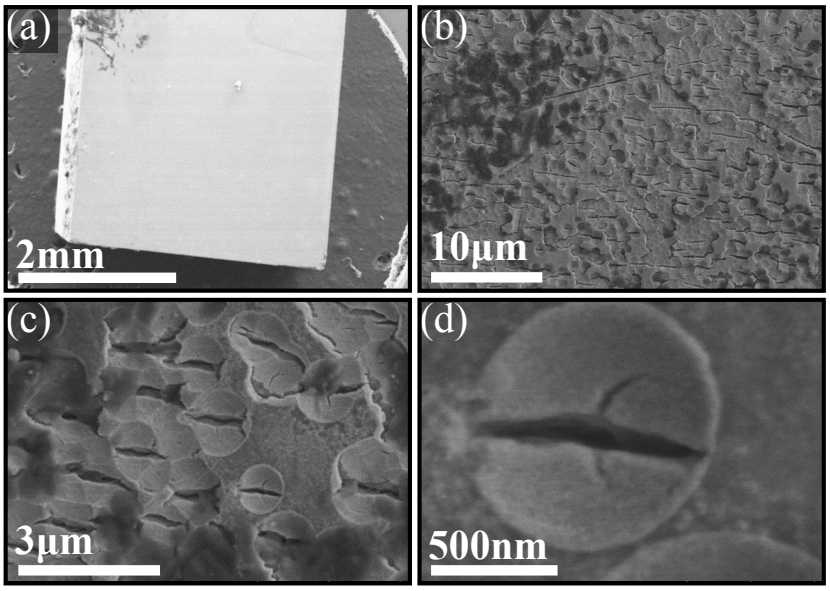

Figure 5.2: SEM images of the (1 0 0 0 0) surface following leaching. (a) Wide zoom of the surface (b) Characteristic roughness of the surface observed (c) Features of the roughness (d) Example of repeating facet on the surface. There is a suggestion in the images that the cracks inside the depressions share an orientation. While the twofold symmetric nature of the surface would suggest this possibility, it was not possible to confirm this feature with any statistical method.

5 - 0.25 µm. The crystal was then suspended in 5 mol conc. NaOH solution and leached for 5 minutes in ambient conditions as described in section 2.1.3. The crystal was then analysed using SEM, EDX, AFM and STM. The SEM/EDX studies were carried out using a Hitachi S-4800 Field-Emission Scanning Electron Microscope combined with an Oxford Instruments Inca Energy EDX Detector at the University of Liverpool's Centre for Materials Discovery.

5.3 Results

5.3.1 The two-fold (1 0 0 0 0) Surface

Figure (5.2) shows a summary of the SEM data for the (1 0 0 0 0) two-fold surface. The surface is characterised mostly as very flat, with a slight puckering of the surface, which can be seen in Figure 5.2b. This can be attributed in places to the presence of many small circular depressions often with at least a single crack forming through the middle. These can be seen in detail in figures 5.2c and 5.2d. The symmetry of these features is different from the surface symmetry, indicating that any order present from the two-fold surface has been lost. As is common in previous Al-based quasicrystal leaching experiments, the surface is coated in a homogenous precipitate particle layer of transition metal as confirmed by EDX

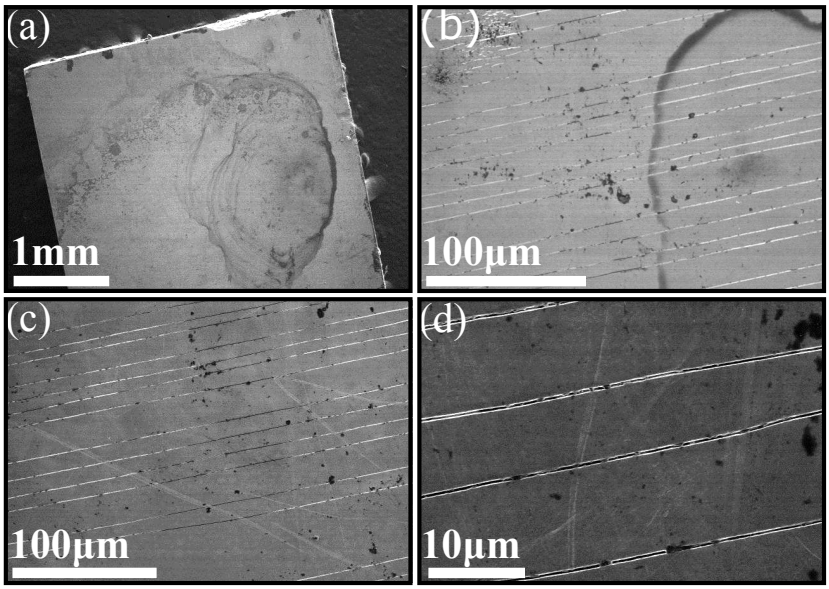

Figure 5.3: Surface of the leached $(0\,1\,\bar{1}\,0\,0)$ surface (a) Wide zoom of leached surface (b) Lines aligned perpendicular to the $(0\,0\,0\,0\,1)$ ten-fold surface (c) Similar lines and line separations from a distant part of the crystal can be directly compared with that in (b). (d) The spacing of the lines shows commonalities in places.

analysis (section 5.3.5).

5.3.2 The two-fold $(0\,1\,\bar{1}\,0\,0)$ Surface

With minimum zoom using the SEM the dramatic effect of leaching can be seen in the surface (Figure (5.3)). Surprisingly, compared to the previous two-fold surface, there is the creation of ordered rows of leached grooves that stretch for long distances across the crystal and examples from two different parts of the surface can be seen in figures 5.3b and 5.3d. These lines are almost parallel, often with slight convergence around areas of leached cavities or at the edges of the crystal. Most lines are separated either by 6 µm or 12 µm ($\pm$ 0.3 µm).

The lines are distinct from those caused by polishing by their near parallel nature, scale and by the observance of polishing grooves crossing the leached lines. What makes these straight grooves of even more note is their orientation with respect to the rest of the crystal. The clean, two-fold $(1\,2\,1\,1\,0)$ (equivalent to $(0\,1\,\bar{1}\,0\,0)$) surface has been shown to be made up of a columnar structure orientated along the ten-fold direction [160]. The columns are up to a few microns long and display abrupt terminations revealing the $(0\,0\,0\,0\,1)$ surface. The grooves observed after leaching are perpendicular to all the ten-fold planes stacked in the crystal structure and are similarly aligned to the columnar structure of the two-fold surface. They are not of similar scale, with the leached grooves being several

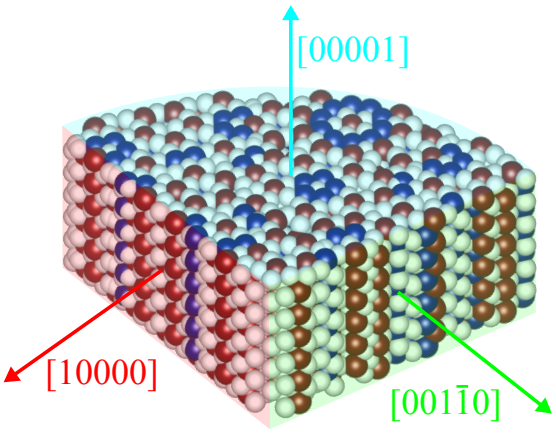

Figure 5.4: Atomic structure of *d*-Al-Ni-Co QC demonstrating the 2D quasicrystalline [00001] surface periodically stacked to form two unique two-fold surfaces.

hundred microns in length. It suggests that it is the presence of the columnar structure and their associated terminations, provides access to the periodic stacking, thus causing the formation of these leached grooves.

A question that arises from this observation is why these well oriented features are observed on one two-fold surface and no other. In the *d*-Al-Ni-Co structure, there are only two unique two-fold surfaces. One appears at the edge of the decagonal structure (equivalent to (1 0 0 0 0)) as shown in Figure 5.1b, while the other is formed at the corner of this structure. The surface formed from the corners (equivalent to (0 1 $\bar{1}$ 0 0)) is unstable and has been shown to facet heavily to form the more stable {1 0 0 0 0} surfaces. The atomic structure of the *d*-Al-Ni-Co crystal is shown in Figure 5.4. It is suggested that this faceting or reduced stability leads to the difference in surface features following leaching. Observing the structure of the (1 0 0 0 0) surface, it appears closer packed and less open than the (0 1 $\bar{1}$ 0 0) surface. This faceted and open nature may increase the access to the periodic direction parallel to the surface.

5.3.3 The ten-fold (0 0 0 0 1) Surface

The leached surface of (0 0 0 0 1) orientation can be seen, even optically, to be more aggressively leached than the other surfaces previously mentioned. The surface is very dark, much darker than the other two surfaces. This was different to previous experiments with *i*-Al-Cu-Fe where similar results would require several hours of leaching. This indicates a preference for leaching along the ten-fold direction, and when considered with previous results, a preference for leaching along the periodic direction. In comparison the greatly increased leaching resistance of the *i*-Al-Cu-Fe system can be considered to be due to the icosahedral struc-

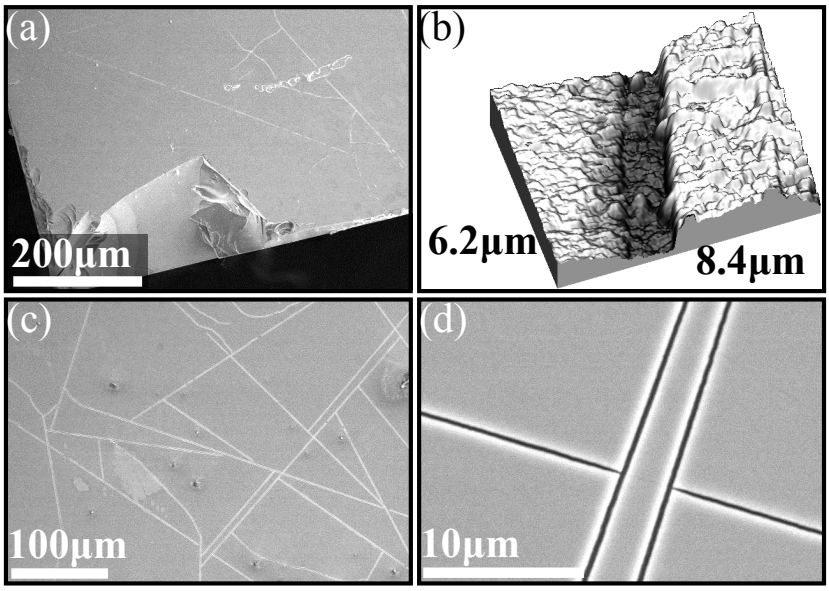

Figure 5.5: (a) SEM image at wide zoom of the (0 0 0 0 1) surface (b) AFM image of etched grooves present on surface (c) SEM image of the grooves produced across a large area with apparent ordered structure but no symmetry could be observed (d) Small scale image of connecting grooves

ture, which provides quasiperiodic ordering in all directions, as opposed to the decagonal structure, which has periodic directions. The surface remains mostly flat apart from the presence of similar troughs to the $(0\,1\,\bar{1}\,0\,0)$ surface, although these are far less regularly patterned (Figure (5.5)). Figure 5.5c shows an example of using AFM to identify the depth of these grooves to be of the order of ∼100nm and to be largely unchanged in depth at other points across the surface. The unusual patterns on the surface displayed in Figure 5.5c, and their inconsistency with the other planes may be attributed to the quasiperiodic nature of the surface, although no aperiodic order could be identified. It was not possible to identify any orientation between the grooves leached into the surface and any defined crystallographic direction.

5.3.4 Measuring the Depth of the Leached Region

In an attempt to better understand the leaching depth, an STM was used in a non-standard approach. By bringing the tip close enough to the surface to observe a tunnelling current, retracting the tip a set number of course steps, moving across the sample laterally then repeating, it was hoped that a profile of the surface could be built up. The ideal situation for this and the schematic are shown in Figure 5.6a.

This technique was unsuccessful in observing any change as there was a con-

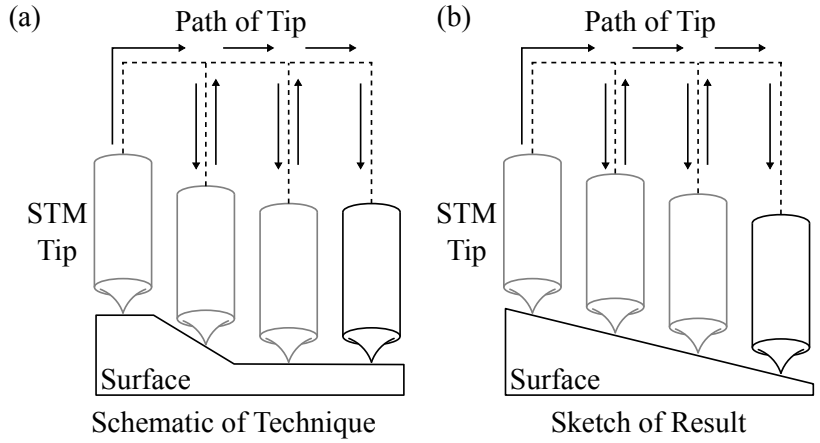

Figure 5.6: (a) Outline of method using STM to investigate leaching depth of the crystal. (b) The result was inconclusive as any change in crystal height were obscured by slope or smaller than course step of STM piezo motors.

stant trend in the height profile as shown in Figure 5.6b. This however, provides two possible explanations. Firstly, the height change is less than the size of one of the course steps of the STM piezo motor, approximately 400 nm. Secondly, through observing the AFM images of the leached surface, and acknowledging their porosity, it could be the case that the STM tip tunnels into the highest points, which are not changed dramatically from the clean surface, but the leached region descends much further into the crystal.

5.3.5 EDX Composition

EDX has an information depth of several microns. The leach depth is not on the same scale, based on previous single crystal leaching work using XPS on *i*-Al-Cu-Fe and attempted use of STM described above. Therefore it is possible that the variation in leaching stability, from a chemical analysis technique, will not be visible with such a large proportion of the signal originating from the bulk. For this reason EDX was used as a means to indicate changes in leach depth. From experiments using XPS in section (4.3.3) the surface is expected to be Al free for at least the information depth of XPS (several atomic layers) assuming similar leaching to Al-Cu-Fe, and any Al signal in EDX must come from the bulk. Therefore variation in this signal may indicate the change in depth of the leached layer. This was attempted by taking EDX spectra at points across each surface of the crystal, starting in the unleached regions, and moving through the leaching boundary and the fully leached area.

All the surfaces appear similarly chemically changed following leaching treatment as measured using EDX. This appears to suggest uniform leaching of all

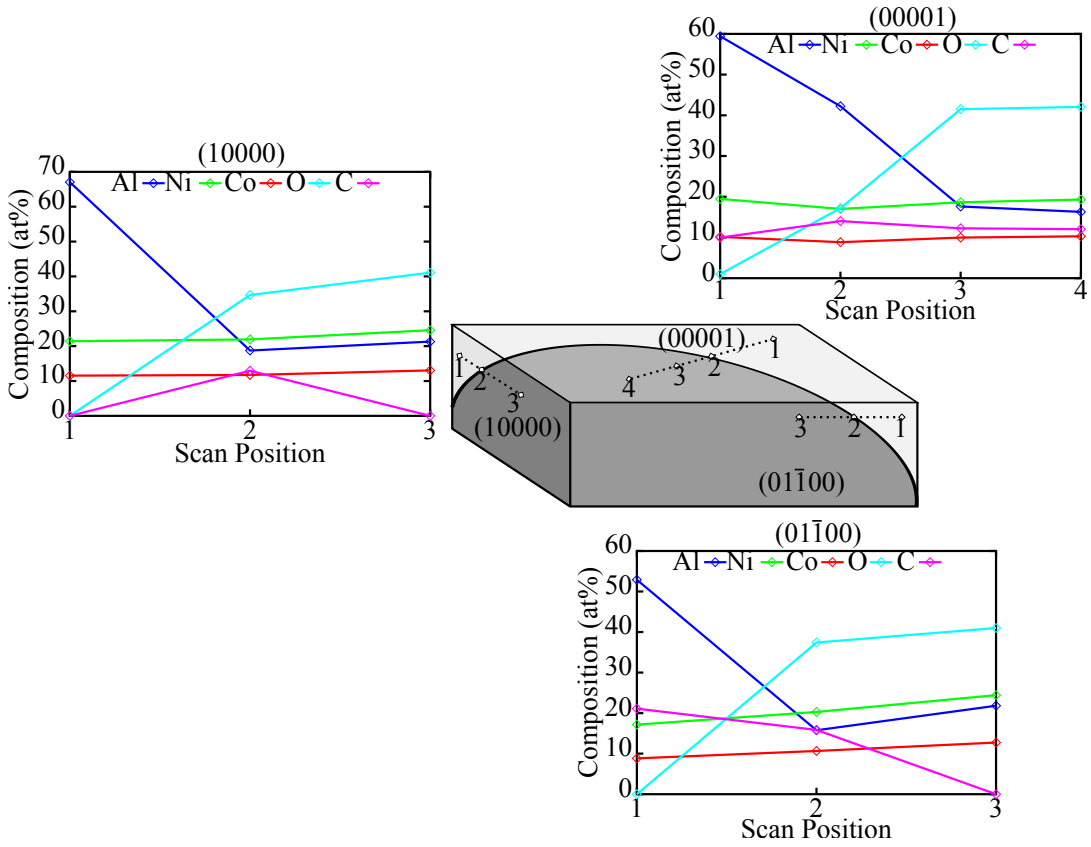

Figure 5.7: Comparison of chemical composition (atomic%) variation across leaching boundaries, or transition regions, on all three Al-Ni-Co surfaces (0 0 0 0 1), (1 0 0 0 0) and (0 1 $\bar{1}$ 0 0). Numbers represent points across the surface at which spectra were taken. The dark gray area represents the leached area of the crystal. Transitions were more sudden in the two-fold surfaces and gradual in the ten-fold surface.

surfaces. However, the low surface sensitivity of the technique means that small variations in response to leaching would not be recognised. The EDX results show a reduction in Al in all observed surfaces, as would be expected based upon previous work. Coupled with this is the observed increase in transition metals and oxygen. The increase in oxygen is attributed largely, but not exclusively, to the Co and Ni oxide species which are formed during leaching. EDX is not capable of determining oxide species in the manner of other spectroscopic techniques such as XPS. Figure (5.7) shows that there is a consistent increase in Co and Ni on all three surfaces. The ratio of Co to Ni remains approximately constant during this treatment, indicating there is no preferential selection of either during the leaching process.

There is a difference in the chemical characteristics of the leaching boundary between the two-fold surfaces and the ten-fold surface. In the two-fold surfaces, the Al content changes dramatically upon entering the leaching boundary and then changes very little even once totally inside the leached region. This can be seen on both $(1\,0\,0\,0\,0)$ and $(0\,1\,\bar{1}\,0\,0)$ surfaces in Figure 5.7, where the Al content decreases from point 1 to point 2. The sharp transition region in the crystal is related to proposed leaching resistance perpendicular to the surface and parallel to the surface in the opposite two-fold direction. These are the two directions which contain aperiodic ordering. In the periodic direction the leaching resistance is much lower leading to a reduced leach depth, which can be inferred from an observed lower Al signal in the two-fold surfaces compared to the ten-fold surface.

In the ten-fold surface, the Al content changes steadily across the leaching boundary and into the entirely leached region. This leaching boundary is difficult to distinguish in the ten-fold surface using SEM, whereas in the two-fold surfaces it was a clear band running across the crystal. This indicates a continuous increase in leach depth across the crystal. This is interpreted to be due to an increased leaching speed along the ten-fold direction. The leaching is still present along the other directions but the speed of this is reduced leading to the continuous slope and a poorly defined leaching boundary. A summary of these observations is shown in Figure 5.8.

5.4 Summary

Three orientated surfaces of a decagonal Al-Ni-Co quasicrystal were leached in NaOH and then studied using SEM and EDX. Both two-fold surfaces were found to be less aggressively leached than the quasiperiodic ten-fold surface. Leached microstructure indicates preferential leaching along the periodic directions, again indicating that crystallographic direction rather than macroscopic surface orien-

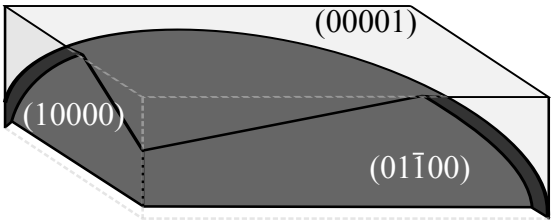

Figure 5.8: Summary of changes due to leaching of the crystal, effects exaggerated for visibility. The top surface displays a sloping surface due to the leaching while the two-fold surfaces contain a much sharper transition region.

tation is the key influence on leaching kinetics of quasicrystals. This gives further weight to the idea that the quasiperiodic arrangement of Al in the crystal inhibits alkali leaching. These results provide an important insight into the preparation of model catalysts of nanoparticles for steam reforming of methanol.

Chapter 6

Molecular Adsorption Site Specificity in Icosahedral Quasicrystals

6.1 Introduction

In Chapters 4 and 5, the effect of aperiodic order on the stability of a catalytically active nanoparticulate overlayer was studied. While it was found that the nanoparticles did not adopt quasiperiodic order in the leached *i*-Al-Cu-Fe and *d*-Al-Ni-Co systems, the effect of the quasicrystalline ordering was indirectly evident in catalytic studies. The leached surfaces of these crystals were not suitable for STM studies of the molecule due to significant roughness but it was decided to use the clean quasicrystal surfaces to investigate site selectivity. *i*-Al-Cu-Fe has been shown to have catalytic properties prior to leaching for methanol decomposition reactions [53].

Site selectivity is an important factor determining catalytic behaviour. A single active site must maintain enough separation to allow for the adsorption of molecules on as many active sites as possible to maintain activity.

Additionally a large drive of current research into aperiodic systems is the application of quasiperiodic ordering to molecular and metallic thin films through epitaxial growth. If molecules can be ordered in a quasiperiodic lattice, this would create the opportunity to manufacture materials that could share the unique set of properties associated with quasicrystals (see section 4.1) or have entirely different properties to their crystalline form.

Materials could also be constructed with tuned optical properties such as photonic materials. The icosahedral structure provides the closest approximation of a fully isotropic first Brillouin zone, and therefore a complete photonic band gap

[161]. Magnetic molecules could also be confined to quasiperiodic arrangements to explore the effect of magnetic frustration in quasicrystalline systems [162]. Previous attempts to construct molecular quasicrystalline material have been unsuccessful [163–166].

In this study, C_{60} (Buckminsterfullerene) was deposited on the five-fold surface of an *i*-Al-Cu-Fe quasicrystal. C_{60} has long been used as an adsorption test molecule due to its large size and isotropic shape. This makes it easy to see and understand in microscopic measurements. In order to examine the adsorption properties of surfaces aligned to other symmetry axis such as the three-fold and two-fold surfaces a *i*-Ag-In-Yb QC was used. The *i*-Al-Cu-Fe QC does not form two-fold and three-fold surfaces which are suitable for UHV studies with STM. These surfaces only form very small atomically flat terraces and are sometimes heavily faceted. The *i*-Ag-In-Yb QC is structurally similar to *i*-Al-Cu-Fe and readily forms large atomic terraces on both the three-fold and two-fold surfaces. These crystals were used to investigate the effect of the surface rotational symmetry on the adsorption site properties. It has been found that the C_{60} molecules (Figure 6.1) will form long range quasicrystalline networks with specific, well defined adsorption sites on the five-fold *i*-Al-Cu-Fe QC but not on either the three-fold or two-fold surfaces of *i*-Ag-In-Yb. In previous work similar experiments were performed on the five-fold surface of *i*-Ag-In-Yb, and there was no observed molecular ordering of the adsorbate [167]. There was evidence of two distinct adsorbed molecular heights indicating some adsorption site preference, although this was not fully described, and the system did not display a specifically decorated quasiperiodic adsorption lattice.

6.2 Experimental Methods

The five-fold surface of an *i*-Al-Cu-Fe quasicrystal, the three-fold surface of an *i*-Ag-In-Yb quasicrystal and the two-fold surface of an *i*-Ag-In-Yb quasicrystal were polished mechanically with diamond paste of successively finer grades (6

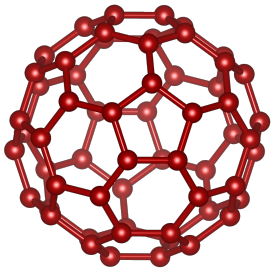

Figure 6.1: Atomic structure of C_{60} Buckminsterfullerene.

μm - 0.25 μm), before being cleaned in methanol in an ultrasonic bath. The crystal was then placed in UHV (10^{-10} mbar) and prepared through cycles of ion bombardment and annealing (as described in Section 2.1.2). The sample was sputtered with 2 keV Ar^+ ions for 45 minutes. The *i*-Al-Cu-Fe QC was annealed at 973 K for 3 hours, while the *i*-Ag-In-Yb QCs were annealed at 713 K for 4 hours.

C_{60} was evaporated from a home-made source as described in Section 2.1.2. The evaporator was heated to 500 K during evaporation and was positioned roughly 10 cm from the surfaces. During evaporation the *i*-Al-Cu-Fe QC sample was held between 773 K and 973 K. C_{60} was deposited on *i*-Ag-In-Yb QCs at room temperature and between 573 K and 673 K. Sample temperature was measured with an optical pyrometer, set to measure at an emissivity of 0.35. This was used to calibrate a K-type thermocouple to measure the temperature of the sample during deposition, when reflected light from the evaporator interfered with the pyrometer's operation.

The images were taken using an Omicron VT-STM at room temperature, once the crystal was allowed sufficient time to cool to room temperature.

6.3 Results and Discussion

6.3.1 C_{60} on the five-fold surface of *i*-Al-Cu-Fe

In order to understand the adsorption properties of the C_{60}, it was first necessary to take images of the clean surface. A scan of the clean surface can be seen in Figure 6.2a. Both the auto-correlation function and the fast Fourier transform of the STM image clearly confirm the five-fold rotational symmetry of the surface.

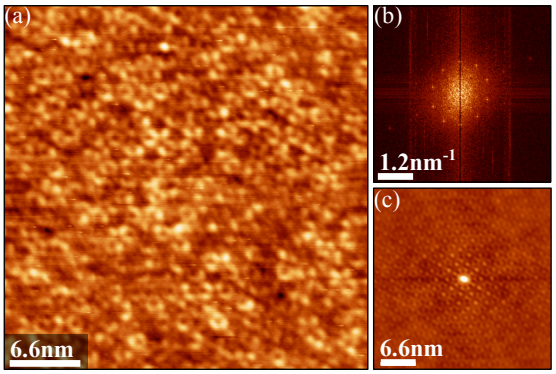

Figure 6.2: (a) STM image of the clean five-fold surface of *i*-Al-Cu-Fe showing the five-fold symmetrical nature of the atomic structure as confirmed by a (b) 2D fast Fourier transform (FFT) of the image and a (c) 2D auto-correlated pattern of the image in (a).

Closer inspection of this clean surface allows comparison to the calculated bulk truncated structure used in this study. The model used is from Yamamoto *et al.* [168], which itself is a refinement of previous models [169]. The model is of the quasicrystal *i*-Al-Pd-Mn, which is isostructural to *i*-Al-Cu-Fe with Pd and Mn replaced by Cu and Fe respectively. A comparison of the image with the model is shown in Figure 6.3. Although the structure is not repeating, clearly recognizable motifs across the surface are visible and can be reproduced in the model.

The clean surface was then exposed to C_{60}, the results of which can be seen in figures 6.4 and 6.5. In these images, it was not possible to obtain high resolution of the substrate, so the substrate has been darkened to improve visibility of the molecules. Images have been plane corrected and manually contrast adjusted but no further corrections have been made.

When attempting to demonstrate the symmetry of the C_{60}/Al-Cu-Fe surface, rather than including symmetry from the substrate, the positions of the molecules were analysed. This can be seen in the figures as the dot-map to the right of the STM image. When observing the auto-correlation of this position map, a clear five-fold symmetry is present. The FFT of these images and position maps is, in general inconclusive, due to the small sample size of points and the variation of C_{60} molecule size.

From these images it was possible to discern two distinct adsorption heights with a difference of 1.4 Å. The higher of the two will be referred to as the bright (B) molecules while the lower will be referred to as the dim (D) molecules. In the above figures (Figures 6.4 and 6.5) the positions of the B molecules were used

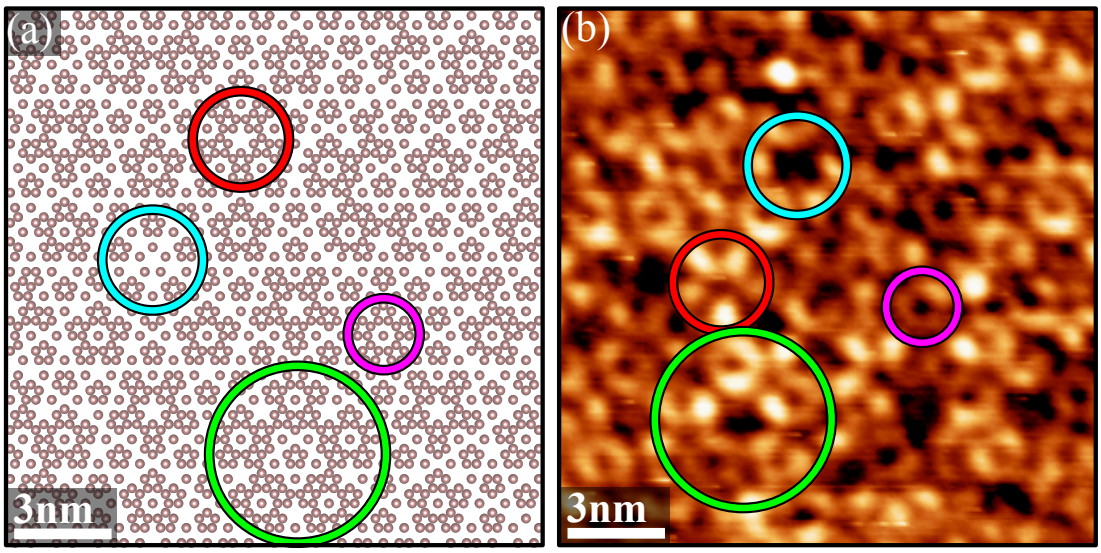

Figure 6.3: Comparison of the (a) model surface with an (b) STM image. Characteristic motifs identified by Sharma *et al,* are observed in the prepared surface and identifiable by the coloured rings. [170].

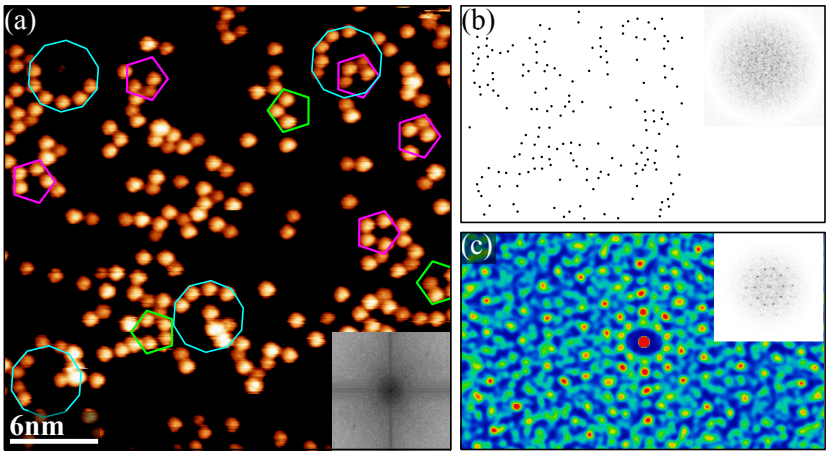

Figure 6.4: (a) Low coverage C_{60} deposited on *i*-Al-Cu-Fe. Substrate has been removed and common features relating to quasicrystalline order highlighted with FFT (inset). (b) Adsorption position map with FFT (inset). (c) Autocorrelation of adsorption map with ten-fold symmetry and associated FFT (inset).

to create the position maps which demonstrate the pentagonal pattern of the adsorption sites.

A key measurement of a quasicrystalline lattice is the nearest neighbour distance. This is most easily observed as the smallest edge length a of pentagonal tiling across the features of the surface. Larger tilings that connect larger motifs of the surface can then be described by the formula $a \cdot \tau^n$, where τ (=1.618...) is the golden ratio and n is a positive integer.

At this coverage the B molecules occupy a pentagonal lattice with lattice site separation $a = 1.2 \pm 0.1$ nm. This separation is consistent with the separation of pentagonal arrangements of surface Fe atoms. There are no Cu atoms in the surface layer and the Al atoms are too densely packed to provide this lattice

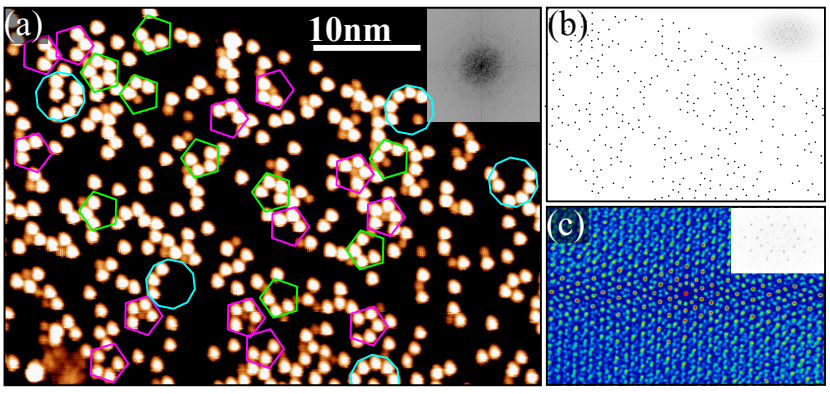

Figure 6.5: (a) High coverage C_{60} deposited on *i*-Al-Cu-Fe. Substrate has been removed and common features relating to quasicrystalline order highlighted with FFT (inset). (b) Adsorption position map with FFT (inset). (c) Autocorrelation of adsorption map with ten-fold symmetry and associated FFT (inset).

separation. The Fe atoms are too close together for all to be decorated ($a_{Fe} = a \cdot \tau^{-1} = 0.74$ nm, C_{60} van der Waals diameter = 1.0 nm), but provide a network of sparse nucleation sites which can explain all of the observed features of the B molecule lattice. A comparison can be seen in Figure 6.6. This will be discussed in greater detail subsequently.

It is a relatively well-developed idea that the adsorption sites for quasicrystals are dependent on the least abundant element in ordered ad-layers. This has previously been observed with Pb, Si and Bi on Al-Pd-Mn, where the network has depended on the positions of Mn atoms in the surface layer [166, 171, 172]. There has also been evidence of preferred adsorption sites atop subsurface minority element positions [163].

The D molecules are positioned on a different lattice where $a_D = \tau \cdot a$. These sites are often found at the centre of incomplete pentagons of B molecules, while their height is 1.4 Å lower than the B molecules. These molecules fit on a lattice that matches the position of subsurface Fe atoms from the next layer down but not with any surface Fe atoms. This supports the idea that it is the positions of Fe atoms in the uppermost layers of the quasicrystal that determine adsorption sites of the C_{60}. Cu and Al are too densely packed to influence the molecular ordering, due to the presence of too many competing sites. In the case of both Cu and Al it would be impossible for a C_{60} molecule to be centered on one specific atom without also decorating a neighbour atom. This level of degeneracy would cause disordered adlayers.

For the subsurface Fe atoms to be decorated, top layer Al atoms must be displaced leading to the conclusion that in the presence of C_{60} at high temperature

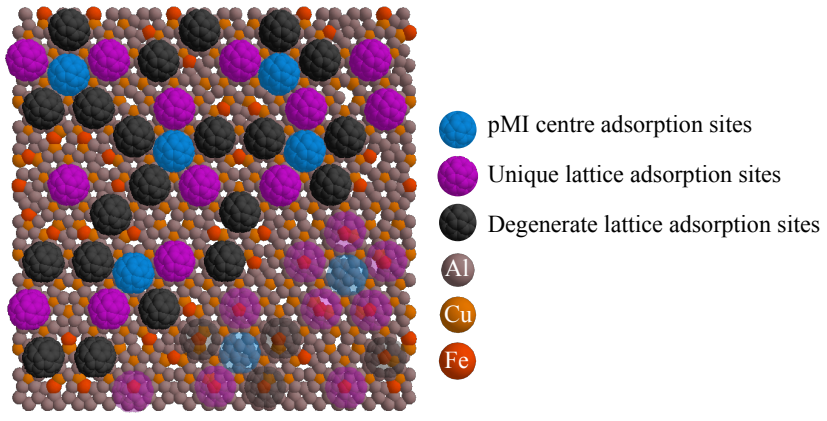

Figure 6.6: Model adsorption sites of C_{60} on Al-Cu-Fe. Blue molecules represent molecules adsorbed on subsurface Fe molecules at pMI centres, magenta molecules are adsorbed on surface Fe atoms which create a unique lattice where all positions can be occupied and black molecules are adsorbed at Fe sites which degenerate. Bottom right-hand corner transparency displays Fe adsorption site.

there must be some small surface reconstruction. The second layer in the model is separated from the first by 0.21 nm, significantly more than the difference in C_{60} height. Dynamical LEED studies by Cai *et al.* [173], showed that surface relaxation served to separate the layers rather than bring them together, ruling out the possibility of a high temperature induced surface relaxation. It is therefore possible to suggest that the apparent height difference of the molecules is related to electronic effects or differences in the bonding environment rather than a surface relaxation.

Interestingly, this film demonstrates the coexistence of several exclusive competing adsorption sites or quasi-degeneracy. Quasi-degeneracy is defined as the existence of many states of similar energy. Upon periodic substrate surfaces, molecules may diffuse to form long-range ordering, stick where they land to form disordered layers or undergo some other surface interaction. Molecules capable of adopting several relative orientations with comparable energies produce quasi-degenerate layers based on well defined-lattices [174, 175].

C_{60}/Al-Cu-Fe is the first system observed in which molecules only adsorb on one subset of the points on the available unique lattice. This is due to the relationship between the characteristic length scale of the adsorption site lattice and the size of the C_{60} molecules. The lattice length scale is large enough that it can directly affect the adsorption characteristics, in that adsorption sites are sufficiently spaced to allow distinctive adsorption. This distance is also small enough such that not all sites can be decorated.

Within this framework it is noticeable that there is a lattice of adsorption sites which are non-degenerate and can all be decorated at once. These molecules, coloured magenta in Figure 6.6, represent these sites. There are no adsorption sites close enough to the ones decorated with magenta molecules to inhibit their decoration. This is the case when the site separation is $a' = \tau \cdot a = 1.9\,(\pm 0.4)$ nm.

The blue C_{60} molecules represent the adsorption sites of the molecules that sit atop subsurface Fe atoms at pseudo-Mackay icosahedra (pMI) centres. The structure of *i*-Al-Cu-Fe is constructed from pMIs. These structures are made up of a Fe atom at the core, surrounded by a first shell of Al atoms, followed by an icosahedron of Al/Cu, completed by an outer icosidodecahedron consisting of Al/Cu or Al only. This can be seen in Figure 6.7. The inner shell of Al atoms is drawn as a cube with atoms at the vertices, this is for diagrammatic purposes only and the literature suggests a range of shapes that are possible.

The lattice resultant from the subsurface Fe is inverted compared to the surface Fe. The mechanism that determines which subsurface Fe is exposed to adsorbed C_{60} molecules at elevated temperature may be based on whether the Fe

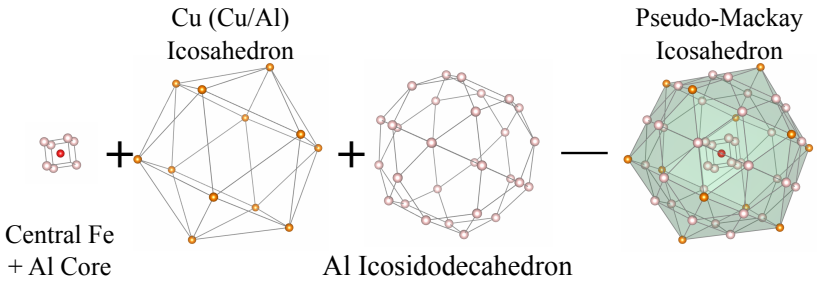

Figure 6.7: Components of the Pseudo-Mackay Icosahedron, a key building block in the *i*-Al-Cu-Fe structure. Elemental make up of the second icosahedron can vary with an Al/Cu mix. Al core arbitrarily plotted on corners of cube.

atom is at the centre of a pMI. These Fe will only have Al nearest neighbours and the clusters have a separation consistent with the data. Cluster centre nucleation sites is consistent with studies on the isostructural *i*-Al-Pd-Mn[166, 171].

6.3.2 C_{60} on the three-fold surface of *i*-Ag-In-Yb

Following the observation of templated molecular ordering of C_{60} on the five-fold surface, it was attempted to apply quasiperiodic ordering to the same molecules using other rotational symmetry surfaces. It is not possible to prepare three-fold or two-fold surfaces of *i*-Al-Cu-Fe which are suitable for UHV studies using STM, but this is possible with quasicrystalline Ag-In-Yb. Ag-In-Yb is made up of Tsai-type clusters, shown in Figure 6.8. Tsai type clusters were introduced to describe the atomic structure of *i*-Cd-Yb quasicrystals and their approximants, *i*-Cd-Yb is isostructural to *i*-Ag-In-Yb. In the structure of the shells Cd is replaced with equal parts Ag and In. This is made up of an inner tetrahedron of 4 Cd (Ag/In) atoms, surrounded by a dodecahedron of 20 Cd (Ag/In) atoms. This is then contained within an icosahedron of 12 Yb atoms. The final two shells are an icosidodecahedron of 30 Cd (Ag/In) atoms and a rhombic tricontahedron (RTH) of 92 Cd (Ag/In) atoms. [177].

After preparation of the crystal as described in section 6.2, the clean three-fold surface of the *i*-Ag-In-Yb QC was observed using STM (Figure 6.9). Features found in previous studies can be seen as compared to the model [178].

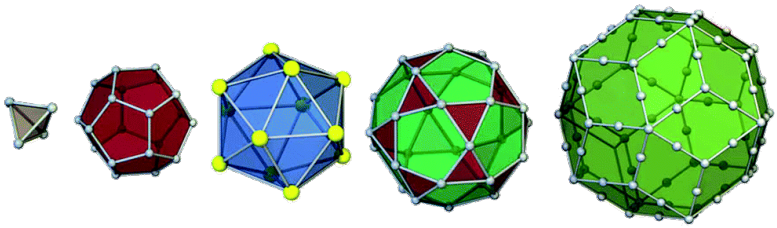

Figure 6.8: Building blocks of a Tsai-type cluster in *i*-Cd-Yb. Modified from [176]

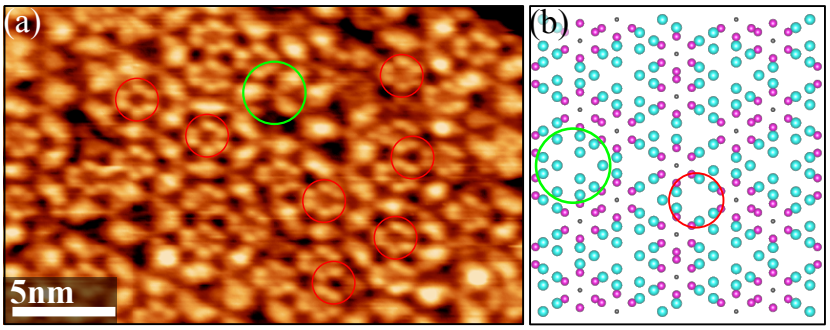

Figure 6.9: (a) Clean surface of the three-fold *i*-Ag-In-Yb QC, (b) Model with comparable motifs, blue atoms are Yb and pink atoms are Cd (Ag/In).

Following observation of the clean surface C_{60} was deposited at low coverage and at room temperature. This produced a layer that did not show any obvious long-range ordering. Analysis of the FFT and auto-correlation patterns were used to isolate the molecules from the substrate during analysis. The resolution of the substrate was markedly poorer following deposition although some three-fold features are present. A representative image of the low coverage experiments can be seen in Figure 6.10 and 6.11.

As can be seen from the low coverage data, there is no preferred site and the molecule positions do not display any certain symmetry. This may be due to a strong interaction with the substrate causing significantly reduced mobility of molecules. This would cause the molecules to adsorb where they land, which would not be surprising at room temperature. The experiment was repeated with higher coverage as shown in Figure 6.12. This also showed similar properties to the low coverage. It was determined that there were no preferential adsorption sites on the surface. The different adsorption sites identified through specific

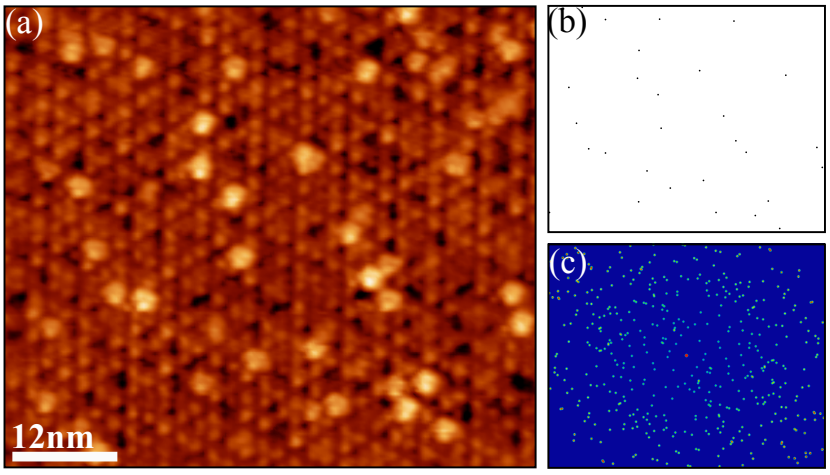

Figure 6.10: (a) Low coverage C_{60} deposition on the three-fold *i*-Ag-In-Yb surface at room temperature. No symmetry can be observed in the corresponding auto-correlation (c) of the molecular adsorption positions (b).

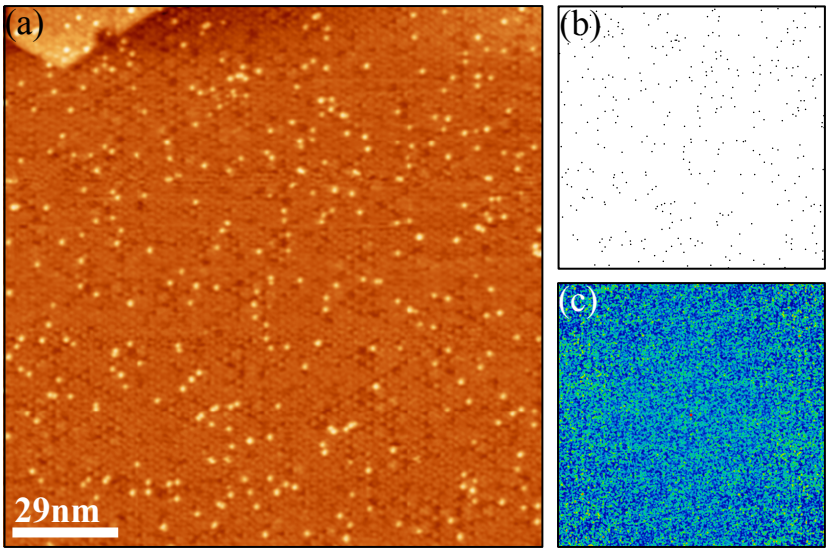

Figure 6.11: (a) Large scale scan of low coverage C_{60} deposition on the three-fold i-Ag-In-Yb surface. No symmetry can be observed in the corresponding auto-correlation (c) of the molecular adsorption positions (b).

molecular heights was also not observed in this system.

Increasing the coverage further led to disordered, rough surfaces containing large islands of disordered C_{60}. Monolayer creation was not possible due to the apparent increased sticking coefficient for C_{60} molecules to adsorb atop each other rather than the substrate.

The obvious differences in adsorption properties between the three-fold surface of *i*-Ag-In-Yb and the five-fold surface of *i*-Al-Cu-Fe is possibly attributed to the elemental components of the material rather than structure. In the five-fold surface it is suggested that C_{60} will most likely sit with a pentagonal face in direct contact with the surface to match the symmetries. If this were a key component of the ordered bonding, something similar would be possible with the hexagonal

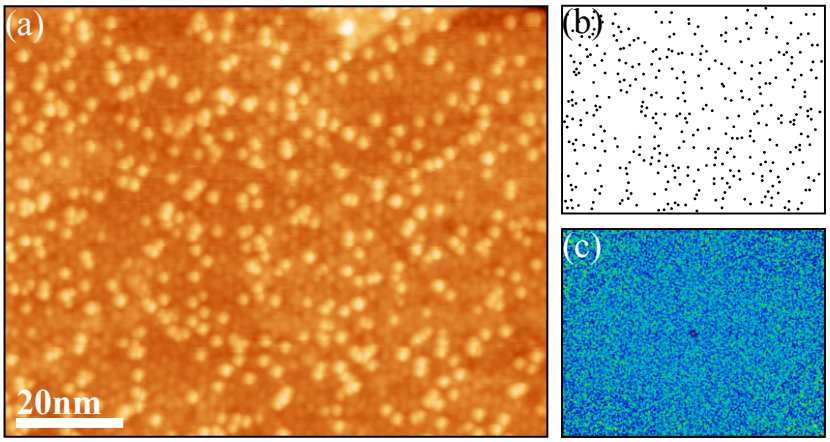

Figure 6.12: Increased C_{60} coverage on the three-fold *i*-Ag-In-Yb surface. The C_{60} forms a disordered layer.

faces of the C_{60} molecule. It is suggested that the key component in this difference is the lattice spacing of the least abundant element of the surface structure, in this case Yb. In *i*-Al-Cu-Fe Fe atoms adopted a nearest neighbour pentagonal lattice constant of 1.2 ± 0.2 nm (1.9 ± 0.4 nm for the non-degenerate lattice) which is larger than the van der Waals diameter of the C_{60} molecule (1 nm). In the three-fold surface of the *i*-Ag-In-Yb the nearest neighbour distance observed in the bulk truncated structure model of the Yb is 0.56 nm [176]. This suggests that the site separation of the active sites in this surface is too small to form an ordered layer of such a large molecule.

High temperature experiments were inconclusive as it proved difficult to adsorb enough C_{60} on the surface at elevated temperatures to create enough of an adlayer for analysis. There was some evidence of close packing of the C_{60} molecules although it was not possible to determine using the microscope whether the features were C_{60} or the periodic impurity phase of the QC.

6.3.3 C_{60} on the two-fold surface of *i*-Ag-In-Yb

The experiment was repeated on the two-fold surface of the *i*-Ag-In-Yb QC. Although large terraces appeared to be promising, to date it has not been possible to achieve atomic resolution on the two-fold surface [179]. C_{60} experiments were repeated regardless and images from this can be seen in Figures 6.13 and 6.14.

No convincing evidence of surface ordering was observed in either FFT or auto-correlations on the two-fold surface. C_{60} molecules also do not appear to have any preferential adsorption sites. The structure of the two-fold surface has the highest

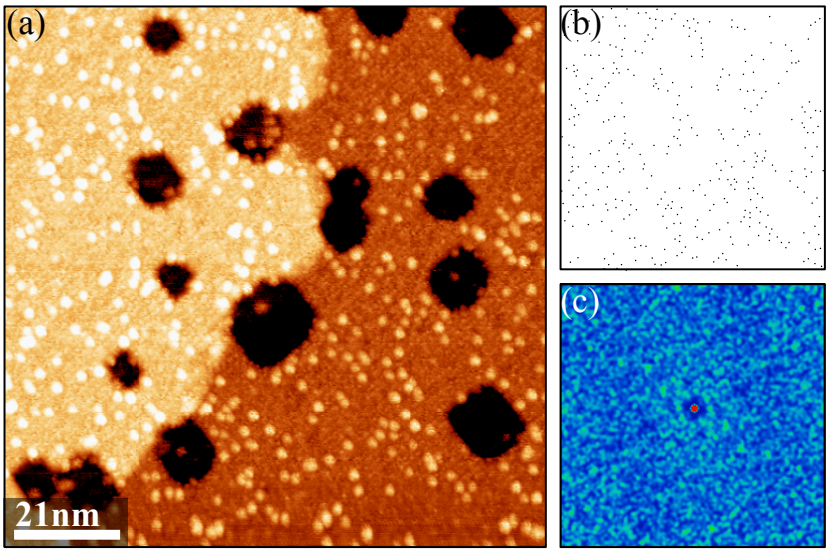

Figure 6.13: STM image of low C_{60} coverage on the two-fold surface of *i*-Ag-In-Yb including molecular position map and subsequent auto-correlation.

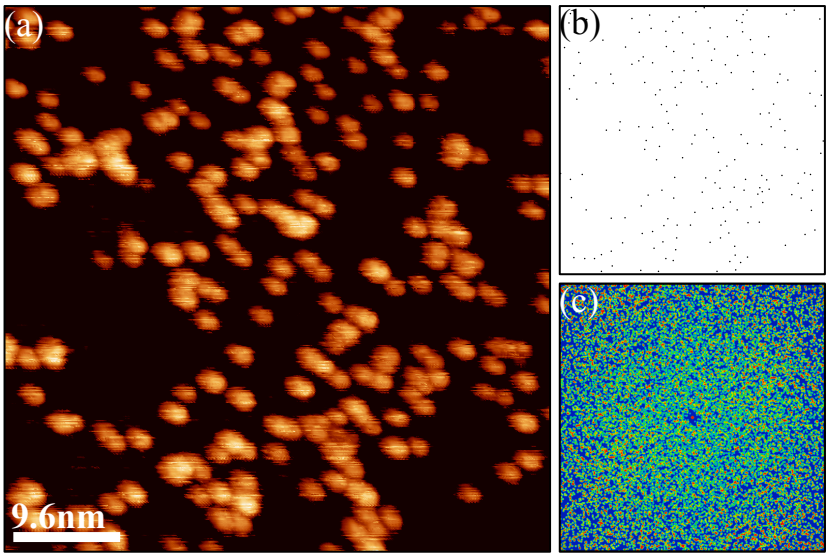

Figure 6.14: STM image of increased C_{60} coverage on the two-fold surface of i-Ag-In-Yb including molecular position map and subsequent auto-correlation.

atomic density of the high symmetry planes in the *i*-Cd-Yb structure with a Yb-Yb nearest neighbour distance of 0.57 nm in the top most layer. The surface has been shown to form rows with a separation of 1.53 $\pm$ 0.05 nm. In some cases the C_{60} appear to be residing along the rows, but the lack of high resolution reduces this to speculation although, the auto-correlation of the molecular positions does show two-fold symmetry. This suggests that the C_{60} reside in the row depressions across the surface in a disordered, non-specific manner. It is assumed, in the absence of clear evidence, that the lack of a specific adsorption site is due to this small nearest neighbour distance relative to the molecule size.

6.4 Summary

This work has presented STM images demonstrating some of the first evidence of two-dimensional hierarchical quasicrystalline growth. The pseudo-spherical C_{60} molecules adopt positions on a quasiperiodic lattice atop the five-fold surface of the *i*-Al-Cu-Fe QC at the Fe sites. This may explain the reactivity of Al-Cu-Fe for methanol decomposition and not SRM, as the reactivity of the Cu sites may be being blocked by the preference of Fe in the unleached surface. This was not the case on the three-fold and two-fold surfaces of the *i*-Ag-In-Yb.

It is suggested that the discrepancy may be due to the chemical bonding environment of the surface and subsurface. It is not expected that C_{60} molecules are inhibited from adopting specific lattice sites with three or two-fold rotational symmetry, based purely on geometrical factors as C_{60} is capable of matching both the two and three-fold symmetry of the surface. Therefore we infer that the

bonding environment provided by the adequately spaced Fe atoms in *i*-Al-Cu-Fe allows the advantageous adsorption characteristics, while the topological aspects of the crystal play a minor role or perhaps affect the orientation of the molecule. It was not possible in this study to establish the orientation of C_{60} molecules on the surface. Since the completion of this study, work published independently on similar systems has investigated epitaxially grown quasiperiodic molecular thin films and have confirmed the findings on the C_{60}/*i*-Al-Cu-Fe system while also identifying the orientation of C_{60} molecules in a pentagon-down orientation [180]. In fact it is suggested that in the Al-based QCs the C_{60} will "rather generally" form an interface between the electron deficient pentagonal C_{60} face and an adsorption site with five-fold symmetry to maximize electron transfer.

Chapter 7

Conclusions

The goal of the work described in this thesis was to determine the underlying roles of surface structure and surface chemistry in intermetallic compound catalysts used for the steam reforming of methanol. The steam reforming of methanol, when adequately catalysed, may provide an excellent route to hydrogen powered fuel cell vehicles or technologies. A study of this type must recognize that the pressure and materials gap create a genuine divide between lab studies and real world application and the results seen here must be carefully considered before being 'scaled-up' to industry. However this work has contributed to the discussion regarding the fundamental processes at work in these promising materials.

A mixture of experimental techniques including those in UHV and ambient conditions were used to study four intermetallic systems; leached Al-Cu-Fe, ZnPd, *i*-Al-Cu-Fe, *d*-Al-Ni-Co and *i*-Ag-In-Yb. Microstructure was investigated using SEM, STM, TEM, LEED and LEEM. The chemical nature of these surfaces was investigated using XPS, UPS and EBSD.

ZnPd was found to have strong preferences for surface structure, and significant restructuring of the surface can take place at relatively low temperatures. The compound, which is known to have a Cu-like DOS at the Fermi level, was found to have a surface terminated by complete Zn-Pd bonds wherever possible. This allows the maintenance of this DOS and fixed, separated active sites for the desired reaction pathways. This has been the first time the surface of a bulk crystal of this intermetallic compound, and not a surface alloy, has been studied. Furthermore, STM has been shown capable of providing atomic scale information on complex polycrystalline materials. This should give surface scientists confidence that results can be achieved on materials where large single crystals are not be available.

The leached five-fold surface of *i*-Al-Cu-Fe was found to adequately recreate the nanoparticles observed on powdered samples, and was able to form a model catalyst surface. A layered structure was found in which the catalytically active

Cu nanoparticles were dispersed with Fe and Fe oxide species in the subsurface layer. This dispersal helps to maintain the isolated active sites to maintain activity. It was also observed that the nanoparticles form an interface with the QC, whereby the highest density planes sit directly atop the QC surface. Also observed were five-fold cavities and facets similar to those from aggressive oxidation studies but never before seen following leaching treatments. These were interpreted as displaying a preference to leaching along the five-fold direction. It also suggested that rather than macroscopic surface orientation, crystallographic direction played a large role in determining leaching kinetics.

The effect of aperiodic atomic structure was investigated to assess its role in leaching kinetics. By simultaneously leaching a *d*-Al-Ni-Co QC with three well-orientated surfaces the effect was compared between surfaces of different QC or crystalline structure. The crystal was found to be most heavily leached along the periodic direction, displaying facets and cavities relating to this orientation. This may help to explain the success of certain QC catalysts in comparison to their crystalline counterparts. The QC structure will 'max-out' its leaching depth, while crystalline structures are leaching continuously and their structures have been seen to collapse from this effect. Both these leaching studies are believed to be the first example of the leaching of single-grain, well-defined surfaces, from which greater understanding of the powdered samples can be gained.

The concept of active site isolation in QC materials was investigated further by depositing C_{60} on the five-fold surface of *i*-Al-Cu-Fe, the three-fold surface of *i*-Ag-In-Yb and the two-fold surface of *i*-Ag-In-Yb. C_{60} was found to form a quasiperiodic lattice atop *i*-Al-Cu-Fe, adsorbing preferentially on surface and subsurface Fe atoms in the structure. The separation of the Fe atoms allowed for a unique lattice to be decorated, and aided the formation of the patterned overlayer. In both surfaces of the *i*-Ag-In-Yb crystal, C_{60} formed disordered layers, as had previously been seen on the five-fold surface. This was attributed to the much smaller site separation of the Yb atoms in the bulk which did not provide a lattice with enough spacing for any specific adsorption site. This study has highlighted the relevance of active site separation and isolation in order to form adequate and ordered adsorption.

The perspective for future work is potentially broad. With new techniques such as ambient pressure XPS more readily available to researchers, it should be possible to attempt to bridge the pressure and materials gap for these materials. A study of this type has already begun. It would also be interesting to take the model leached QC catalysts and perform flow reactor experiments upon them, accepting the drastic reduction in performance from the greatly reduced surface area.

More work can be considered in the laboratory too. During the work for this thesis, attempts to deposit gaseous reaction molecules on the surface of ZnPd were unsuccessful due to technical difficulties. There is no reason why this could not be performed again. Ultimately, when considering ZnPd, the largest single advance that could be made with this material would be to obtain a single grain sample that would allow reliable results and use low temperature microscopy to understand the adsorption properties of the reactant and product molecules. In addition, using spectroscopic techniques such as XPS or temperature controlled desorption it would be interesting to understand the adsorption properties of reaction molecules on the leached surface, and to investigate the relationship with powdered samples in greater depth.

Appendix A

UHV Techniques

A.1 UHV Pumps

To realise the required pressures of UHV, and understand the technical challenges involved in reducing the pressure to desired levels, it is important to understand the concept of flow regimes [181]. Above 10^{-2} mbar the atmosphere can be described as being in the viscous or turbulent flow regime. This is where the gases can be considered to be moving in fluid motion. Particles can be considered to be in constant interaction with the particles closest to them. When a volume in the viscous flow regime is put in contact with a volume of lower pressure, the gas molecules will 'flow' to the additional region in an attempt to create an equilibrium between the two volumes. The preferred direction of the particles is consistent with the macroscopic direction of flow for the gas as a whole.

Below pressures of 10^{-3} mbar, the gas can be described as being in the molecular flow regime, in this region the individual particles can be described as adhering to ballistic flow. In contrast to viscous flow, the average gas particle interacts with the walls of its container far more than with other particles of the gas. If a volume in this pressure range is connected to a volume of lower pressure still, equilibrium can take a much longer time to establish as particles move in straight lines, independent of the pressure gradient.

To pump a vacuum chamber down to the ballistic flow regime, the chamber must first pass through the viscous flow regime. Chambers are pumped first to a rough vacuum using rotary vane pumps (see figure A.1) , which use rotating vanes which separate gas from the chamber then force it out a oil sealed valve. These pumps create a rough vacuum of 10^{-3} mbar. After this it is possible to use turbo-molecular pumps to pump the chamber down to the UHV range. The turbo-molecular pump uses pairs of rotors and stators oppositely inclined to each other (figure A.2) . The rotors spin up to 30,000 rpm and transfer momentum to

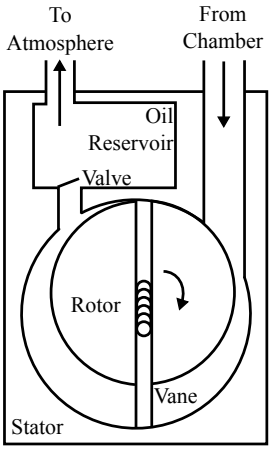

Figure A.1: Schematic of a rotary pump

the molecules being pumped. These are then in effect trapped by the stators and then further pumped through the mechanism before being removed by a rotary pump placed behind the turbo-molecular pump.

It is possible to reach UHV with a turbo-molecular pump alone, although the vibrations produced are often prohibitive when attempting techniques such as scanning tunnelling microscopy which is highly vibration-sensitive. In these circumstances the use of a sputter-ion pump is utilized. This pump is based on the sorption processes initiated by ionized gas particles following cold cathode discharge. The large potential difference (several keV) accelerates the ionized particles toward the titanium cathode where they are captured or chemisorbed (figure A.3). These pumps are surrounded by large magnets which cause the discharged electrons to move in a helical path, increasing the path length and therefore the chance of ionizing collision.

In addition, one can use a titanium sublimation pump as a complementary pump in the chamber. This uses a high current through a titanium filament to sublime the metal onto the chamber walls with a high surface area, creating an active surface for chemisorption most commonly for hydrogen which is otherwise

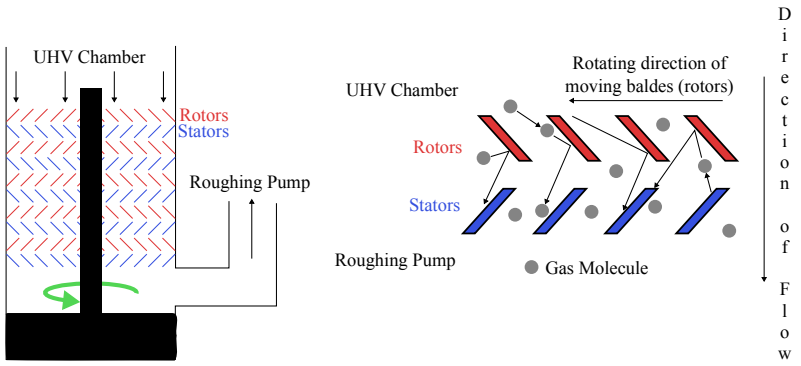

Figure A.2: Cut-through of turbo-molecular pump

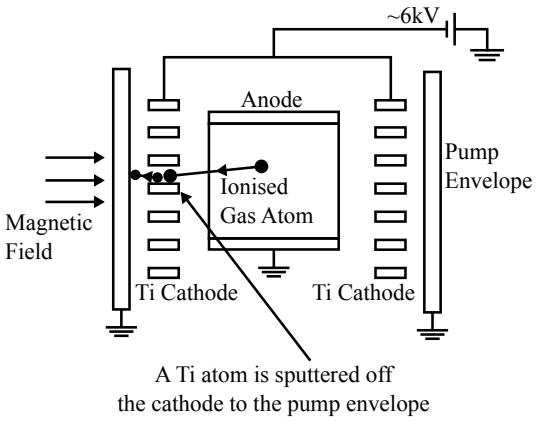

Figure A.3: Schematic of ion pump

difficult to pump. The efficiency of this pump can be greatly increased by cooling the surface in combination with a liquid nitrogen trap although this technique is not at use within the experimental systems of this study.

A.2 Pressure Gauges

The measurement of pressure requires different means in differing flow regimes. In the higher, viscous flow regime, pressure is measured using a Piriani gauge (figure A.4). This works by passing a current through a filament in the chamber, the temperature of the filament is affected by the collision of gas particles, which in turn affects the resistance of the filament. This change of resistance is used to determine the pressure down to 10^{-3} mbar at which point the collisions are too low to determine a change in resistance.

In the molecular flow regime pressure must be measured with an ionization gauge (figure A.5). A filament is used to provide thermionic emission of electrons, which are then accelerated across a large potential difference toward a positively biased cage. Electrons frequently pass through the cage before being turned back toward the anode, however the electron may ionize a gas particle inside the cage, which is then accelerated toward the negatively biased collector. The current

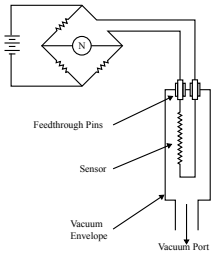

Figure A.4: Circuit of piriani gauge

observed from the collector is then used to determine the pressure.

A.3 Mass Spectrometry (MS)

Mass Spectrometry is a vital tool to understand the residual gases present in a vacuum chamber. In this sense, the mass spectrometer is used mainly within this study as a residual gas analyzer. The mass spectrometer uses quadrupole technology to filter ions entering the detector. The main processes inside the mass spectrometer are the ionization of gas molecules, the filtering of ions through the detector and the eventual detection of the ion. The results are then combined into a spectrum showing the peaks for each ion detected. This allows the user to understand what gases are present or to accurately calibrate the presence or confirm the purity of any deliberately introduced gases.

Initially gas molecules are ionized by their proximity to a heated cathode undergoing thermionic emission and accelerating electrons toward the anode. Gas molecules that pass through this region are ionized and subsequently accelerated along a path through the quadrupole analyzer. By placing oscillating radio frequency voltages between one pair of rods and the other, the quadrupole selectively causes ions of certain mass to charge ratios to reach resonance on their path through, all other ions are forced into the poles and away from the detector. Once through the quadrupole the ion is collected by the detector and turned into an intensity based on the number of ions collected. By scanning the frequency of the voltages on the poles, the device scans through the mass to charge ratios and counts the number of ions for each window. By this method it is possible to

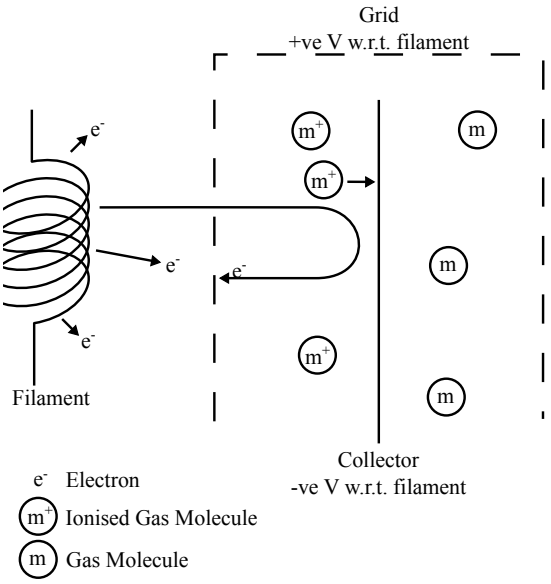

Figure A.5: Working principle of ion gauge

collect a spectrum of the gas molecules present.

Mass spectrometry was mostly used to ensure high quality vacuum during UHV experiments or to understand the behaviour of molecular evaporators. Constant pressure rises during evaporant heating indicated constant deposition, whereas erratic pressure fluctuations signified continued out gassing of impurities in the evaporant. The mass spectrometer was also used to rule out Zn evaporation from the ZnPd sample during annealing when developing an cleaning regime for the sample, this is discussed in greater detail in section 3.3.2.

Appendix B

Publications

Published Works

- G.M. McGuirk, J. Ledieu, E. Gaudry, M.C. de Weerd, M. Hahne, P. Gille, D. Ivarsson, M. Armbrüster, J. Ardini, G. Held, F. Macherozzi, A. Bayer, **M. Lowe**, K. Pussi, R.D. Diehl, V. Fournée. The atomic structure of low-index surfaces of the intermetallic compound InPd. *Journal of Chemical Physics,* 143, pp. 074705, 2015.

- **M. Lowe**, T.P. Yadav, V. Fournée, J. Ledieu, R. McGrath and H.R. Sharma. Influence of leaching on surface composition, microstructure and valence band of single grain icosahedral Al-Cu-Fe quasicrystal. *Journal of Chemical Physics*, 142, pp. 094703, 2015.

- J. Smerdon, K.M. Young, **M. Lowe**, S.S. Hars, T.P. Yadav, D. Hesp, V.R. Dhanak, A.P. Tsai, H.R. Sharma and R. McGrath. Templated quasicrystalline molecular ordering. *Nano Letters*, 14(3), pp. 1184-1189, 2014.

- **M. Lowe**, P. Gille, R. McGrath and H.R. Sharma, Leaching effect on multiple surfaces of a single grain decagonal Al-Ni-Co quasicrystal. *Acta Physica Polonica A*, 126(2), pp. 520-523, 2014.

- T.P. Yadav, S.S. Mishra, S.K. Pandey, D. Singh, **M. Lowe**, R. Tamura, N.K. Mukhopadhyay, O.N. Srivastava, R. McGrath and H.R. Sharma. Leaching of Al-based polygrain quasicrystalline and related crystalline surfaces. *Acta Physica Polonica A*, 126(2), pp. 629-632, 2014.

- T.P. Yadav, **M. Lowe**, R. Tamura, R. McGrath and H.R. Sharma. Effect of leaching on surface microstructure and chemical composition of Al-based quasicrystals. S. Schmid *et al.* (eds.), *Aperiodic Crystals*, Springer Science, Ch37, pp. 275-282, 2013.

- **M. Lowe**, A. Al-Mahboob, D. Ivarsson, M. Armbrüster, J. Ardini, G. Held, F. Maccherozzi, A. Bayer, V. Fournée, J. Ledieu, R. McGrath and H.R. Sharma. *In preparation.*

- A. Al-Mahboob, **M. Lowe**, R. McGrath and H.R. Sharma, Transition state limited kinetics in stabilizing intermetallic surfaces. *In preparation.*

Oral Presentations

- *Characterisation of clean polycrystalline ZnPd surfaces.* 4th International Symposium of Intermetallic Compounds in Catalysis, 2014.

- *Quasicrystals as catalysts for the steam reforming of methanol: a study of the leached surfaces of single grain quasicrystals.* International Conference on Quasicrystals, 2013.

- *Preparation and characterisation of a clean polycrystalline ZnPd surface.* 3rd International Symposium of Intermetallic Compounds in Catalysis, 2013.

- *Quasicrystals as catalysts for the steam reforming of methanol: a study of the leached surface of single grain Al-Cu-Fe quasicrystal.* Interdisciplinary Surface Science Conference, 2013.

- *Pentagonal facets on the leached fivefold Al-Cu-Fe quasicrystalline surface.* European Conference on Surface Science, 2012.

Poster Presentations

- *Effect of leaching on surface microstructure and chemical composition of Al-based quasicrystals.* CMAC Euroschool, 2014.

- *Preparation and characterisation of a clean polycrystalline ZnPd surface.* CMAC Days, 2012.

- *Pentagonal facets on the leached fivefold Al-Cu-Fe quasicrystalline surface.* 2nd International Symposium of Intermetallic Compounds in Catalysis, 2012.

Appendix C

Table of Abbreviations

AFM	Atomic Force Microscopy
BCT	Body Centred Tetragonal
CCD	Charge Coupled Device
d	Decagonal
DFT	Density Functional Theory
DOS	Density of States
EBSD	Electron Back Scattered Diffraction
EDX	Energy Dispersive X-ray Analysis
FCT	Face Centred Tetragonal
FFT	Fast Fourier Transform
i	Icosahedral
IMC	Intermetallic Compound
LEED	Low Energy Electron Diffraction
LEEM	Low Energy Electron Microscope
MEM	Mirror Electron Microscopy
MS	Mass Spectrometry
PEEM	Photoexcitation Electron Microscope
PEMFC	Proton Exchange Membrane Fuel Cell
QC	Quasicrystal
SAED	Selected Area Electron Diffraction
SEM	Scanning Electron Microscope
SRM	Steam Reforming of Methanol
STM	Scanning Tunneling Microscope
TEM	Transmission Electron Microscope
UHV	Ultra High Vacuum
UPS	Ultraviolet Photoelectron Spectroscopy
UV	Ultraviolet Radiation
XPS	X-ray Photoelectron Spectroscopy
XRD	X-ray Diffraction

*Abbreviations from table 3.2 on page 50 omitted for relevence.

List of Tables

List of Figures

Bibliography

[1] International Energy Agency. *2011 Key World Energy Statistics*. OECD/IEA, 2011.

[2] International Energy Agency. *2014 Key World Energy Statistics*. OECD/IEA, 2014.

[3] G.A. Olah. After oil and gas: Methanol economy. *Catalysis Letters*, 93(1-2):1–2, 2004.

[4] T. Barker, P. Ekins, and N. Johnstone. *Global Warming and Energy Demand*. Routledge, 1995.

[5] R. von Helmolt and U. Eberle. Fuel cell vehicles: Status 2007. *Journal of Power Sources*, 165(2):833–843, 2007.

[6] J. Romm. The car and fuel of the future. *Energy Policy*, 34(17):2609–2614, 2006.

[7] K.S. Choi, I.J. Choi, S.J. Hwang, H.M. Kim, J.L. Dorr, and P. A. Erickson. An experimental study of methanol autothermal reformation as a method of producing hydrogen for transportation applications. *International Journal of Hydrogen Energy*, 35(12):6210–6217, 2010.

[8] S. Ahmed and M. Krumpelt. Hydrogen from hydrocarbon fuels for fuel cells. *International Journal of Hydrogen Energy*, 26(4):291–301, 2001.

[9] W.H. Heffner, A.C. Veverka, and G.T. Skaperdas. *Fuel Cell Systems*, chapter 24 - Hydrogen-Generating Plant Based on Methanol Decomposition, pages 318–331. American Chemical Society, 1969.

[10] Y.H. Chin, R. Dagle, J. Hu, A.C. Dohnalkova, and Y. Wang. Steam reforming of methanol over highly active Pd/ZnO catalyst. *Catalysis Today*, 77(1-2):79–88, 2002.

[11] S.R. Samms and R.F. Savinell. Kinetics of methanol-steam reformation in an internal reforming fuel cell. *Journal of Power Sources*, 112(1):13–29, 2002.

[12] G.K. Smith, S. Lin, W. Lai, A. Datye, D. Xie, and H. Guo. Initial steps in methanol steam reforming on PdZn and ZnO surfaces: Density functional theory studies. *Surface Science*, 605(7-8):750–759, 2011.

[13] D.R. Palo, R.A. Dagle, and J.D. Holladay. Methanol steam reforming for hydrogen production. *Chemical Reviews*, 107(10):3992–4021, 2007.

[14] H. Gabasch, A. Knop-Gericke, R. Schlögl, S. Penner, B. Jenewein, K. Hayek, and B. Klötzer. Zn adsorption on Pd(111): ZnO and PdZn alloy formation. *Journal of Physical Chemistry B*, 110(23):11391–11398, 2006.

[15] V.D. Phillips and P.K. Takahashi. Methanol from biomass. *Environmental Science and Technology*, 24(8):1136–1137, 1990.

[16] C. Rameshan, W. Stadlmayr, C. Weilach, S. Penner, H. Lorenz, M. Hävecker, R. Blume, T. Rocha, D. Teschner, A. Knop-Gericke, R. Schlögl, N. Memmel, D. Zemlyanov, G. Rupprechter, and B. Klötzer. Subsurface-controlled CO_2 selectivity of PdZn near-surface alloys in H_2 generation by methanol steam reforming. *Angewandte Chemie - International Edition*, 49(18):3224–3227, 2010.

[17] V. Mehta and J.S. Cooper. Review and analysis of PEM fuel cell design and manufacturing. *Journal of Power Sources*, 114(1):32–53, 2003.

[18] L.F. Brown. A comparative study of fuels for on-board hydrogen production for fuel-cell-powered automobiles. *International Journal of Hydrogen Energy*, 26(4):381–397, 2001.

[19] K. Nozawa, N. Endo, S. Kameoka, A.P. Tsai, and Y. Ishii. Catalytic properties dominated by electronic structures in PdZn, NiZn, and PtZn intermetallic compounds. *Journal of the Physical Society of Japan*, 80(6), 2011.

[20] W. Stadlmayr, S. Penner, B. Klötzer, and N. Memmel. Growth, thermal stability and structure of ultrathin Zn-layers on Pd(111). *Surface Science*, 603(1):251–255, 2009.

[21] S. Lin, D. Xie, and H. Guo. Pathways of methanol steam reforming on PdZn and comparison with Cu. *Journal of Physical Chemistry C*, 115(42):20583–20589, 2011.

[22] N. Iwasa, S. Masuda, N. Ogawa, and N. Takezawa. Steam reforming of methanol over Pd/ZnO: Effect of the formation of PdZn alloys upon the reaction. *Applied Catalysis A, General*, 125(1):145–157, 1995.

[23] K.R. Webb. Sir William Robert Grove (1811-1896) and the origins of the fuel cell. *Journal of the Royal Institute of Chemistry*, 85:291–320, 1961.

[24] G. Simader. *Fuel Cells and Their Applications*. John Wiley & Sons, Incorporated, 2005.

[25] M. Grujicic, C.L. Zhao, K.M. Chittajallu, and J.M. Ochterbeck. Cathode and interdigitated air distributor geometry optimization in polymer electrolyte membrane (PEM) fuel cells. *Materials Science and Engineering: B*, 108(3):241–252, 2004.

[26] J.J. Berzelius. Considerations respecting a new power which acts in the formation of organic bodies. *Edinburgh New Philosophical Journal*, 21:223–228, 1836.

[27] M. Bowker. *The Basis and Applications of Heterogeneous Catalysis*. Oxford Chemistry Primers, 1998.

[28] V. Smil. Detonator of the population explosion. *Nature*, 400(6743):415–415, 1999.

[29] D.W. Blakely and G.A. Somorjai. The dehydrogenation and hydrogenolysis of cyclohexane and cyclohexene on stepped (high miller index) platinum surfaces. *Journal of Catalysis*, 42(2):181–196, 1976.

[30] M. Armbrüster, R. Schlögl, and Yu. Grin. Intermetallic compounds in heterogeneous catalysis—a quickly developing field. *Science and Technology of Advanced Materials*, 15(3):034803, 2014.

[31] K.W. Kolasinski. *Experimental Probes and Techniques*, pages 51–114. John Wiley & Sons, Ltd, 2012.

[32] A. Roudgar and A. Groß. Local reactivity of thin Pd overlayers on Au single crystals. *Journal of Electroanalytical Chemistry*, 548(0):121–130, 2003.

[33] P. Sabatier. Hydrogénations et déshydrogénations par catalyse. *Berichte der Deutschen Chemischen Gesellschaft*, 44(3):1984–2001, 1911.

[34] B. Hammer and J.K. Nørskov. Electronic factors determining the reactivity of metal surfaces. *Surface Science*, 343(3):211–220, 1995.

[35] J. Singh, R.C. Nelson, B.C. Vicente, S.L. Scott, and J.A. van Bokhoven. Electronic structure of alumina-supported monometallic Pt and bimetallic PtSn catalysts under hydrogen and carbon monoxide environment. *Physical Chemistry Chemical Physics*, 12:5668–5677, 2010.

[36] J.R. Kitchin, J.K. Nørskov, M.A. Barteau, and J.G. Chen. Role of strain and ligand effects in the modification of the electronic and chemical properties of bimetallic surfaces. *Physical Review Letters*, 93:156801, 2004.

[37] E. Nikolla, J. Schwank, and S. Linic. Measuring and relating the electronic structures of nonmodel supported catalytic materials to their performance. *Journal of the American Chemical Society*, 131(7):2747–2754, 2009.

[38] J. Prinz, R. Gaspari, C.A. Pignedoli, J. Vogt, P. Gille, M. Armbrüster, H. Brune, O. Gröning, D. Passerone, and R. Widmer. Isolated Pd sites on the intermetallic PdGa(111) and PdGa($\bar{1}\bar{1}\bar{1}$) model catalyst surfaces. *Angewandte Chemie International Edition*, 51(37):9339–9343, 2012.

[39] J.H. Westbrook. Applications of intermetallic compounds. *MRS Bulletin*, 21:26–29, 1996.

[40] K. Kovnir, M. Armbrüster, D. Teschner, T.V. Venkov, F.C. Jentoft, A. Knop-Gericke, Yu. Grin, and R. Schlögl. A new approach to well-defined, stable and site-isolated catalysts. *Science and Technology of Advanced Materials*, 8(5):420–427, 2007.

[41] M. Armbrüster, K. Kovnir, M. Behrens, D. Teschner, Yu. Grin, and R. Schlögl. Pd-Ga intermetallic compounds as highly selective semihydrogenation catalysts. *Journal of the American Chemical Society*, 132(42):14745–14747, 2010.

[42] A. Ota, M. Armbrüster, M. Behrens, D. Rosenthal, M. Friedrich, I. Kasatkin, F. Girgsdies, W. Zhang, R. Wagner, and R. Schlögl. Intermetallic compound Pd_2Ga as a selective catalyst for the semi-hydrogenation of acetylene: From model to high performance systems. *The Journal of Physical Chemistry C*, 115(4):1368–1374, 2011.

[43] J. Osswald, R. Giedigkeit, R.E. Jentoft, M. Armbrüster, F. Girgsdies, K. Kovnir, T. Ressler, Yu. Grin, and R. Schlögl. Palladium–gallium intermetallic compounds for the selective hydrogenation of acetylene: Part I: Preparation and structural investigation under reaction conditions. *Journal of Catalysis*, 258(1):210–218, 2008.

[44] J. Osswald, K. Kovnir, M. Armbrüster, R. Giedigkeit, R.E. Jentoft, U. Wild, Yu. Grin, and R. Schlögl. Palladium–gallium intermetallic compounds for the selective hydrogenation of acetylene: Part II: Surface characterization and catalytic performance. *Journal of Catalysis*, 258(1):219–227, 2008.

[45] M. Friedrich, D. Teschner, A. Knop-Gericke, and M. Armbrüster. Influence of bulk composition of the intermetallic compound ZnPd on surface composition and methanol steam reforming properties. *Journal of Catalysis*, 285(1):41–47, 2012.

[46] N. Iwasa, T. Mayanagi, N. Ogawa, K. Sakata, and N. Takezawa. New catalytic functions of Pd-Zn, Pd-Ga, Pd-In, Pt-Zn, Pt-Ga and Pt-In alloys in the conversions of methanol. *Catalysis Letters*, 54(3):119–123, 1998.

[47] T. Hirano, Y. Ozawa, T. Sekido, T. Ogino, T. Miyao, and S. Naito. The role of additives in the catalytic reduction of NO by CO over Pd-In/SiO_2 and Pd-Pb/SiO_2 catalysts. *Applied Catalysis A: General*, 320:91–97, 2007.

[48] F.A. Marchesini, S. Irusta, C. Querini, and E. Miró. Spectroscopic and catalytic characterization of Pd-In and Pt-In supported on Al_2O_3 and SiO_2, active catalysts for nitrate hydrogenation. *Applied Catalysis A: General*, 348(1):60–70, 2008.

[49] M. Armbrüster, K. Kovnir, M. Friedrich, D. Teschner, G. Wowsnick, M. Hahne, P. Gille, L. Szentmiklosi, M. Feuerbacher, M. Heggen, F. Girgsdies, D. Rosenthal, R. Schlogl, and Yu. Grin. $Al_{13}Fe_4$ as a low-cost alternative for palladium in heterogeneous hydrogenation. *Nature Materials*, 11(8):690–693, 2012.

[50] A.P. Tsai, S. Kameoka, and Y. Ishii. PdZn=Cu: Can an intermetallic compound replace an element? *Journal of the Physical Society of Japan*, 73(12):3270–3273, 2004.

[51] M. Raney. Method of preparing catalytic material. *US Patent 1,563,787*, 1925.

[52] M. Raney. Method of producing finely divided nickel. *US Patent 1,628,190*, 1927.

[53] C.J. Jenks and P.A. Thiel. Comments on quasicrystals and their potential use as catalysts. *Journal of Molecular Catalysis A: Chemical*, 131(1–3):301–306, 1998.

[54] M. Boudart. Model catalysts: reductionism for understanding. *Topics in Catalysis*, 13(1-2):147–149, 2000.

[55] G. Ertl. Surface science and catalysis. In *Studies in Surface Science and Catalysis*, pages 21–35. Elsevier BV, 1981.

[56] R.A. Armstrong and J.P. Hobson. The contribution of ultrahigh vacuum science to catalysis. In *Catalysis on the Energy Scene*, pages 33–43. Elsevier BV, 1984.

[57] C. Wen, Y. Liu, and F. Tao. Integration of surface science, nanoscience, and catalysis. *Pure Applied Chemistry*, 83(1):243–252, 2011.

[58] G. McGuirk, J. Ledieu, E. Gaudry, M.C. de Weerd, M. Hahne, P. Gille, D. Ivarsson, M. Armbruster, J. Ardini, G. Held, F. Maccherozzi, A. Bayer, M. Lowe, K. Pussi, R. Diehl, and V. Fournée. The atomic structure of low-index surfaces of the InPd intermetallic compound. *Journal of Chemical Physics - Submitted*, 2015.

[59] A. Einstein. Über einen die Erzeugung und Verwandlung des Lichtes betreffenden heuristischen Gesichtspunkt. *Annalen der Physik*, 322(6):132–148, 1905.

[60] K. Siegbahn, C. Nordling, A. Fahlman, R. Nordberg, K. Hamrin, J. Hedman, G. Johansson, T. Bergmark, S.E. Karlsson, I. Lindgren, and B. Lindberg. ESCA: Atomic, molecular and solid state structure studied by means of electron spectroscopy. *Nova Acta Regiae Societatis Scientiarum Upsaliensis*, 20, 1967.

[61] B.D. Ratner and D.G. Castner. *Electron Spectroscopy for Chemical Analysis*, pages 47–112. John Wiley & Sons, Ltd, 2009.

[62] Omicron Nanotechnology. *EA 125 Energy Analyser User's Guide*, version 2.1 edition, 2002.

[63] K. Berresheim, M. Mattern-Klosson, and M. Wilmers. A standard form of spectra for quantitative ESCA-analysis. *Fresenius' Journal of Analytical Chemistry*, 341(1-2):121–124, 1991.

[64] H.G. Nöller, H.D. Polaschegg, and H. Schillalies. A step towards quantitative electron spectroscopy measurements by improved electron optics. *Journal of Electron Spectroscopy and Related Phenomena*, 5(1):705–723, 1974.

[65] N. Fairley. *CasaXPS manual 2.3.15. XPS AES ToF-MS SNMS dynamic-SIMS*. Acolyte Science, 2009.

[66] S. Tanuma, C.J. Powell, and D.R. Penn. Calculations of electron inelastic mean free paths. II. data for 27 elements over the 50 to 2000 eV range. *Surface and Interface Analysis*, 17(13):911–926, 1991.

[67] S. Tanuma, C.J. Powell, and D.R. Penn. Calculations of electron inelastic mean free paths. V. data for 14 organic compounds over the 50–2000 eV range. *Surface and Interface Analysis*, 21(3):165–176, 1994.

[68] S. Tanuma, T. Shiratori, T. Kimura, K. Goto, S. Ichimura, and C.J. Powell. Experimental determination of electron inelastic mean free paths in 13 elemental solids in the 50 to 5000 eV energy range by elastic-peak electron spectroscopy. *Surface and Interface Analysis*, 37(11):833–845, 2005.

[69] J.J. Yeh and I. Lindau. Atomic subshell photoionization cross sections and asymmetry parameters: 1 z 103. *Atomic Data and Nuclear Data Tables*, 32(1):1–155, 1985.

[70] CasaXPS. http://www.casaxps.com/.

[71] A. Khursheed. *Scanning Electron Microscope Optics and Spectrometers*. World Scientific, 2011.

[72] G. Binnig, C.F. Quate, and Ch. Gerber. Atomic force microscope. *Physical Review Letters*, 56:930–933, March 1986.

[73] R. Garcia and R. Perez. Dynamic atomic force microscopy methods. *Surface Science Reports*, 47(6):197–301, 2002.

[74] T.R. Albrecht, P. Grütter, D. Horne, and D. Rugar. Frequency modulation detection using high-Q cantilevers for enhanced force microscope sensitivity. *Journal of Applied Physics*, 69(2):668–673, 1991.

[75] L. Gross, F. Mohn, N. Moll, P. Liljeroth, and G. Meyer. The chemical structure of a molecule resolved by atomic force microscopy. *Science*, 325(5944):1110–1114, 2009.

[76] J. Repp, G. Meyer, S.M. Stojković, A. Gourdon, and C. Joachim. Molecules on insulating films: Scanning-tunneling microscopy imaging of individual molecular orbitals. *Physical Review Letters*, 94:026803, 2005.

[77] I. Horcas, R. Fernández, J.M. Gómez-Rodríguez, J. Colchero, J. Gómez-Herrero, and A.M. Baro. WSxM: A software for scanning probe microscopy and a tool for nanotechnology. *Review of Scientific Instruments*, 78(1):013705, 2007.

[78] D. Necas and P. Klapetek. Gwyddion: an open-source software for SPM data analysis. *Central European Journal of Physics*, 10(1):181–188, 2012.

[79] C.J. Powell. The quest for universal curves to describe the surface sensitivity of electron spectroscopies. *Journal of Electron Spectroscopy and Related Phenomena*, 47:197–214, 1988.

[80] K.Z. Baba-Kishi. Review electron backscatter kikuchi diffraction in the scanning electron microscope for crystallographic analysis. *Journal of Materials Science*, 37(9):1715–1746, 2002.

[81] R.A. Schwarzer. Automated crystal lattice orientation mapping using a computer-controlled SEM. *Micron*, 28(3):249–265, 1997.

[82] S.S. Dhesi, S.A. Cavill, A. Potenza, H. Marchetto, R.A. Mott, P. Steadman, A. Peach, E.L. Shepherd, X. Ren, U.H. Wagner, and R. Reininger. The nanoscience beamline (I06) at diamond light source. *AIP Conference Proceedings*, 1234(1):311–314, 2010.

[83] F.M. Mueller, A.J. Freeman, J.O. Dimmock, and A.M. Furdyna. Electronic structure of palladium. *Physical Review B*, 1:4617–4635, 1970.

[84] E.R. Jette and F. Foote. Precision determination of lattice constants. *The Journal of Chemical Physics*, 3(10):605–616, 1935.

[85] E. Jeroro, V. Lebarbier, A. Datye, Y. Wang, and J.M. Vohs. Interaction of CO with surface PdZn alloys. *Surface Science*, 601(23):5546–5554, 2007.

[86] Y. Wang, R. Dagle, Y.H. Chin, D. Palo, J. Hu, and J. Holladay. Methane and methanol steam reforming to produce hydrogen using catalytic microchannel reactors. *ACS Division of Fuel Chemistry, Preprints*, 47(1):114–115, 2002.

[87] M. Friedrich, A. Ormeci, Y. Grin, and M. Armbrüster. PdZn or ZnPd: Charge transfer and Pd–Pd bonding as the driving force for the tetragonal distortion of the cubic crystal structure. *Zeitschrift für anorganische und allgemeine Chemie*, 636(9-10):1735–1739, 2010.

[88] A. Bayer, K. Flechtner, R. Denecke, H.-P. Steinrück, K.M. Neyman, and N. Rösch. Electronic properties of thin Zn layers on Pd(111) during growth and alloying. *Surface Science*, 600(1):78–94, 2006.

[89] W. Stadlmayr, Ch. Rameshan, Ch. Weilach, H. Lorenz, M. Hävecker, R. Blume, T. Rocha, D. Teschner, A. Knop-Gericke, D. Zemlyanov, S. Penner, R. Schlögl, G. Rupprechter, B. Klötzer, and N. Memmel. Temperature-induced modifications of PdZn layers on Pd(111). *Journal of Physical Chemistry C*, 114(24):10850–10856, 2010.

[90] T. P. Yadav, M. Lowe, R. Tamura, R. McGrath, and H. R. Sharma. Effect of leaching on surface microstructure and chemical composition of al-based quasicrystals. In *Aperiodic Crystals*, pages 275–282. Springer Science, 2013.

[91] A. Tamtögl, M. Kratzer, J. Killman, and A. Winkler. Adsorption/desorption of H_2 and CO on Zn-modified Pd(111). *Journal of Chemical Physics*, 129(22), 2008.

[92] C.A. Leighton, A.J. Swift, and J.C. Vickerman. Further characterisation of Pd deposited on an extensively oxidised Zn(001) support. *Surface Science*, 253(1-3):220–232, 1991.

[93] W. Stadlmayr, B. Kratzer, S. Penner, and N. Memmel. Growth and alloying of ultra-thin Zn layers on Pd(110). *The Journal of Physical Chemistry C*, 116(5):3635–3644, 2012.

[94] Z.X. Chen, K.M. Neyman, and N. Rösch. Theoretical study of segregation of Zn and Pd in Pd–Zn alloys. *Surface Science*, 548(1–3):291–300, 2004.

[95] H.P. Koch, I. Bako, G. Weirum, M. Kratzer, and R. Schennach. A theoretical study of Zn adsorption and desorption on a Pd(111) substrate. *Surface Science*, 604(11-12):926–931, 2010. cited By (since 1996) 3.

[96] X. He, Y. Huang, and Z.X. Chen. Zinc coverage dependent structure of PdZn surface alloy. *Physical Chemistry Chemical Physics*, 13(1):107–109, 2011.

[97] A. Fasana, I. Abbati, and L. Braicovich. Photoemission evidence of surface segregation at liquid-nitrogen temperature in Zn-Pd system. *Physical Review B*, 26(8):4749–4751, 1982.

[98] J.A. Rodriguez. Interactions in bimetallic bonding: Electronic and chemical properties of PdZn surfaces. *Journal of Physical Chemistry*, 98(22):5758–5764, 1994.

[99] M. Kratzer, A. Tamtögl, J. Killmann, R. Schennach, and A. Winkler. Preparation and calibration of ultrathin Zn layers on Pd(111). *Applied Surface Science*, 255(11):5755–5759, 2009.

[100] G. Weirum, M. Kratzer, H.P. Koch, A. Tamtogl, J. Killmann, I. Bako, A. Winkler, S. Surnev, F.P. Netzer, and R. Schennach. Growth and desorption kinetics of ultrathin Zn layers on Pd(111). *Journal of Physical Chemistry C*, 113(22):9788–9796, 2009.

[101] C. Rameshan, C. Weilach, W. Stadlmayr, S. Penner, H. Lorenz, M. Hävecker, R. Blume, T. Rocha, D. Teschner, A. Knop-Gericke, R. Schlögl, D. Zemlyanov, N. Memmel, G. Rupprechter, and B. Klötzer. Steam reforming of methanol on PdZn near-surface alloys on Pd(111) and Pd foil studied by in-situ XPS, LEIS and PM-IRAS. *Journal of Catalysis*, 276(1):101–113, 2010.

[102] I. Kovács, J. Kiss, and F. Solymosi. The adsorption properties of $PdZn_x$ alloy on Pd(100): Preparation and characterization. *Vacuum*, 82(2):182–185, 2007.

[103] E. Jeroro and J.M. Vohs. Exploring the role of Zn in PdZn reforming catalysts: Adsorption and reaction of ethanol and acetaldehyde on two-dimensional PdZn alloys. *Journal of Physical Chemistry C*, 113(4):1486–1494, 2009.

[104] Q. Zhang and R.J. Farrauto. A PdZn catalyst supported on stabilized ceria for stoichiometric methanol steam reforming and hydrogen production. *Applied Catalysis A: General*, 395(1-2):64–70, 2011.

[105] T. Conant, A.M. Karim, V. Lebarbier, Y. Wang, F. Girgsdies, R. Schlögl, and A. Datye. Stability of bimetallic Pd-Zn catalysts for the steam reforming of methanol. *Journal of Catalysis*, 257(1):64–70, 2008.

[106] S. Sá, H. Silva, L. Brandão, J.M. Sousa, and A. Mendes. Catalysts for methanol steam reforming-a review. *Applied Catalysis B: Environmental*, 99(1-2):43–57, 2010.

[107] C. Weilach. ZnPd preparation technique. Personal Communication, 2011.

[108] Z.A. Munir, U. Anselmi-Tamburini, and M. Ohyanagi. The effect of electric field and pressure on the synthesis and consolidation of materials: a review of the spark plasma sintering method. *Journal of Materials Science*, 41(3):763–777, 2006.

[109] K.S. Kim, A.F. Gossmann, and N. Winograd. X-ray photoelectron spectroscopic studies of palladium oxides and the palladium-oxygen electrode. *Analytical Chemistry*, 46(2):197–200, 1974.

[110] C.J. Powell. Recommended Auger parameters for 42 elemental solids. *Journal of Electron Spectroscopy and Related Phenomena*, 185(1–2):1–3, 2012.

[111] J.C. Klein and D.M. Hercules. Surface characterization of model urushibara catalysts. *Journal of Catalysis*, 82(2):424–441, 1983.

[112] A. Lebugle, U. Axelsson, R. Nyholm, and N. Mårtensson. Experimental L and M core level binding energies for the metals ^{2}2Ti to ^{3}0Zn. *Physica Scripta*, 23(5A):825, 1981.

[113] M. Armbrüster, M. Behrens, K. Föttinger, M. Friedrich, É. Gaudry, S.K. Matam, and H.R. Sharma. The intermetallic compound ZnPd and its role in methanol steam reforming. *Catalysis Reviews*, 55(3):289–367, 2013.

[114] C.D. Yuen, B. Unal, D. Jing, and P.A. Thiel. Weak bonding of Zn in an Al-based approximant based on surface measurements. *Philosophical Magazine*, 91(19-21):2879–2888, 2011.

[115] A. Al-Mahboob, M. Lowe, R. McGrath, and H.R. Sharma. Transition state limited kinetics in stabilizing intermetallic surfaces. *In preparation*, 2015.

[116] S.J. Clark, M.D. Segall, C.J. Pickard, P.J. Hasnip, M.I.J. Probert, K. Refson, and M.C. Payne. First principles methods using CAStep. *Zeitschrift für Kristallographie*, 220:567–570, 2005.

[117] K.E. Hermann and M.A. van Hove. The software utility LEEDpat, version 4.1. Berlin/Hong Kong, 2014.

[118] D. Shechtman, I. Blech, D. Gratias, and J.W. Cahn. Metallic phase with long-range orientational order and no translational symmetry. *Physics Review Letters*, 53(20):1951–1953, 1984.

[119] J.M. Dubois, S.S. Kang, and J. Von Stebut. Quasicrystalline low-friction coatings. *Journal of Materials Science Letters*, 10(9):537–541, 1991.

[120] S.S. Kang, J.M. Dubois, and J. von Stebut. Tribological properties of quasicrystalline coatings. *Journal of Materials Research*, 8:2471–2481, 1993.

[121] U. Köster, W. Liu, H. Liebertz, and M. Michel. Mechanical properties of quasicrystalline and crystalline phases in Al-Cu-Fe alloys. *Journal of Non-Crystalline Solids*, 153–154:446–452, 1993.

[122] A.P. Tsai, H. Suenaga, M. Ohmori, Y. Yokoyama, A. Inoue, and T. Masumoto. Temperature dependence of hardness and expansion in an icosahedral Al-Pd-Mn alloy. *Japanese Journal of Applied Physics*, 31(8R):2530, 1992.

[123] Z. Wang, W. Zhao, C. Qin, and Y. Cui. Fabrication and corrosion resistance of Mg-Zn-Y-based nano-quasicrystal alloys. *Materials Research*, 15:51–56, 2012.

[124] Y. Yokoyama, T. Miura, A.P. Tsai, A. Inoue, and T. Masumoto. Preparation of a large $Al_70Pd_20Mn_10$ single-quasicrystal by the czochralski method and its electrical resitivity. *Materials Transactions JIM*, 33(2):97–101, 1992.

[125] C.J. Jenks and P.A. Thiel. Quasicrystals: A short review from a surface science perspective. *Langmuir*, 14(6):1392–1397, 1998.

[126] J.M. Dubois. *Proceedings of the conference New Horizons in Quasicrystals*, volume 77, chapter Survey of the Potential Applications of Quasicrystals, pages 1928–1938. World Scientific, 1997.

[127] I.M. Hutchings. *Tribology: Friction and Wear of Engineering Materials*. Friction and Wear of Engineering Materials. Edward Arnold, 1992.

[128] S. Takeuchi, H. Akiyama, N. Naito, T. Shibuya, T. Hashimoto, K. Edagawa, and K. Kimura. Electrical resistivity of single-grained quasicrystals. *Journal of Non-Crystalline Solids*, 153–154:353–356, 1993.

[129] J.M. Dubois. *Journal of Materials Research*, 8(1):31, 1993.

[130] A. Perrot and J.M. Dubois. *Ann. Chim. Fr. Special Issue on Quasicrystals*, 18:501, 1993.

[131] A.P. Tsai and M. Yoshimura. Highly active quasicrystalline Al-Cu-Fe catalyst for steam reforming of methanol. *Applied Catalysis A-General*, 214(2):237–241, 2001.

[132] M. Yoshimura and A.P. Tsai. Quasicrystal application on catalyst. *Journal of Alloys and Compounds*, 342(1–2):451–454, 2002.

[133] B.P. Ngoc, C. Geantet, M. Aouine, G. Bergeret, S. Raffy, and S. Marlin. Quasicrystal derived catalyst for steam reforming of methanol. *International Journal of Hydrogen Energy*, 33:1000–1007, 2008.

[134] S. Kameoka, T. Tanabe, and A.P. Tsai. Al-Cu-Fe quasicrystals for steam reforming of methanol: A new form of copper catalysts. *Catalysis Today*, 93-95:23–26, 2004.

[135] T. Tanabe, S. Kameoka, and A.P. Tsai. A novel catalyst fabricated from Al-Cu-Fe quasicrystal for steam reforming of methanol. *Catalysis Today*, 111:153–157, 2006.

[136] J.C. Amphlett, K.A.M. Creber, J.M. Davis, R.F. Mann, B.A. Peppley, and D.M. Stokes. Hydrogen production by steam reforming of methanol for polymer electrolyte fuel cells. *International Journal of Hydrogen Energy*, 19(2):131–137, 1994.

[137] T. Tanabe, S. Kameoka, and A.P. Tsai. Microstructure of leached Al-Cu-Fe quasicrystal with high catalytic performance for steam reforming of methanol. *Applied Catalysis A: General*, 384:241–251, 2010.

[138] T. Tanabe, S. Kameoka, E. Sato, M. Terauchi, and A. P. Tsai. Cross-section TEM investigation of quasicrystalline catalysts prepared by aqueous NaOH leaching. *Philosophical Magazine*, 87:3103–3108, 2007.

[139] T. Tanabe, S. Kameoka, and A.P. Tsai. Evolution of microstructure induced by calcination in leached Al-Cu-Fe quasicrystal and its effects on catalytic activity. *Journal of Materials Science*, 46:2242–2250, 2011.

[140] A.A. Pavlic and H. Adkins. Preparation of a raney nickel catalyst. *Journal of the American Chemical Society*, 68(8):1471–1471, 1946.

[141] I.R. Fisher, M.J. Kramer, Z. Islam, R.A. Ross, A. Kracher, T. Weiner, M.J. Sailer, A.J Goldman, and P.C Canfield. On the growth of decagonal Al-Ni-Co quasicrystals from the ternary melt. *Philosophical Magazine B*, 79:425–434, 1999.

[142] T.P. Yadav, S.S. Mishra, S.K. Pandey, D. Singh, M. Lowe, R. Tamura, N.K. Mukhopadhyay, O.N. Srivastava, R. McGrath, and H.R. Sharma. Leaching of Al-based polygrain quasicrystalline and related crystalline surfaces. *Acta Physica Polonica, A*, 126(2):629–632, 2014.

[143] J. Lu, Y. Lei, K.C. Lau, X. Luo, P. Du, J. Wen, R.S. Assary, U. Das, D.J. Miller, J.W. Elam, H.M. Albishri, D.A. El-Hady, Y.K. Sun, L.A. Curtiss, and K. Amine. A nanostructured cathode architecture for low charge overpotential in lithium-oxygen batteries. *Nature Communications*, 4:2383, 2013.

[144] H.R. Sharma, M. Shimoda, and A.P. Tsai. Quasicrystal surfaces: Structure and growth of atomic overlayers. *Advances in Physics*, 56(3-4):403–464, 2007.

[145] C. Beeli, T. Gödecke, and R. Lück. Highly faceted growth shape of microvoids in icosahedral Al-Mn-Pd. *Philosophical Magazine Letters*, 78(5):339–348, 1998.

[146] A. Haugeneder, T. Eisenhammer, A. Mahr, J. Schneider, and M. Wendel. Oxidation of quasicrystalline and crystalline AlCuFe thin films in air. *Thin Solid Films*, 307(1–2):120–125, 1997.

[147] D. Rouxel, M. Gil-Gavatz, P. Pigeat, and B. Weber. Oxidation kinetics of the quasicrystalline *i*-AlCuFe phase compared with that of crystalline *x*-AlCuFe and pure aluminium. *Journal of Non-Crystalline Solids*, 351:802–809, 2005.

[148] D. Rouxel and P. Pigeat. Surface oxidation and thin film preparation of Al-CuFe quasicrystals. *Progress in Surface Science*, 81(10–12):488–514, 2006.

[149] B.I. Wehner and U. Koster. Oxidation of bulk Al-Cu-Fe quasicrystals. In S. Takeuchi and T. Fujiwara, editors, *Proceedings of the 6th International Conference on Quasicrystals*, pages 773–776. World Scientific, Tokyo, 1998.

[150] C. Hinnen, D. Imbert, J.M. Siffre, and P. Marcus. An in situ XPS study of sputter-deposited aluminium thin films on graphite. *Applied Surface Science*, 78:219–231, 1994.

[151] N.S. McIntyre and D.G. Zetaruk. X-ray photoelectron spectroscopic studies of iron oxides. *Analytical Chemistry*, 49:1521, 1977.

[152] N.S. McIntyre and M.G. Cook. X-ray photoelectron studies on some oxides and hydroxides of cobalt, nickel, and copper. *Analytical Chemistry*, 47:2208, 1975.

[153] J.P. Tobin, W. Hirshwald, and J. Cunningham. XPS and XAES studies of transient enhancement of Cu at CuO surfaces during vacuum outgassing. *Applications of Surface Science*, 16(3-4):441–452, 1983.

[154] S. Poulston, P.M. Parlett, P. Stone, and M. Bowker. Surface oxidation and reduction of CuO and Cu_2O studied using XPS and XAES. *Surface and Interface Analysis*, 24(12):811–820, 1996.

[155] M.C. Biesinger, B.P. Payne, A.P. Grosvenor, L.W.M. Lau, A.R. Gerson, and R.S.C. Smart. Resolving surface chemical states in XPS analysis of first row transition metals, oxides and hydroxides: Cr, Mn, Fe, Co and Ni. *Applied Surface Science*, 257:2717, 2011.

[156] V. Zabarskas, S. Tamulevičius, I. Prosyčevas, and J. Puišo. Analysis of Fe_3O_4 protective coatings thermally grown on color picture TV tube structural steel components. *Materials Science (Medžiagotyra)*, 10(2):147–151, 2004.

[157] J.A. Barrow, V. Fournée, A.R. Ross, P.A. Thiel, M. Shimoda, and A.P. Tsai. Photoemission studies of the sputter-induced phase transformation on the Al-Cu-Fe surface. *Surface Science*, 539(1–3):54–62, 2003.

[158] C.F. Brucker and T.N. Rhodin. Oxygen chemisorption and reaction on α-Fe(100) using photoemission and low-energy electron diffraction. *Surface Science*, 57:523–539, 1976.

[159] K.H. Schulz and D.T. Cox. Photoemission and low-energy-electron-diffraction study of clean and oxygen-dosed Cu_2O (111) and (100) surfaces. *Physical Review B*, 43:1610–1621, 1991.

[160] R. Mäder, R. Widmer, P. Gröning, S. Deloudi, W. Steurer, M. Heggen, P. Schall, M. Feuerbacher, and O. Gröning. High-resolution scanning tunneling microscopy investigation of the (12110) and (10000) two-fold symmetric *d*-Al-Ni-Co quasicrystalline surfaces. *Physical Review B*, 80:035433, July 2009.

[161] G. Ungar and X. Zeng. Frank-Kasper, quasicrystalline and related phases in liquid crystals. *Soft Matter*, 1:95–106, 2005.

[162] E.Y. Vedmedenko, H.P. Oepen, and J. Kirschner. Decagonal quasiferromagnetic microstructure on the penrose tiling. *Physical Review Letters*, 90:137203, 2003.

[163] J. Ledieu, C.A. Muryn, G. Thornton, R.D. Diehl, T.A. Lograsso, D.W. Delaney, and R. McGrath. C_60 adsorption on the quasicrystalline surface of $Al_{70}Pd_{21}Mn_9$. *Surface Science*, 472(1):89–96, 2001.

[164] J.A. Smerdon, J.K. Parle, L.H. Wearing, L. Leung, T.A. Lograsso, A.R. Ross, and R. McGrath. C_{60} adsorption on an aperiodically modulated Cu surface. *Journal of Physics: Conference Series*, 226(1):012006, 2010.

[165] K.M. Young, J.A. Smerdon, H.R. Sharma, M. Lahti, K. Pussi, and R. McGrath. Acene adsorption on a fibonacci-modulated Cu film. *Physical Review B*, 87:085407, 2013.

[166] J.A. Smerdon, L. Leung, J.K. Parle, C.J. Jenks, R. McGrath, V. Fournée, and J. Ledieu. Formation of a quasicrystalline Pb monolayer on the 10-fold surface of the decagonal Al–Ni–Co quasicrystal. *Surface Science*, 602(14):2496–2501, 2008.

[167] P.J. Nugent, J.A. Smerdon, R. McGrath, M. Shimoda, C. Cui, A.P. Tsai, and H.R. Sharma. Step-terrace morphology and reactivity to C_{60} of the five-fold icosahedral Ag–In–Yb quasicrystal. *Philosophical Magazine*, 91(19–21):2862–2869, 2011.

[168] A. Yamamoto, H. Takakura, and A.P. Tsai. Six-dimensional model of icosahedral Al-Pd-Mn quasicrystals. *Physical Review B*, 68:094201, 2003.

[169] M. Boudard, M. de Boissieu, C. Janot, J.M. Dubois, and C. Dong. The structure of the icosahedral AlPdMn quasicrystal. *Philosophical Magazine Letters*, 64(4):197–206, 1991.

[170] H.R. Sharma, V. Fournée, M. Shimoda, A.R. Ross, T.A. Lograsso, A.P. Tsai, and A. Yamamoto. Structure of the fivefold surface of the icosahedral Al-Cu-Fe quasicrystal: Experimental evidence of bulk truncations at larger inter-layer spacings. *Physical Review Letters*, 93:165502–165505, 2004.

[171] J. Ledieu, P. Unsworth, T.A. Lograsso, A.R. Ross, and R. McGrath. Ordering of Si atoms on the fivefold Al-Pd-Mn quasicrystal surface. *Physical Review B*, 73:012204, 2006.

[172] J. Ledieu, M. Krajčí, J. Hafner, L. Leung, L.H. Wearing, R. McGrath, T.A. Lograsso, D. Wu, and V. Fournée. Nucleation of Pb starfish clusters on the five-fold Al-Pd-Mn quasicrystal surface. *Physical Review B*, 79:165430, 2009.

[173] T. Cai, F. Shi, Z. Shen, M. Gierer, A.I. Goldman, M.J. Kramer, C.J. Jenks, T.A. Lograsso, D.W. Delaney, P.A. Thiel, and M.A. van Hove. Structural aspects of the fivefold quasicrystalline Al–Cu–Fe surface from STM and dynamical LEED studies. *Surface Science*, 495(1–2):19–34, 2001.

[174] M.O. Blunt, J.C. Russell, M.D.C. Giménez-López, J.P. Garrahan, X. Lin, M. Schröder, N.R. Champness, and P.H. Beton. Random tiling and topological defects in a two-dimensional molecular network. *Science*, 322(5904):1077–1081, 2008.

[175] J.A. Smerdon, M. Bode, N.P. Guisinger, and J.R. Guest. Monolayer and bilayer pentacene on Cu(111). *Physical Review B*, 84:165436, 2011.

[176] H. Takakura, C..P. Gomez, A. Yamamoto, M. de Boissieu, and A.P. Tsai. Atomic structure of the binary icosahedral Yb-Cd quasicrystal. *Nature Materials*, 6(1):58–63, 2007.

[177] C. Cui, M. Shimoda, and A.P. Tsai. Studies on icosahedral Ag-In-Yb: a prototype for Tsai-type quasicrystals. *RSC Advances*, 4:46907–46921, 2014.

[178] C. Cui, P.J. Nugent, M. Shimoda, J. Ledieu, V. Fournée, A.P. Tsai, R. McGrath, and H.R. Sharma. The atomic structure of the threefold surface of the icosahedral Ag–In–Yb quasicrystal. *Journal of Physics: Condensed Matter*, 24(44):445011, 2012.

[179] C. Cui, P.J. Nugent, M. Shimoda, J. Ledieu, V. Fourné, A.P. Tsai, R. McGrath, and H.R. Sharma. Structure of the twofold surface of the icosahedral Ag–In–Yb quasicrystal. *Journal of Physics: Condensed Matter*, 26(1):015001, 2014.

[180] V. Fournée, É. Gaudry, J. Ledieu, M.C. de Weerd, D. Wu, and T. Lograsso. Self-organized molecular films with long-range quasiperiodic order. *ACS Nano*, 8(4):3646–3653, 2014.

[181] D.J. Hucknall and A. Morris. *Vacuum Technology*. The Royal Society of Chemistry, 2003.